Improving the Imaging Performance of Novel Ultrasonic Arrays

By James P. Kirkpatrick

Department of Mechanical Engineering
University of Bristol

A dissertation submitted to the University of Bristol in accordance with the requirements for award of the degree of Engineering Doctorate in the Faculty of Engineering.

SEPTEMBER 2020

Word count: Sixteen thousand, two hundred and twenty-seven.

Abstract

Ultrasonic arrays have been a common feature of ultrasonic non-destructive evaluation in academia for many years. Their prevalence in industry has also recently increased. As ultrasonic arrays have become more common, so have the number of novel ultrasonic arrays. These novel arrays have come from industrial companies driving the production of arrays with higher numbers of elements and from the academic community applying concepts from ultrasonic arrays to less common methods of ultrasonic testing. In this work, the imaging performance of two very different novel ultrasonic arrays have been improved.

Firstly, the total focusing method has been adapted for use with row-column addressed arrays. The algorithm has been demonstrated experimentally to improve the detectability and sizing of simulated defects, with a less-than-half-wavelength conical bottom hole being successfully detected and the sizing accuracy being increased by an order of magnitude.

Secondly, diffuse field reconstruction techniques have been demonstrated to increase the data collection speed of laser ultrasonic arrays by two orders of magnitude. The techniques used have created an array of laser interferometers which appear as if they transmit and receive ultrasound, producing images with similar properties to conventional ultrasonic arrays.

This work was funded by the Engineering and Physical Sciences Research Council and the Defence Science and Technology Laboratory.

Acknowledgements

On Sunday 9th July 2017, in a small church in Overberg in The Netherlands, a man stood up and preached from The Bible on Ephesians chapter 1 verse 1, ”Paulus, een apostel van Jezus Christus door de wil van God” [Paul, an apostle of Jesus Christ by the will of God]. I thank God for this man, Maarten Ezinga, and others like him who taught me that, as wonderful as doing a doctorate is, there are far more important things in life. I thank God for giving me children, family, friends and churches which I have been blessed to be a member of. I especially thank Him for giving me a godly and supportive wife who would self-sacrificially walk with me through this whole doctorate and beyond. But most of all, above all else, I thank the LORD for saving me: for taking me as I was in my sinful state, paying the ransom on the cross for all of the wrong I have done, and giving me a new heart that I could live for Him.

James Kirkpatrick (an EngD student by the will of God)

Soli Deo Gloria

Author's Declaration

I declare that the work in this dissertation was carried out in accordance with the requirements of the University's *Regulations and Code of Practice for Research Degree Programmes* and that it has not been submitted for any other academic award. Except where indicated by specific reference in the text, the work is the candidate's own work. Work done in collaboration with, or with the assistance of, others, is indicated as such. Any views expressed in the dissertation are those of the author.

SIGNED: .....JAMES KIRKPATRICK..... DATE: .....05/09/2020.....

Table of Contents

List of Tables

List of Figures

Chapter 1

Introduction

1.1 Background

Non-Destructive Evaluation (NDE) is the process of evaluating the structure of an object without destroying the object. This is typically achieved by surface examination or by propagating waves through part, or all, of the object. Examples of surface examination NDE techniques include visual inspection, liquid penetrant testing [2], magnetic particle testing [3] and eddy-current testing [4]. Examples of NDE techniques which evaluate the internal structure of an object are radiography [5], thermography [6] and ultrasonics [7]. The use of ultrasonic frequency sound waves is a popular NDE technique because it can be used to build up a detailed picture of the internal structure of an object and is relatively safe to apply. The waves are propagated through the object, signals recorded, and inversion methods used to infer the structure which produced that set of signals.

For many years, ultrasonic testing was confined to single element probes. Ultrasound was either excited and received on the same probe, called pulse-echo, or transmitted and received on two different probes, called pitch-catch. Towards the end of the twentieth century, a transition to ultrasonic arrays was made. These were made from many single elements joined together. Excitation of the ultrasonic waves from each element was delayed in time so that constructive and destructive interference in the material would produce steered ultrasonic beams or beams with particular focal points. The same technique could be used in reception. Eventually, the elements were excited and received individually and sequentially, and the delays were applied in post-processing. This method allows the array to be focussed at multiple locations in the material.

Since ultrasonic arrays were first used, many novel variants in design have been created in order to reduce the effect of a particular limitation or apply the array principle to a particular situation.

One restriction encountered with ultrasonic arrays is the limit on the number of elements in the array. This restriction is imposed by the number of interconnections required as the number of array elements increases. Arrays need a large number of elements in order to produce a large aperture at the same time as meeting the array element spacing requirements needed for a high quality ultrasonic beam. Ideally, arrays with elements in two dimensions would also meet these requirements. However this number of interconnections is often too large for practical use. A compromise therefore has to be made. This compromise has meant the creation of many novel array designs.

The array principle can also be applied to more abstract ultrasonic testing technology. The use of laser ultrasonic testing allows broadband sources and detectors to be used and non-contact measurements to be made. A natural extension of single point measurements was to create laser ultrasonic arrays. This is an example of the array principle being applied to a more novel technology.

The ultrasonic imaging performance of an array is of fundamental importance when trying to detect and characterise defects. For example, an increase in resolution can help to resolve defect features which are close together, enabling better sizing or the distinguishing of multiple defects from each other. Similarly, the removal of imaging artefacts from images enables defects to be detected and characterised with more certainty. Industry is always looking for ways to improve the detectability and characterisation of defects. Improving the imaging performance of arrays is therefore important to industry.

This thesis aims to improve the imaging performance of two novel ultrasonic arrays. The first covers Row-Column Addressed (RCA) arrays. RCA arrays use a different array design to increase the number of effective elements in the array while maintaining the number of interconnections at a manageable level. The second covers laser ultrasonic arrays. Neither of these arrays are standard and both have reported problems associated with imaging performance.

1.2 Thesis Structure

After this introduction chapter, the thesis is split into two main sections. Each section covers a different aspect of improving the imaging performance of a novel ultrasonic array and each comprises a triplet of three chapters. The first chapter in each triplet provides a brief overview of the theory and the literature of the subject dealt with in that section. The second and third chapters in each triplet comprise the original work undertaken as part of this project. The second chapter always considers modelling; the third, always experiment. Conclusions are drawn at the end of each of these chapters. After both triplets, a joint conclusion is drawn to end the thesis. The conclusion also contains recommendations of possible further work in each area.

The first triplet covers the use of the Total Focusing Method (TFM) with RCA arrays. This work was presented at the 56th Annual British Conference of Non-Destructive Testing in 2017 and published as a journal paper in 2019 [8]. The results of this work were presented to DolphiTech, the manufacturer of the RCA array used. In 2020, DolphiTech added the adapted TFM algorithm proposed in this work into their latest product.
The second triplet covers the use of diffuse fields with laser ultrasonic arrays. This work was presented to industry at the Research Centre for Non-Destructive Evaluation Technology Transfer Day and the British Institute of Non-Destructive Testing Aerospace Event, both in 2019. This work has not yet been published as a journal paper.

Chapter 2

Ultrasonics, Arrays and Row-Column Addressed Arrays

2.1 Ultrasonics

Ultrasonic frequency pressure waves have been used for the Non-Destructive Evaluation (NDE) of materials for many years. Traditionally, a single crystal of piezoelectric material is contained, with damping material and a face material, in the housing of an ultrasonic probe or transducer. This ultrasonic probe is used to excite and detect ultrasound in a material. How ultrasound is emitted, received and interacts with a material structure can be predicted through mathematical models. These models have inherent approximations but, nevertheless, can provide useful information about a system. The generated field can be described using the quantities and equations set out in the following sub-sections.

2.1.1 Directivity

Firstly, the directivity of the transducer is considered. The directivity describes how the amplitude of the ultrasonic field radiated from a transducer varies with angle. The approximations made here for the directivity are only valid in the far field of the probe, that is, where the dependency of the amplitude of the field on distance and angle can be decoupled.

All probes have a geometric directivity which is based on their shape. The geometric directivity, Γ_g, of a rectangular transducer is given by the equation [9]:

$$\Gamma_g(\theta, \varphi, \omega) = \left| \operatorname{sinc}\left(\frac{\pi \ell_1 \sin(\theta)\cos(\varphi)}{\lambda(\omega)}\right) \operatorname{sinc}\left(\frac{\pi \ell_2 \sin(\theta)\sin(\varphi)}{\lambda(\omega)}\right) \right|, \tag{2.1}$$

where ℓ_1 is the width in the x direction, ℓ_2 is the length in the y direction, θ is the polar angle, measured from the z axis, φ is the azimuthal angle, measured from the x axis, ω is the angular frequency and λ is the wavelength. The angular frequency is given by $\omega = 2\pi\nu$ where ν is the frequency. As wavelength is dependant on the frequency of the transducer, it is clear that the directivity is also frequency dependent.

The component response directivity relates to how the excited transducer generates different ultrasonic wave modes in the material it is coupled to. An approximation to this is given by the component response directivity of a finite diameter disc applying a harmonic force to the surface of a semi-infinite isotropic elastic solid. The component response directivity, Γ_c, for the longitudinal waves generated in the solid is given by [10]:

$$\Gamma_c(\theta) \propto \frac{\cos(\theta)\left({v_r}^2 - 2\sin^2(\theta)\right)}{\left(2\sin^2(\theta) - {v_r}^2\right)^2 - 4\sin^2(\theta)\sqrt{\left(\sin^2(\theta)-1\right)}\sqrt{\left(\sin^2(\theta)-{v_r}^2\right)}}, \tag{2.2}$$

where

$$v_r = \frac{v_l}{v_s}, \tag{2.3}$$

and v_l and v_s are the longitudinal and shear wave velocities in the solid. Finally, the combined directivity is given by the product of the geometric and component response directivities:

$$\Gamma(\theta, \varphi, \omega) = \Gamma_g(\theta, \varphi, \omega)\,\Gamma_c(\theta). \tag{2.4}$$

By reciprocity [11], the directivity describing how the amplitude response of a transducer to an incoming ultrasonic field varies with angle is given by the same equation.

2.1.2 Beam Spread

Secondly, the beam spread of the transducer is considered. The beam spread, or geometric attenuation, accounts for the fact that as the ultrasound propagates from the transducer it spreads out in space. An approximation to the beam spread, B, of a 2-Dimensional (2D) transducer, that is where $\ell_2 = \infty$, is given by:

$$B \approx \sqrt{\frac{1}{|\mathbf{b}|}}\,, \tag{2.5}$$

where

$$\mathbf{b} = \mathbf{e} - \mathbf{d}, \tag{2.6}$$

$\mathbf{e}$ is the centre of the transducer and $\mathbf{d}$ is the measurement location. Similarly, an approximation to the beam spread of a 3-Dimensional (3D) transducer is given by:

$$B \approx \frac{1}{|\mathbf{b}|}. \tag{2.7}$$

These beam spread equations can be combined when dealing with reflections from geometric features. For example, the total beam spread for a reflection from a point reflector is given by:

$$B_{tr} = B_t B_r, \tag{2.8}$$

where B_t and B_r are the values of the beam spread at the point reflector for the transmitting and receiving transducer respectively.

2.2 Ultrasonic Arrays

Ultrasonic arrays are made up of many single elements. In addition to length and width, useful characteristic measurements for linear arrays are pitch, ℓ_3, and the number of elements, n_e. The dimensions of an example array are shown in Figure 2.1. Arrays can be used to steer or focus ultrasound in the material by applying delays to the transmission or reception of each element. This can also be done in post-processing. The maximum amount of data which can be collected by an array for post processing is the full array response matrix. This is collected by transmitting on each element individually and sequentially while also receiving on the elements individually.

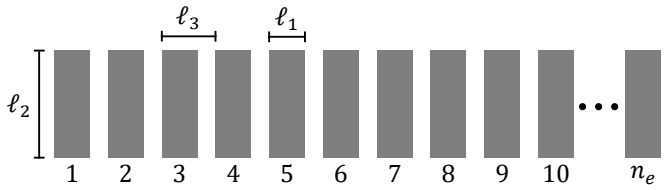

Figure 2.1: Schematic of a linear array of n_e elements with characteristic lengths indicated.

2.2.1 Modelling Ultrasonic Arrays

The full array response matrix of an array can be analytically modelled in 3D using a frequency-domain linear time invariant model [12, 13]. This model is similar to those successfully used by numerous authors, especially in the NDE group at the University of Bristol [14, 15, 16, 17,

18, 19]. In this model, the full array response matrix spectra, $\tilde{h}_{tr}(\omega)$, when a point reflector target is located at $\mathbf{d}$ in a semi-infinite homogeneous medium, is given by:

$$\tilde{h}_{tr}(\omega) = \Psi_0(\omega)\; B_{tr}(\mathbf{b_t}, \mathbf{b_r})\; \Gamma_t(\theta_t, \varphi_t, \omega)\; \Gamma_r(\theta_r, \varphi_r, \omega) \exp\left(-i\omega \frac{|\mathbf{b_t}| + |\mathbf{b_r}|}{v}\right), \tag{2.9}$$

where Ψ_0 is the spectrum of the input pulse, v is the velocity of the wave and $i = \sqrt{-1}$. The final exponent term in the equation describes the propagation of the wave. Due to the assumptions made in some of the terms, this model is only valid in the far field of the elements.

2.2.2 Imaging with Ultrasonic Arrays

Ultrasonic imaging is useful in that it can provide, from a series of signals, a graphical representation of the structure that produced those signals. Two main imaging algorithms, the Plane B-Scan algorithm and the Total Focusing Method (TFM), are considered in this work. The image, I, at a voxel located at $\mathbf{p}$, when using the Plane B-Scan algorithm is given by the equation:

$$I(\mathbf{p}) = \sum_{t,r} \Lambda_t\; \Lambda_r\; h_{tr}\left(\frac{|\mathbf{c_t} \cdot \hat{\mathbf{z}}| + |\mathbf{c_r} \cdot \hat{\mathbf{z}}|}{v}\right), \tag{2.10}$$

where

$$\mathbf{c_j} = \mathbf{e_j} - \mathbf{p},$$

Λ_j is a weighting function and h_{tr} is the time domain full array response matrix. For the Plane B-Scan algorithm, Λ_j is often defined as:

$$\Lambda_j = \begin{cases} 1 & \text{if } \sqrt{(\mathbf{c_j} \cdot \hat{\mathbf{x}})^2 + (\mathbf{c_j} \cdot \hat{\mathbf{y}})^2} \leq \dfrac{a}{2} \\ 0 & \text{otherwise} \end{cases} \tag{2.11}$$

where a is the aperture diameter.

Similarly, when using the TFM algorithm, the image is given by the equation:

$$I(\mathbf{p}) = \sum_{t,r} \Lambda_t\; \Lambda_r\; h_{tr}\left(\frac{|\mathbf{c_t}| + |\mathbf{c_r}|}{v}\right). \tag{2.12}$$

Different weighting functions are usually applied for the TFM algorithm. In the original definition of the TFM algorithm $\Lambda_j = 1$ was used [20]. An alternative example would be an angle limit at the voxel. In this case, Λ_j would be defined as:

$$\Lambda_j = \begin{cases} 1 & \arccos\left(\dfrac{\mathbf{c_j} \cdot \hat{\mathbf{z}}}{|\mathbf{c_j}|}\right) \leq \theta_{\text{limit}} \\ 0 & \text{otherwise} \end{cases} \tag{2.13}$$

where θ_{limit} is the angle limit at the voxel.

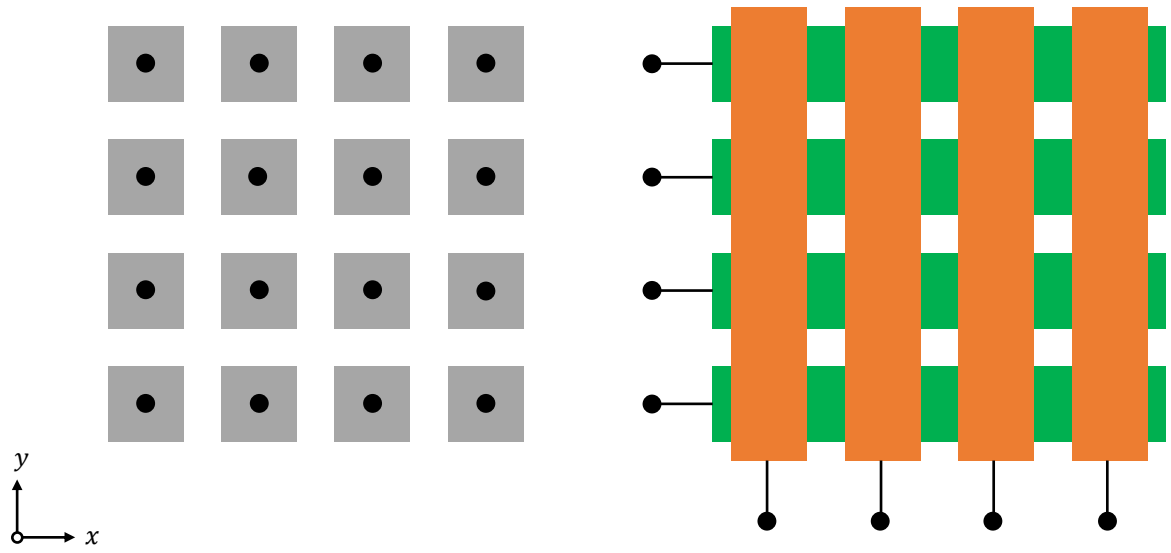

(a) (b)

Figure 2.2: Schematic of (a) FP2 and (b) RCA arrays for which $n_e = 4$. The difference in the number of interconnections is clear.

2.3 Row-Column Addressed Arrays

A 2D array with a large number of very small elements separated by a small pitch which can all be independently controlled is very useful. In practice, the manufacturing process limits the size and pitch of the elements, as well as the number of connections it is possible to make with those elements. This has led to the development of more novel array designs which have been proposed to suit specific inspection scenarios and provide a balance between the number of elements and the inspection quality or speed. This has included the Mill's cross configuration [21], which uses elements arranged in a cross shape to increase array area while maintaining a small number of elements, random sparse arrays [22] which allow the array elements to be positioned further apart and use destructive interference to reduce the resulting side lobes, and Row-Column Addressed (RCA) arrays [23] which use two orthogonal overlapping linear arrays. These RCA arrays will be the focus of this section of work.

If a Fully Populated 2D (FP2) array is defined as a simple 2D array consisting of square elements arranged on a uniform Cartesian grid to form a square array, then RCA arrays, by contrast, are formed by two identical, but orthogonally orientated, linear arrays of elongated elements placed on top of each other. A schematic of the two arrays is shown in Figure 2.2.

In order to compare the performance of these two types of arrays, a useful characteristic length needs to be defined. For these two array types, the array width given in terms of the number of elements, n_e, is a good comparator [Figure 2.2]. Both arrays are assumed to be square and the elements have a constant pitch. The total number of elements in the array, and therefore the number of interconnections needed, N_e, can now be defined for each type of array. For FP2 arrays this is given by $N_e = {n_e}^2$, and for RCA arrays this is given by $N_e = 2n_e$. These relationships show that RCA arrays have $\frac{1}{2}n_e$ times fewer elements than their FP2 array counterparts. Similarly, the number of unique transmit-receive combinations, N_{tr}, that can be obtained using these arrays is given by the equation $N_{tr} = {N_e}^2$. This would result in RCA arrays having $\frac{1}{4}{n_e}^2$ less transmit-receive combinations compared to FP2 arrays. However, in practise, for both types of array, this is often reduced. For FP2 arrays, the reciprocity principle [11] requires only half of the full array response matrix to be collected. In this case $N_{tr} = \frac{1}{2}N_e\left(N_e + 1\right)$. For RCA arrays, transmit-receive element combinations where the transmit and receive elements are not orthogonal are often disregarded. In addition, the reciprocity principle is applied so that only one of set of the perpendicular elements are ever used to transmit or receive respectively. In this reduced case, $N_{tr} = \frac{1}{4}{N_e}^2$. These relationships show that RCA arrays normally use $\frac{1}{2}\left({n_e}^2 + 1\right)$ times fewer transmit-receive combinations than FP2 arrays. Other than different values for N_e and N_{tr}, the array types also differ in ultrasonic response. This is due to the differences between square and elongated rectangular elements. These differences form the basis of the compromise in performance which needs to be evaluated.

RCA arrays were originally invented for use in through-transmission NDE in order to increase both the number of effective elements in 2D arrays and increase the scanning speed [24]. In addition to continued use in through-transmission NDE [25, 26], these arrays have been used for different applications including particle manipulation [27], photoacoustic imaging [28] and medical imaging [29]. In the simplest case, image volumes can be formed by using the assumption that each A-scan originates from a fictional element located at the intersection between the physical transmit and receive elements. Recently, a number of developments have been made in the medical ultrasonics field because of increased interest in RCA arrays. Advances in the design of, and imaging using, RCA arrays have been well summarised in [30] and [31] which are currently the two most definitive papers on RCA arrays in the medical field. Improved beamforming techniques for medical imaging are shown and a new apodisation scheme was demonstrated to reduce the edge effects of elongated RCA array elements and significantly increase the imaging quality to a level comparable with FP2 arrays.

Similarly, the field of NDE has made significant advances in the last 20 years with the growing use of arrays in industry as well as the increased adoption of the TFM [20]. Many of these advances have come about by the use of systematic approaches which combine modelling and experiment. Array models are often used to predict the performance of particular arrays and test potential improvements, as well as being used to assess imaging algorithms in both medical [32] and NDE fields [33, 34].

While advances have been made in both the medical and NDE fields, the use of RCA arrays for NDE has been predominantly limited to through-transmission. Recently however, a commercial device using an RCA array has been produced specifically for NDE which operates in pulse-echo mode [35]. While the device has been introduced into industry, there is a lack of literature covering the use of RCA arrays in pulse-echo mode for NDE applications. In 2014, Wong et al. [23] attempted to use a medical RCA array to demonstrate the use of RCA arrays for NDE. This approach, however, was not representative of normal practice in NDE because of, for example, the size of the array, surface scanning and reference subtraction. Also, results were shown using images with low dynamic range. Therefore, with the additional possibility of an NDE specific RCA array, there is a need to carefully examine pulse-echo RCA array use for NDE using more standard practice, current state-of-the-art processes and imaging algorithms on representative samples.

Chapter 3

Improving Imaging with Row-Column Addressed Arrays

3.1 Introduction

A quantitative comparison between Fully Populated 2D (FP2) arrays and Row-Column Addressed (RCA) arrays has never been made in the field of Non-Destructive Evaluation (NDE). This chapter uses modelling to calculate the metric of the $6\,\mathrm{dB}$ drop volume of the Point Spread Function (PSF). This is then used to make that quantitative comparison. Comparisons are made between both array types for different sizes of array. The PSF is calculated for a target at a single location, directly below each array. If an equivalent performance is found between the array types, RCA arrays could be used in the place of FP2 arrays. This would substantially reduce the required number of elements in an array needed for 3-Dimensional (3D) imaging. The PSF is calculated for three different imaging algorithms: two Plane B-Scan algorithms with apertures of 1 and 4 elements, and the Total Focusing Method (TFM). For the RCA arrays, an adapted TFM algorithm is proposed and applied to the RCA array data. This proposed TFM algorithm is compared against the conventional Plane B-Scan imaging algorithms for the RCA array. The TFM algorithm has never been applied to RCA arrays in the field of NDE.

3.2 Method

3.2.1 Modelling

A suitable model was required in order to compare array responses and imaging algorithms for FP2 and RCA arrays. Using a Finite Element (FE) model would have been possible, but would have been prohibitively slow because of the number of degrees of freedom required. This is because the model would be 3D and dimensionally large in comparison to the small wavelength of the ultrasonic waves. Therefore, a frequency domain linear-time-invariant model was used. This model does not capture all of detailed information in the ultrasonic system, however, its accuracy is sufficient. For example, shear waves are not present in the model used. However, in a real system, the amplitude of these waves would be small in comparison to the longitudinal waves of interest.

Perfect point reflectors were used as the targets in the models in order to generate a PSF which could be used to evaluate imaging performance. The model used is described in Section 2.2.1. However, some changes were made to the model described in Section 2.2.1 so that the elongated elements of the RCA array could be modelled accurately. The length of the RCA array elements means that targets of interest are likely to be in the near field of the elements. To allow Equation (2.9) to be used, the RCA array elements were modelled by dividing each element into a number of sub-elements for which the far field assumption was valid. The responses for these sub-elements were calculated, in transmit and receive, before being summed to give the total response for each elongated element combination as shown by the equation:

$$\tilde{h}_{tr}(\omega) = \sum_{k,m} \tilde{h}_{t_k r_m}(\omega), \tag{3.1}$$

where k and m are the sub-element indices for transmit and receive elements respectively. The position of the target was always kept beneath the centre of the array. A 3-cycle Hann-weighted sine wave was used as the input pulse. For consistency with the experimental set-up used later, acrylic was used as the medium for modelling the test sample. The wave velocities used for the acrylic were $v_l = 2700\,\mathrm{m\,s^{-1}}$ and $v_s = 1100\,\mathrm{m\,s^{-1}}$ for the longitudinal and shear wave velocities respectively. Details of the arrays used in the modelling can be found in Table 3.1.

Table 3.1: Modelled array parameters.

Parameter Name	Notation	Value		Unit
Array type	-	RCA	FP2	-
Centre frequency	ν_0	3.5	3.5	MHz
Array width range	n_e	3-81	3-149	No. of elements
Total number of elements	N_e	$2n_e$	${n_e}^2$	-
Element width	ℓ_1	0.308	0.308	mm
Element length	ℓ_2	$\ell_3(n_e-1)+\ell_1$	0.308	mm
Element pitch	ℓ_3	0.385	0.385	mm

3.2.2 Imaging

Plane B-Scan and TFM algorithms were used to image the array response to the target. These have been described in Section 2.2.2. For RCA arrays, modifications were made to the standard algorithms but the general idea was kept consistent.

Plane B-Scans for RCA arrays were generated using the approximation that an A-Scan from any orthogonal transmit-receive combination originated from a fictional element located at the intersection of the physical elements. For example, if the elongation direction of the elements are in the y and x directions for transmit and receive respectively, and the element centres are located at $\mathbf{e_t} = \left(e_{t_x}, e_{t_y}, e_{j_z}\right)$ for transmit and $\mathbf{e_r} = \left(e_{r_x}, e_{r_y}, e_{j_z}\right)$ for receive, then the centre of the fictional element would be given by $\tilde{\mathbf{e}}_\mathbf{j} = \left(e_{t_x}, e_{r_y}, e_{j_z}\right)$. This is shown schematically in Figure 3.1. Two different Plane B-Scan apertures were used. These were $a = \ell_3$ and $a = 4\ell_3$ which are denoted PB1 and PB4 respectively. PB4 was used in order to simulate the default data collection method set by the DolphiCam device used later in the experimental setup. This used 4 elements in transmit in order to increase the amount of energy put into the system and, by widening the aperture, to increase the downwards component of the transmit directivity function.

The RCA-adapted TFM algorithm uses the shortest time path between the centre line of an element and a voxel in both transmit and receive. On a regular Cartesian imaging grid, symmetry reduces Equation (2.12) for RCA arrays to two 2-Dimensional (2D) path calculations, one in transmit and one in receive, which improves the speed of the algorithm. Both are calculated using Equation (2.12) in 2D as if there were two linear arrays perpendicular in orientation with one in transmit and one in receive. Using the same example as above where the elongation direction of the elements were in the y and x directions for transmit and re-

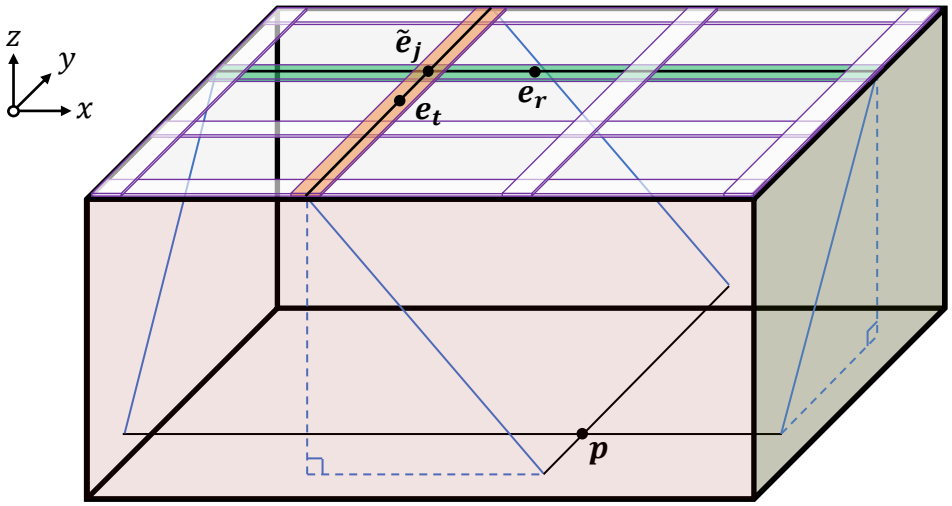

Figure 3.1: An RCA array for which $n_e = 4$ showing the centre locations, $\mathbf{e_t}$ and $\mathbf{e_r}$, of the transmit and receive elements respectively. The intersection, $\tilde{\mathbf{e}}_\mathbf{j}$, of the transmit and receive elements, relating to the fictional element used for the Plane B-Scan algorithm, is shown. The paths lengths used for a voxel at $\mathbf{p}$ for the TFM algorithm are also shown.

ceive respectively, the transmit path calculation would be calculated in the x-z plane and the receive path calculation in the y-z plane, as shown schematically in Figure 3.1. For square RCA arrays, where the number of transmit elements equals the number of receive elements, $n_{e_t} = n_{e_r}$, and the number of voxels in the x and y directions are also equal, $n_{p_x} = n_{p_y}$, symmetry simplifies the problem further and improves the speed of the algorithm. In this case, only $n_{e_t} \times n_{p_x} \times n_{p_z}$ paths need to be calculated. This is substantially less than the number of calculations required for full 3D path calculations for every element for FP2 arrays using TFM. A similar algorithm was proposed by Rasmussen et al. and Christiansen et al. for medical applications [30, 31]. However, in that algorithm, elements were focussed to a line source on transmission to increase the speed of the acquisition. In reception, delays were applied in post-processing to focus at every point. For NDE, where the speed of the acquisition is less important, the adapted TFM algorithm suggested in this work is preferable to that proposed by Rasmussen et al. and Christiansen et al. because there is no defocussing on transmission. However, this is also at the cost of a lower input energy leading to a decrease in the signal-to-random-noise ratio.

One final step was added to all algorithms used, which was to divide the amplitude of every voxel by the number of transmit-receive combinations which contribute to the voxel. This had benefits for the experimental setup which will be described later, however, when

imaging the modelled array response it reduced the unevenness of the images when the PSF was not completely contained below the array's aperture.

3.2.3 Point Spread Function Evaluation

The PSF, with a target at $\mathbf{d} = (0, 0, -5)\mathrm{mm}$, was used to compare the imaging performance of both FP2 and RCA arrays and their respective imaging algorithms. A decibel scale, normalised to the maximum amplitude of the PSF, was used. The imaging performance was quantified using a measurement of the $-6\,\mathrm{dB}$ drop volume of the PSF, $V_{-6\,\mathrm{dB}}$, which was calculated by summing the number of voxels of the image with an amplitude greater than $-6\,\mathrm{dB}$ and multiplying it by the volume of one voxel, V_p. The uncertainty in this value, $\alpha_{V_{-6\,\mathrm{dB}}}$, was estimated using the maximum uncertainty in the volume of a sphere placed in a regular 3D Cartesian grid, α_{V_s}, as follows. The volume of a sphere, V_s, is given by:

$$V_\mathrm{s} = \frac{4}{3}\pi r^3, \tag{3.2}$$

where r is the radius of the sphere. Rearranging this in terms of r yields:

$$r = \left(\frac{3}{4\pi}V_\mathrm{s}\right)^{\frac{1}{3}}. \tag{3.3}$$

Similarly, the surface area of a sphere is given by:

$$A_\mathrm{s} = 4\pi r^2. \tag{3.4}$$

By substituting (3.3) into (3.4), an equation for the relationship between volume and surface area for the sphere can be obtained:

$$A_\mathrm{s} = 4\pi\left(\frac{3}{4\pi}V_\mathrm{s}\right)^{\frac{2}{3}} = \left(36\pi V_\mathrm{s}^2\right)^{\frac{1}{3}}. \tag{3.5}$$

A similar relationship can be established for the voxel. The volume of a voxel is given by:

$$V_\mathrm{p} = R \cdot R \cdot R = R^3, \tag{3.6}$$

where R is the length of one edge of the voxel. Similarly, the area of one face of the voxel is given by:

$$A_\mathrm{p} = R \cdot R = R^2. \tag{3.7}$$

Again, by combining 3.6 and 3.7, a relationship between V_p and A_p is obtained:

$$A_{\mathrm{p}} = V_{\mathrm{p}}{}^{\frac{2}{3}}. \tag{3.8}$$

Assuming the surface area of the sphere is made up of the faces of the voxels on the edge of the sphere, then the number of voxels, n_{p}, on the edge of the sphere is given by:

$$n_{\mathrm{p}} = \frac{A_{\mathrm{s}}}{A_{\mathrm{p}}} = \left(\frac{36\pi V_{\mathrm{s}}^2}{V_{\mathrm{p}}^2}\right)^{\frac{1}{3}}. \tag{3.9}$$

The worst case uncertainty in the volume of the sphere using a regular 3D Cartesian grid can then be thought of as half a voxel volume per voxel on the edge of the sphere, or mathematically:

$$\alpha_{V_{\mathrm{s}}} \approx \frac{1}{2} V_{\mathrm{p}} n_p. \tag{3.10}$$

By substituting 3.9 into 3.10, the final expression is given by:

$$\alpha_{V_{\mathrm{s}}} = \frac{1}{2} V_{\mathrm{p}} \left(\frac{36\pi V_{\mathrm{s}}^2}{V_{\mathrm{p}}^2}\right)^{\frac{1}{3}} = \left(\frac{9}{2}\pi V_{\mathrm{p}} V_{\mathrm{s}}^2\right)^{\frac{1}{3}}. \tag{3.11}$$

As an approximation, $\alpha_{V_{\mathrm{s}}}$ is used as $\alpha_{V_{-6\,\mathrm{dB}}}$ for all of the error bars in this chapter.

3.3 Results

Example PSF B-Scan and C-Scan images for the $n_e = 41$ case for both types of array and all imaging algorithms considered are shown in Figure 3.2 and Figure 3.3 respectively. The images are shown using a decibel scale which is normalised to the maximum amplitude of the PSF in the 3D image volume and has a $40\,\mathrm{dB}$ dynamic range. The PSF was calculated as a function of n_e for both types of array and all imaging algorithms considered. $V_{-6\,\mathrm{dB}}$ as a function of n_e is shown in Figure 3.4.

3.4 Discussion

It is shown from the results in Figure 3.2 and Figure 3.3 that FP2 arrays provide a tighter PSF than RCA arrays. For a given n_e, $V_{-6\,\mathrm{dB}}$ is shown to be smaller for FP2 arrays in all cases [Figure 3.4a]. It can be clearly seen that the TFM based imaging algorithms have a narrower PSF and $V_{-6\,\mathrm{dB}}$ than the PB1 and PB4 algorithms in all cases. For low values of n_e, where $V_{-6\,\mathrm{dB}}$ of the PSF extends outside of the array aperture, the division of the amplitude by the

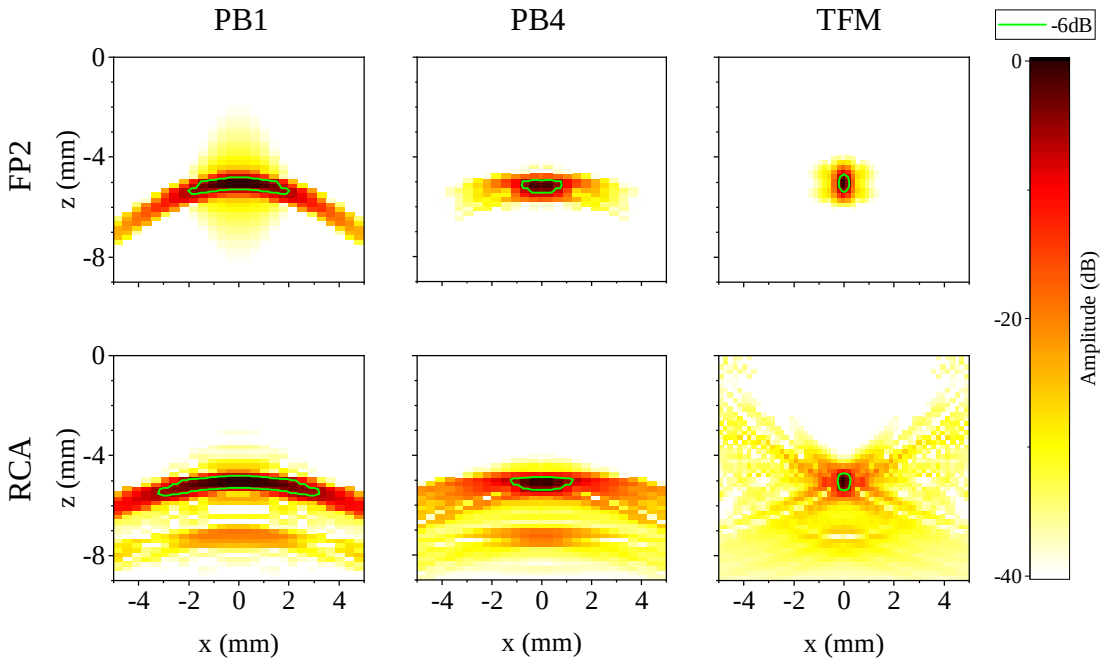

Figure 3.2: B-Scan at $y = 0\,\mathrm{mm}$ of the PSF with a target at $\mathbf{d} = (0, 0, -5)\mathrm{mm}$ for $n_e = 41$. FP2 and RCA arrays are shown from top to bottom respectively. PB1, PB4 and TFM imaging algorithms are shown from left to right respectively.

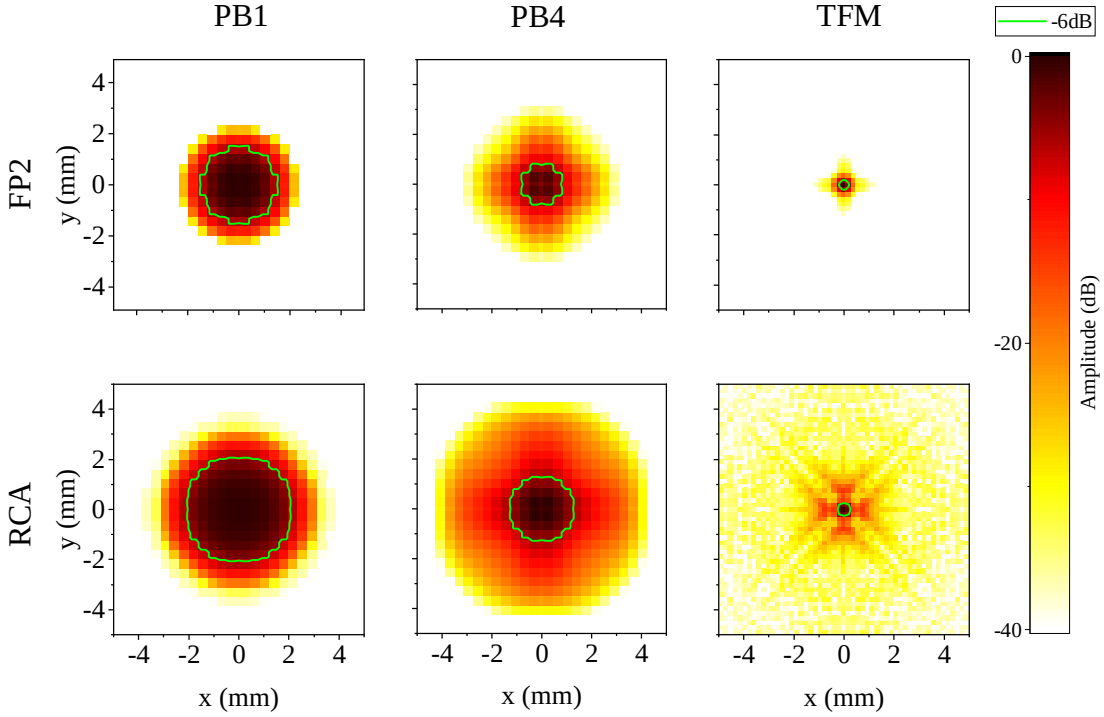

Figure 3.3: C-Scan at $z = -5\,\mathrm{mm}$ of the PSF with a target at $\mathbf{d} = (0, 0, -5)\mathrm{mm}$ for $n_e = 41$. FP2 and RCA arrays are shown from top to bottom respectively. PB1, PB4 and TFM imaging algorithms are shown from left to right respectively.

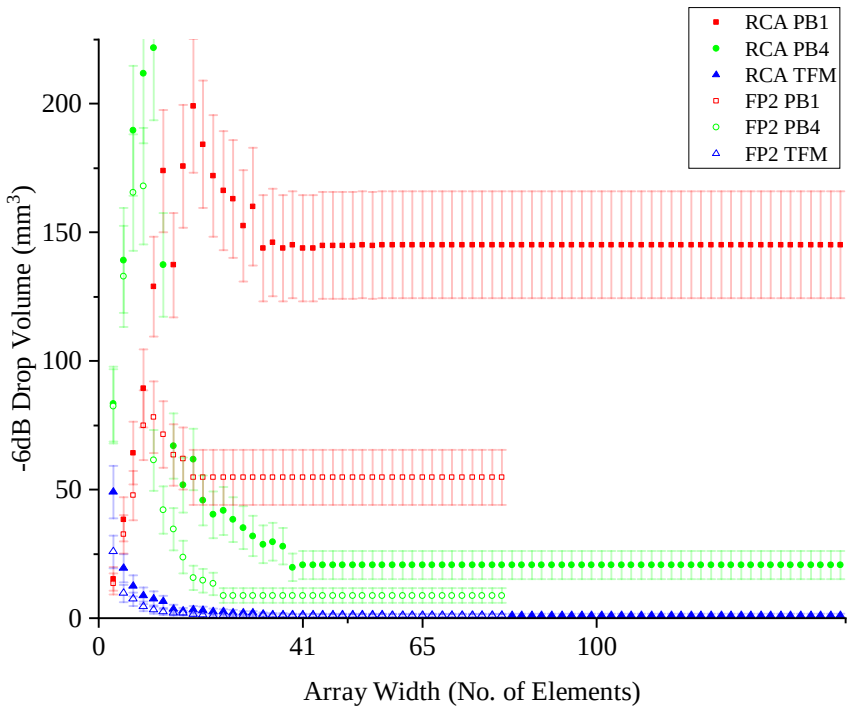

(a)

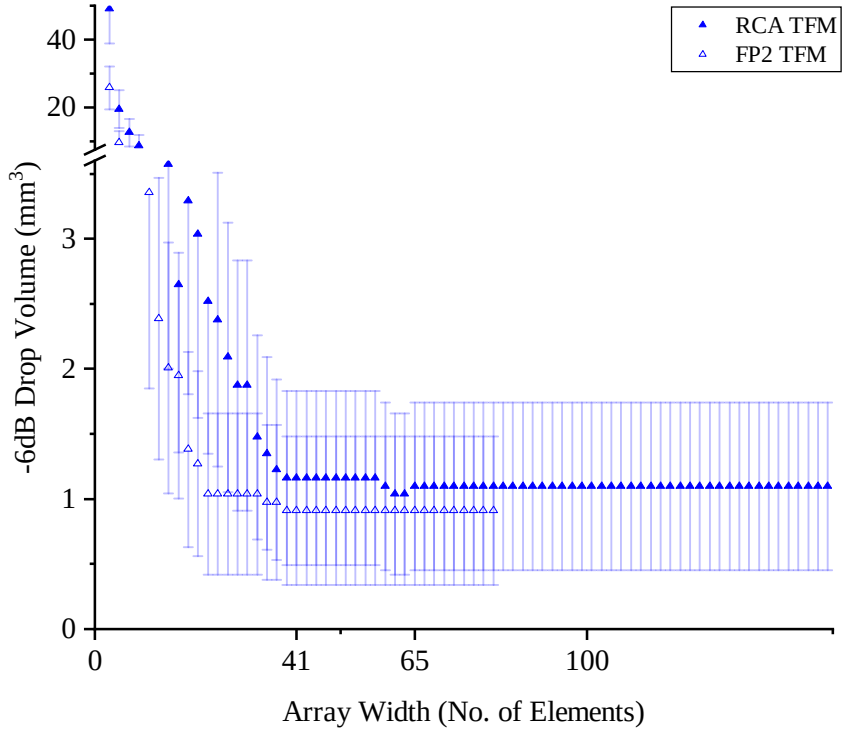

(b)

Figure 3.4: The $-6\,\mathrm{dB}$ drop volume of the PSF at $\mathbf{d} = (0, 0, -5)\mathrm{mm}$ as a function of n_e for (a) all imaging algorithms and arrays, and (b) for TFM based imaging algorithms only. A reduced number of error bars are shown for clarity.

number of transmit-receive combinations which contribute to a voxel causes $V_{-6\,\mathrm{dB}}$ to be artificially enlarged. At larger values of n_e, where $V_{-6\,\mathrm{dB}}$ of the PSF is contained beneath the array, the results become stable. It is shown in Figure 3.4b that the TFM algorithms for the FP2 array and the RCA array quickly become within error of each other after this point. From $n_e = 65$, the difference in $V_{-6\,\mathrm{dB}}$ is only $(0.2 \pm 0.9)\,\mathrm{mm}^3$. In terms of $V_{-6\,\mathrm{dB}}$, the TFM imaging performance of the FP2 array and the RCA array can be considered comparable after this point. However, it can be seen from Figure 3.2 and Figure 3.3, that outside of the $V_{-6\,\mathrm{dB}}$, the PSF for the RCA array is extended in all directions compared to the FP2 array. This is because of the defocussing in one direction in both transmit and receive. This is expected to result in a decrease in Signal-to-Noise Ratio (SNR) [36], and therefore detectability, when using RCA arrays as opposed to FP2 arrays experimentally. It has also been shown that the PB4 algorithm produced a smaller $V_{-6\,\mathrm{dB}}$ compared to the PB1 algorithm. This was in agreement with the prediction that, due to the increase in aperture size, the directivity function is narrower. The limit reached by the PB1 and PB4 algorithms in Figure 3.4a is because, once the $V_{-6\,\mathrm{dB}}$ is beneath the array, any elements added to the side of the array do not contribute to $V_{-6\,\mathrm{dB}}$. For the TFM based algorithms, the $V_{-6\,\mathrm{dB}}$ continues to decrease as more elements are added, but tends towards a limit as additional elements contribute less and less to the $V_{-6\,\mathrm{dB}}$ due to both directivity and beam spread. Beyond these effects, the diffraction limit sets the minimum value of $V_{-6\,\mathrm{dB}}$.

While these results indicate that the imaging performance, in terms of $V_{-6\,\mathrm{dB}}$, of FP2 and RCA arrays can be comparable when using the TFM algorithm, only a single PSF under the centre of the array was considered. The results cannot be generalised for all target locations; however, the approach is pragmatic given the computation time required. Given that the results are as expected, it is sensible to assume that the TFM algorithm will perform similarly well for both types of array for PSFs not under the centre of the array.

3.5 Conclusion

The imaging performance of FP2 and RCA arrays were compared using frequency domain modelling techniques. Three different imaging algorithms were applied to the modelled data in order to obtain the PSF. These consisted of two plane B-Scan algorithms, with apertures of $a = \ell_3$ and $a = 4\ell_3$, and the TFM algorithm. A RCA-adapted TFM algorithm was proposed in order to take account of the geometry of RCA arrays. The $-6\,\mathrm{dB}$ drop volume of the PSF was used as the comparison metric to compare the imaging performance. For a given n_e, RCA

arrays were found to perform worse than FP2 arrays for imaging in all cases. However, the imaging performance of RCA arrays was comparable to that of FP2 arrays when using the RCA-adapted TFM algorithm.

Experimental trials of large n_e FP2 arrays are not practically possible because of the large number of elements and the number of interconnections required between the elements. It is possible, however, to apply the RCA-adapted TFM algorithm to experimental data from a RCA array with a large value of n_e and compare the results to the conventional PB1 and PB4 algorithms for the same array.

Chapter 4

Improved Defect Detection and Sizing using DolphiCam

4.1 Introduction

In the previous chapter an adapted Total Focusing Method (TFM) algorithm was shown through modelling to improve the imaging performance of Row-Column Addressed (RCA) arrays compared to conventional Plane B-Scan algorithms. The modelling also showed that the imaging performance of RCA arrays was comparable to that of Fully Populated 2D (FP2) arrays when using the adapted TFM algorithm. If an improved performance can be demonstrated experimentally using the adapted TFM algorithm, then the likelihood of RCA arrays being used in the place of FP2 arrays will be increased. This would substantially reduce the required number of elements in an array needed for 3-Dimensional (3D) imaging. This adapted TFM algorithm has never been applied to data from an RCA array experimentally in the field of Non-Destructive Evaluation (NDE). This chapter shows the results of post-processing data from a commercial RCA array using three different imaging algorithms: two Plane B-Scan imagining algorithms with apertures of 1 and 4 elements, and the adapted TFM algorithm. A series of targets at a constant depth are imaged. The resulting images, their respective Signal-to-Noise Ratio (SNR), and the sizing performance of the three algorithms will be compared.

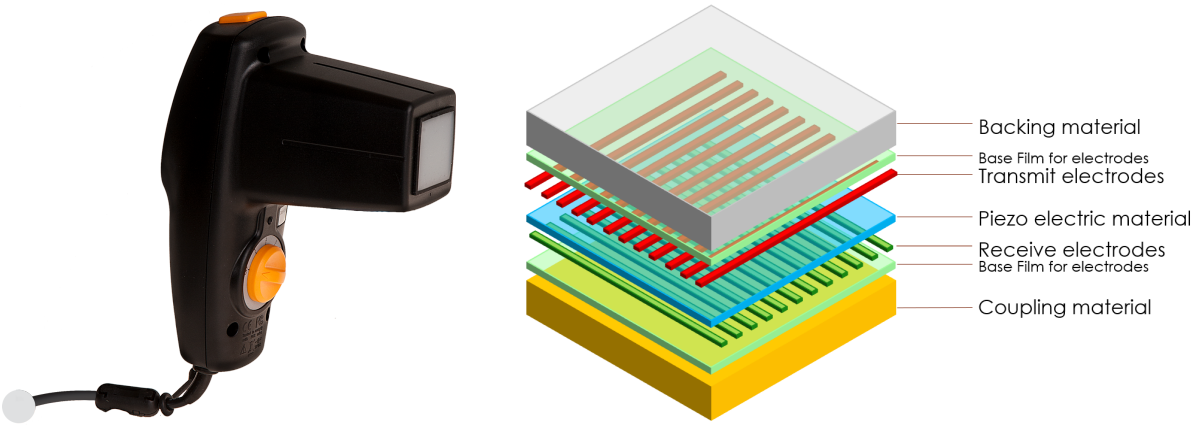

(a) (b)

Figure 4.1: (a) The DolphiCam device. (b) A schematic showing the construction of the DolphiCam array. © 2020 DolphiTech, both used with permission.

4.2 Method

4.2.1 Experimental Setup

4.2.1.1 Array

A suitable commercial RCA array was required in order to show any improvements in the imaging performance of RCA arrays experimentally. The DolphiCam (DolphiTech, Norway) is a RCA array with $n_e = 124$. A picture of the DolphiCam and its array construction is shown in Figure 4.1. In the array, perpendicular rows of electrodes are placed either side of a layer of piezoelectric material. The DolphiCam uses a soft, conformable silicone based coupling pad to make contact with the sample surface whether couplant is used or not. The array's other properties are listed in Table 4.1.

The DolphiCam software allows the export of the raw A-Scan data into a text format. The DolphiCam applies an additional delay in the software between transmission and data recording for each element transmit-receive combination. These delays are calibrated using the reflection from the coupling pad when the DolphiCam is not coupled to a sample. This means that the exported A-Scan data begins just before the interface between the coupling pad and the sample when in use. These delays are stored in a calibration file. The reason for these delays is not clear. It is assumed that these delays are used by the software to account for element flatness and coupling pad thickness non-uniformity when using the array for Plane B-Scan imaging. In general, a delay would also reduce the data transfer requirement.

Table 4.1: DolphiCam array parameters [1].

Parameter Name	Notation	Value	Unit
Array name	-	DolphiCam CF08	-
Centre frequency	f_0	3.5 [1]	MHz
Bandwidth $(-6\,\mathrm{dB})$	Δf	50% [1]	-
Array width	n_e	124	No. of elements
Total number of elements	N_e	248	-
Element width	ℓ_1	0.210	mm
Element length	ℓ_2	30.96	mm
Element pitch	ℓ_3	0.250	mm
Coupling Pad			
- Nominal thickness	ℓ_4	3	mm
- Longitudinal wave velocity	v_l	950	$\mathrm{m\,s^{-1}}$

[1] Approximate values estimated from the frequency spectrum provided.

An example calibration file is shown graphically in Figure 4.2. The sampling frequency of the DolphiCam is fixed at $64\,\mathrm{MHz}$. The example calibration time values in Figure 4.2 have a range of 28 bins. This would equate to a change in element position or coupling pad thickness of $\approx 0.2\,\mathrm{mm}$ (1 s.f.). This variation is expected to be due to tolerances in the array or coupling pad manufacturing or fabrication processes.

The device uses two square waves in quick succession to excite the transducer when transmitting ultrasound. This is done to increase the amount of energy going into the sample to increase the signal-to-random-noise ratio of the received signals. If not removed through signal processing, the double square wave excitation would cause every reflection to appear twice in each A-Scan. Therefore, a matched filter, using cross-correlation, is used by the device by default [1] to remove these repeated responses.

4.2.1.2 Sample

An acrylic test sample was manufactured in order to assess the performance of the imaging algorithms. Acrylic was chosen because it closely matches the acoustic properties of Carbon Fibre Reinforced Polymer (CFRP) for which the DolphiCam was designed. However, unlike CFRP, acrylic is homogeneous which matches the modelling conditions used in Chapter 3. The test sample was $8\,\mathrm{mm}$ thick and contained a $0.3\,\mathrm{mm}$ diameter Conical Bottom Hole (CBH) as well as a series of Flat Bottom Holes (FBHs) with diameters of $1\,\mathrm{mm}$, $2\,\mathrm{mm}$, $4\,\mathrm{mm}$, $5\,\mathrm{mm}$ and $10\,\mathrm{mm}$. These were all drilled to a depth of $3\,\mathrm{mm}$, which meant that their

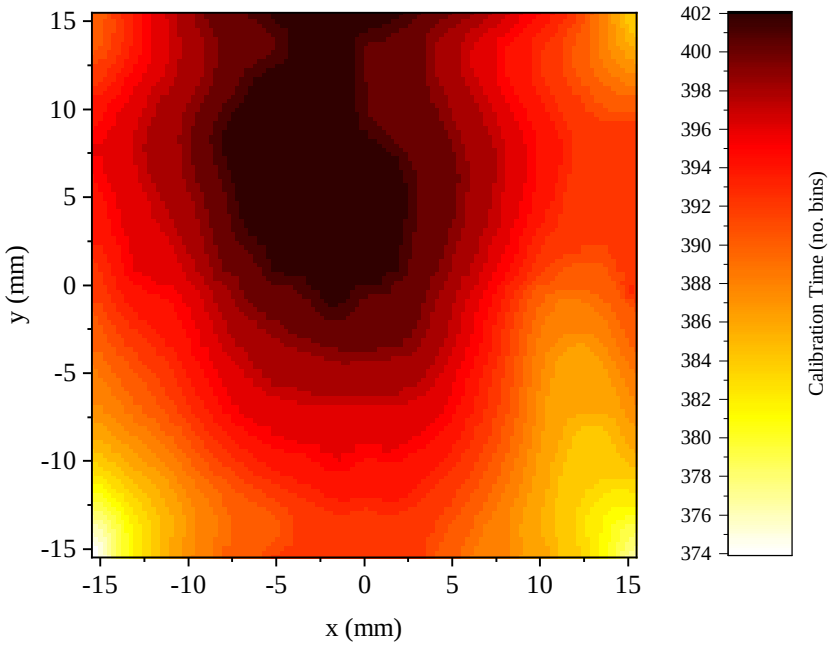

Figure 4.2: Delays obtained from an example calibration file from the DolphiCam. The delay between transmission and the start of data collection for each transmit-receive combination is shown in terms of the number of bins. The sampling frequency of the device is $64\,\mathrm{MHz}$.

tips were approximately $5\,\mathrm{mm}$ deep when measured from the scanning surface. The $0.3\,\mathrm{mm}$ CBH was chosen as the smallest target defect to try to resolve experimentally. It is below the half-wavelength diffraction limit of $\approx 0.4\,\mathrm{mm}$ (1 s.f.). The FBHs were chosen because they have a response similar to delaminations which are commonly sought defects for detection and sizing in CFRP.

4.2.1.3 Data Collection

12 complete and independent datasets were taken for each target using a single element aperture in transmit and receive. 8 software averages were taken for each A-Scan using the manufacturer's software and no focussing was used when collecting the data. The matched filter was used during data collection. The raw data were then extracted from the device and stored along with the calibration file containing the recording delays. Couplant was used to improve coupling performance. 12 complete and independent datasets were also taken from areas of the acrylic sample where no targets were located.

4.2.2 Imaging

When imaging the experimental data, a broadband frequency domain Gaussian filter with $\Delta f \approx 150\%$ was applied to the raw A-Scans before any further processing was carried out.

4.2.2.1 Adjusting for the Coupling Pad

The coupling pad in the DolphiCam device acts as a stand-off which is similar to that used for normal arrays in industry. Unlike normal stand-off materials though, the DolphiCam coupling pad is conformable. The coupling pad adds two complications to the imaging process. Firstly, the coupling pad has a very low longitudinal velocity. This means that there is a large amount of refraction at the interface between the coupling pad and the sample. Secondly, the flexible nature of the coupling pad means that the array is not generally parallel to the surface, and the coupling pad thickness is a function of position. If the exact geometry of the interface between the coupling pad and the sample was not used when calculating the delay laws in post processing, the accuracy of the delay law calculation would be decreased. This issue is further exacerbated by the issue of strong refraction at that interface. All of this will increase the uncertainty in which time point from the A-Scan should be chosen to contribute to a voxel in the image and will generally increase noise in the image.

The complexity of this problem means that a solution is difficult to implement. For a linear array, or for a FP2 array with a small number of elements, the computation time for calculating the surface profile and then calculating the refracted path is achievable. For a FP2 array with a large number of elements, the calculation itself is achievable but computationally heavy [37]. For a large RCA array, due to the elongated and overlapping elements, the calculation itself is more complicated and it is still prohibitively computationally time consuming.

Therefore the simplest case was considered here, with a view to expanding the complexity of the solution if the results were not of a suitably high standard. The simplest case tested was that the array was perfectly parallel to the sample surface and therefore that the coupling pad had a uniform thickness at every point. This approximation was used throughout this chapter. To calculate a singe value of coupling pad thickness, the location of the maximum of the absolute of the Hilbert envelope within the first 50 time points in every A-Scan was calculated. An average of these values was then taken and used to calculate a single value of coupling pad thickness. An example of this calculation is shown for the first 300 transmit-receive combinations in Figure 4.3.

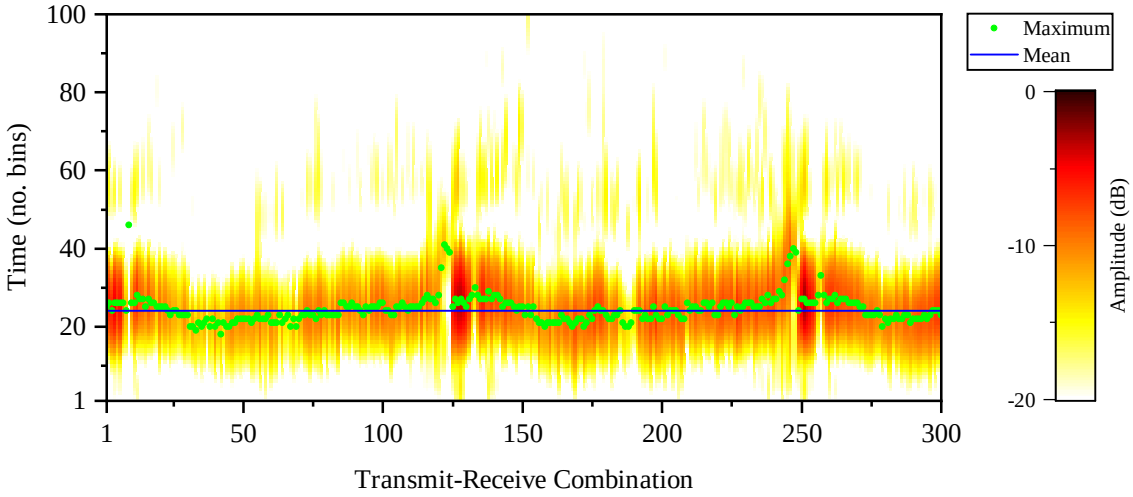

Figure 4.3: An example image showing how a single value for the thickness of the coupling pad is calculated. The first 300 transmit-receive combination A-scans are shown for the first 100 time points. The sampling frequency of the device is 64 MHz. The maximum of the absolute of the Hilbert envelope within the first 50 time points for each A-Scan is shown in green. The mean of these values across all transmit-receive combinations is shown as a blue horizontal line.

The Plane B-Scan algorithm for RCA arrays described in Section 3.2.2 was used for the experimental work in this chapter. The travel time in the coupling pad for all elements was calculated using the single value of coupling pad thickness. This was taken into account in the imaging algorithm in the usual way.

When the adapted TFM algorithm described in Section 3.2.2 was applied experimentally, the refraction at the interface was taken into account for each leg. The interface was discretized and the shortest time path for each element to interface point to voxel combination was calculated in 2-Dimensional (2D) [Figure 4.4]. The symmetry of the array was used to reduce the number of these calculations performed. An angle limit of $\theta_{\text{limit}} = 30°$ was used during all experimental implementations of the adapted TFM algorithm.

The same division of the amplitude of each voxel by the number of transmit-receive combinations which contribute to it was also implemented in the experimental setup. This was especially important as there was a combination of angle limiting and a large amount of refraction. This meant that the range of contributions per voxel across the image was large. This division by the number of contributions helps to normalise the response from reflectors at different locations. Without it, responses from a reflector at each voxel would vary considerably

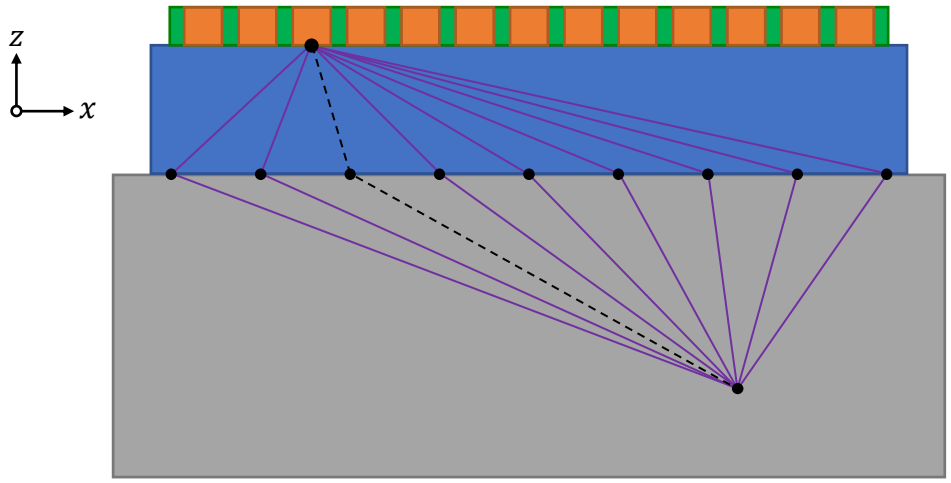

Figure 4.4: The discretization of the interface between the coupling pad and the sample used for the delay law calculation. The shortest time path, shown in dashed black, was chosen from all the possible paths, shown in purple, between the element and the voxel. The 2D calculation is shown for transmission. Where symmetry allows, only the path calculations for either transmission or reception in 2D need to be calculated for any element-to-voxel combination.

more in amplitude and the results would become difficult to interpret.

All the data were processed using the imaging algorithms described above, including data collected on areas of the sample which did not contain targets.

4.2.2.2 Detectability and Sizing

Due to the targets in the sample being too close together, the edge of another target was sometimes imaged at the same time as the intended target. A region of interest was chosen which contained only the intended target to combat this. The region of interest was defined as $(-13\,\mathrm{mm} \leq x, y \leq 13\,\mathrm{mm})$ and $(-6\,\mathrm{mm} \leq z \leq -4\,\mathrm{mm})$. The depth constraint was chosen so that only voxels around the depth of the target $z \approx -5\,\mathrm{mm}$ were used.

The images from data recorded where no targets were located on the sample were used to calculate the noise level. The Root Mean Square (RMS) of the amplitudes of the image voxels in the region of interest was calculated for each dataset and each imaging algorithm. The mean of the RMS for each of the 12 datasets was calculated to give a single RMS noise value for each imaging algorithm. An arbitrary conservative detectability threshold of $15\,\mathrm{dB}$ above the RMS noise level was set for a target to be classed as successfully detected.

The data taken over the FBHs were processed using an automated procedure which aimed to calculate the the maximum width dimension of each FBH. For each image, the maximum amplitude within the region of interest, p_{max}, was found. The location of this maximum was denoted $\mathbf{p}_{\text{max}}$. If $p_{\text{max}} \geq 15\,\text{dB}$ then sizing was carried out using the following automated procedure. All voxels within the region of interest that satisfied the condition $|(\mathbf{p} - \mathbf{p}_{\text{max}}) \cdot \hat{\mathbf{z}}| \leq 0.05\,\text{mm}$ were selected in order to take account of any small deviations in surface height or orientation of the FBH. The amplitudes of these voxels for different z at each (x, y) location were condensed into a single amplitude by taking the maximum. As $-6\,\text{dB}$ drop sizing was to be used, all voxels in the, now 2D, image which satisfied the condition $p \geq (p_{\text{max}} - 6\,\text{dB})$ were selected. For images with a low SNR, random noise caused voxels outside of the defect cluster to meet the selection criteria. These outliers were removed from the selection if they were more than three scaled geometric median absolute deviations away from the geometric median. Finally, the maximum width dimension of the FBH was given by the maximum distance between any two of the remaining selected voxels. This process was repeated for all 12 datasets for each defect. The mean was used to give a best estimate of the $-6\,\text{dB}$ drop width and the standard error was used to quantify the uncertainty. An example set of experimental data from stages of this automated procedure are shown in Figure 4.5, Figure 4.6 and Figure 4.7.

4.3 Results

The responses of the DolphiCam array to different targets located at a depth of approximately $5\,\text{mm}$ in acrylic were measured and imaged for all imaging algorithms considered. Example B-Scan and C-Scan images for each hole considered are shown in Figure 4.8 and Figure 4.9 respectively. The images are shown using a decibel scale which is normalised to the amplitude of the RMS noise and has a $40\,\text{dB}$ dynamic range. The maximum value on the scale is equal to the maximum amplitude within the region of interest. Finally, the DolphiCam array responses, imaged using all the imaging algorithms considered, were used to size the diameters of the FBHs. The $-6\,\text{dB}$ drop widths of the FBHs are compared to the drill bit diameter used to make them in Figure 4.10. The average difference between the $-6\,\text{dB}$ drop width and the nominal drill bit diameter across the whole range of FBHs was $(2.08 \pm 0.05)\,\text{mm}$, $(1.33 \pm 0.05)\,\text{mm}$ and $(0.12 \pm 0.03)\,\text{mm}$ for PB1, PB4 and TFM imaging algorithms respectively.

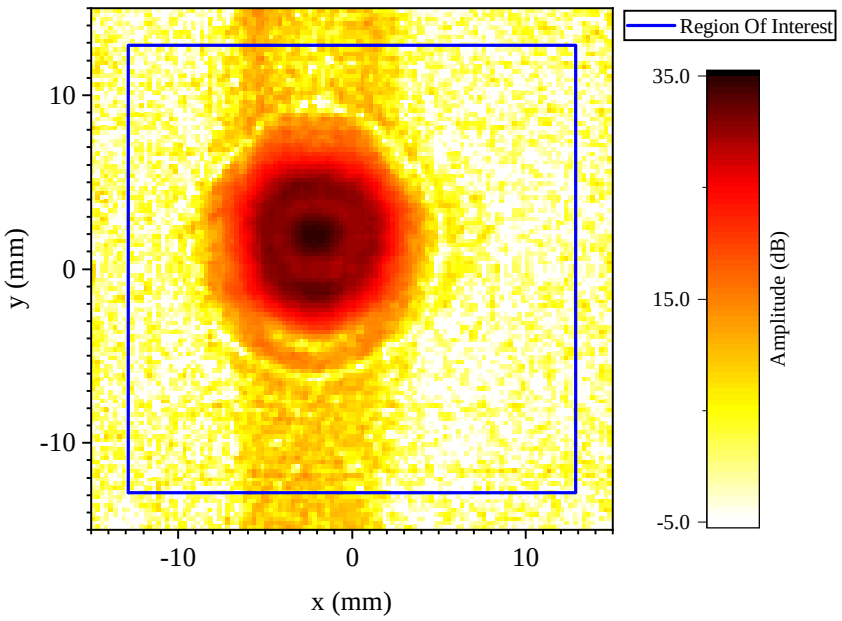

Figure 4.5: An example C-Scan slice at the depth at which the maximum amplitude within the region of interest occurs for the $10\,\mathrm{mm}$ FBH. The region of interest is indicated schematically. The decibel scale is normalised to the RMS noise level. The maximum value on the scale is the maximum amplitude within the region of interest. The image is shown with a $40\,\mathrm{dB}$ dynamic range.

4.4 Discussion

The SNR for the smallest target considered, the $0.3\,\mathrm{mm}$ CBH, was improved using the RCA-adapted TFM algorithm. This improvement led to the response being above the $15\,\mathrm{dB}$ detectability threshold, while the next highest response, using the PB4 algorithm, was below the threshold [Figure 4.8 and Figure 4.9]. The SNR benefits of the RCA-adapted TFM algorithm decrease as the FBH diameter increases. This is expected to be because the orientation of the FBHs is parallel to the sample surface and so the PB1 and PB4 algorithms are aligned to the high amplitude specular reflection from the FBH. The RCA-adapted TFM algorithm uses a much larger set of A-Scans which contain, in addition, many other signals which contribute very little apart from noise. The responses from the holes in Figure 4.8 and Figure 4.9 do not show the side lobes seen in Figure 3.2 and Figure 3.3 for the PB1 and PB4 algorithms. This is because of the refraction at the interface between the coupling pad and the sample. At this interface, the critical angle for longitudinal waves is $\theta_{\text{crit.}} \approx 20^\circ$ (1 s.f.). Therefore the coupling pad not only stops the edge waves propagating into the sample below the centre of the array, but also increases the applicability of the intersection approximation used for the PB1 and PB4 algorithms by narrowing the directivity function in terms of the waves propagating into

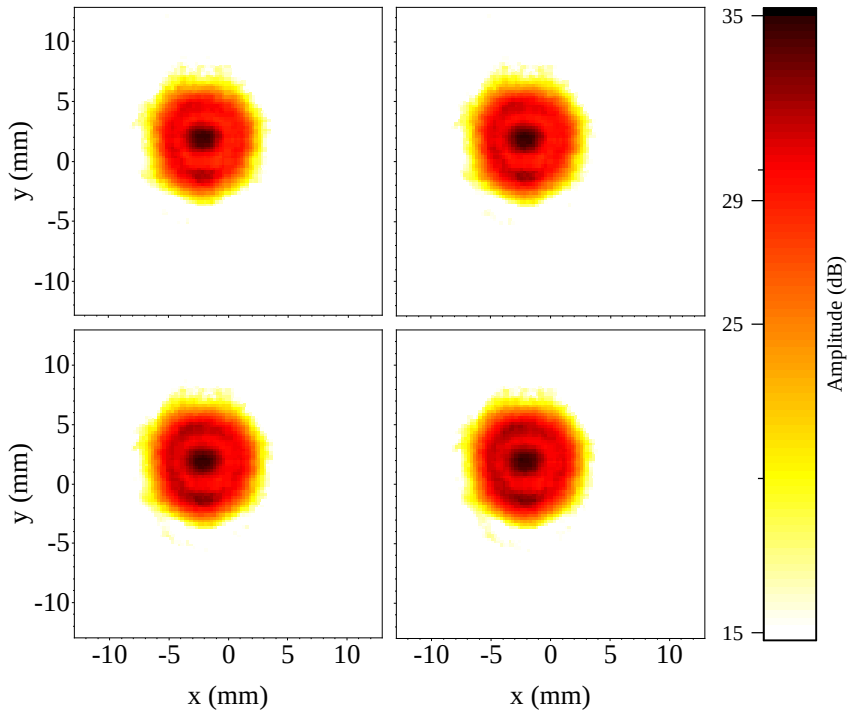

Figure 4.6: Example C-Scan slices at the depths which satisfied the condition $|(\mathbf{p} - \mathbf{p}_{\max}) \cdot \hat{\mathbf{z}}| \leq 0.05\,\mathrm{mm}$. The decibel scale is normalised to the RMS noise level. The maximum value on the scale is the maximum amplitude within the region of interest. The minimum value on the scale is denoted by the $15\,\mathrm{dB}$ detectability threshold. The $-6\,\mathrm{dB}$ drop value, $29\,\mathrm{dB}$, is also indicated on the decibel scale for reference.

the sample. The coupling pad also reduces the benefits of a broad directivity function used by the RCA-adapted TFM algorithm. In the absence of a coupling pad, the literature shows that side lobes have been successfully reduced using element apodisation outside the main array area. This would allow the use of the broad directivity function of the elements to be maximised for the RCA-adapted TFM algorithm. The extension of the response, in terms of depth, from the holes seen for all algorithms in Figure 4.8 is caused by the long length in time of the transmission pulse, which is approximately 5-cycles. The extension of the response, in terms of width in the y direction, from the $4\,\mathrm{mm}$, $5\,\mathrm{mm}$ and $10\,\mathrm{mm}$ diameter FBHs seen in all algorithms in Figure 4.9 is caused by the transducer design asymmetry, that is that each set of electrodes above and below the piezoelectric material are orthogonal.

Finally, the accuracy and precision of sizing the FBHs in acrylic has been improved by using the RCA-adapted TFM algorithm. The average difference across the whole range of FBH diameters has been improved by a factor of about 11. Figure 4.10 shows that the RCA-adapted

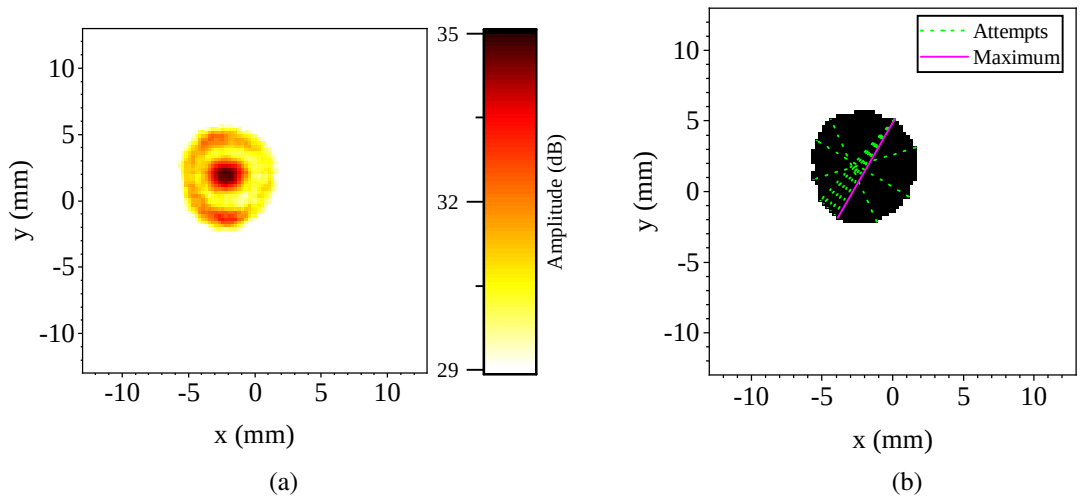

Figure 4.7: (a) An example C-Scan image created by taking the maximum amplitude at each (x, y) location for all z which satisfied the condition $|(\mathbf{p} - \mathbf{p}_{\text{max}}) \cdot \hat{\mathbf{z}}| \leq 0.05\,\text{mm}$. The decibel scale is normalised to the RMS noise level. The maximum value on the scale is the maximum amplitude within the region of interest. The minimum value on the scale is denoted by the $-6\,\text{dB}$ drop value. (b) An example image showing, in black, all of the pixels in (a) which are above the $-6\,\text{dB}$ drop value. Some example lengths found by the sizing algorithm are shown in green. The maximum distance between any two black pixels is indicated in pink.

TFM algorithm consistently performs better than the PB1 and PB4 algorithms across the full range of FBH diameters. The systematic error in the $-6\,\text{dB}$ drop width for the PB1 and PB4 algorithms towards the higher diameters of FBHs is caused by the beam profile not being circular for the RCA array. The PB1 algorithm overestimates the $-6\,\text{dB}$ drop width at lower diameters of FBH because the SNR of the images is very low. The PB4 algorithm behaves as expected towards the lower diameters of FBH as it reaches a sizing limit roughly proportional to its beam size [38]. Accurate values of beam size are difficult to calculate because of the refraction at the coupling pad. The sizing limit for the RCA-adapted TFM algorithm was not reached and so cannot be conclusively stated in this paper. However, it cannot be below the half-wavelength diffraction limit of $\approx 0.4\,\text{mm}$ (1 s.f.).

As linear arrays are predominantly used in industry, it is interesting to consider a theoretical comparison between a linear array and a refined RCA array. It is expected that, because of the results in Chapter 3, a refined RCA array would perform similarly to an FP2 array when using the TFM. As an FP2 array provides an additional focussing direction, an FP2 array would be expected to perform better than a linear array in most situations. Therefore, it is expected that a refined RCA array would outperform a linear array.

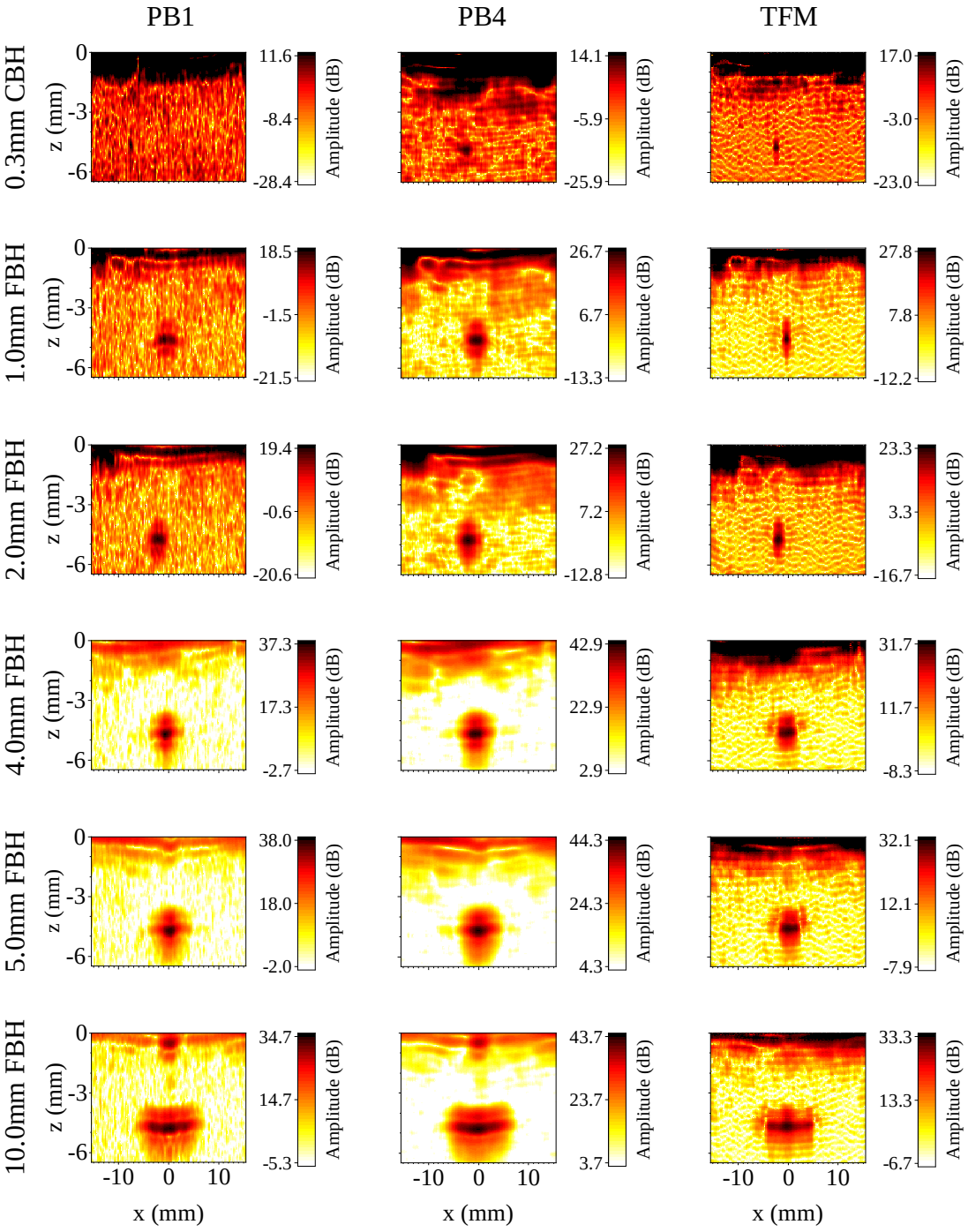

Figure 4.8: B-Scan images of a range of holes in acrylic at a depth of approximately $-5\,\mathrm{mm}$. Increasing defect diameters are shown from top to bottom. PB1, PB4 and TFM imaging algorithms are shown from left to right respectively.

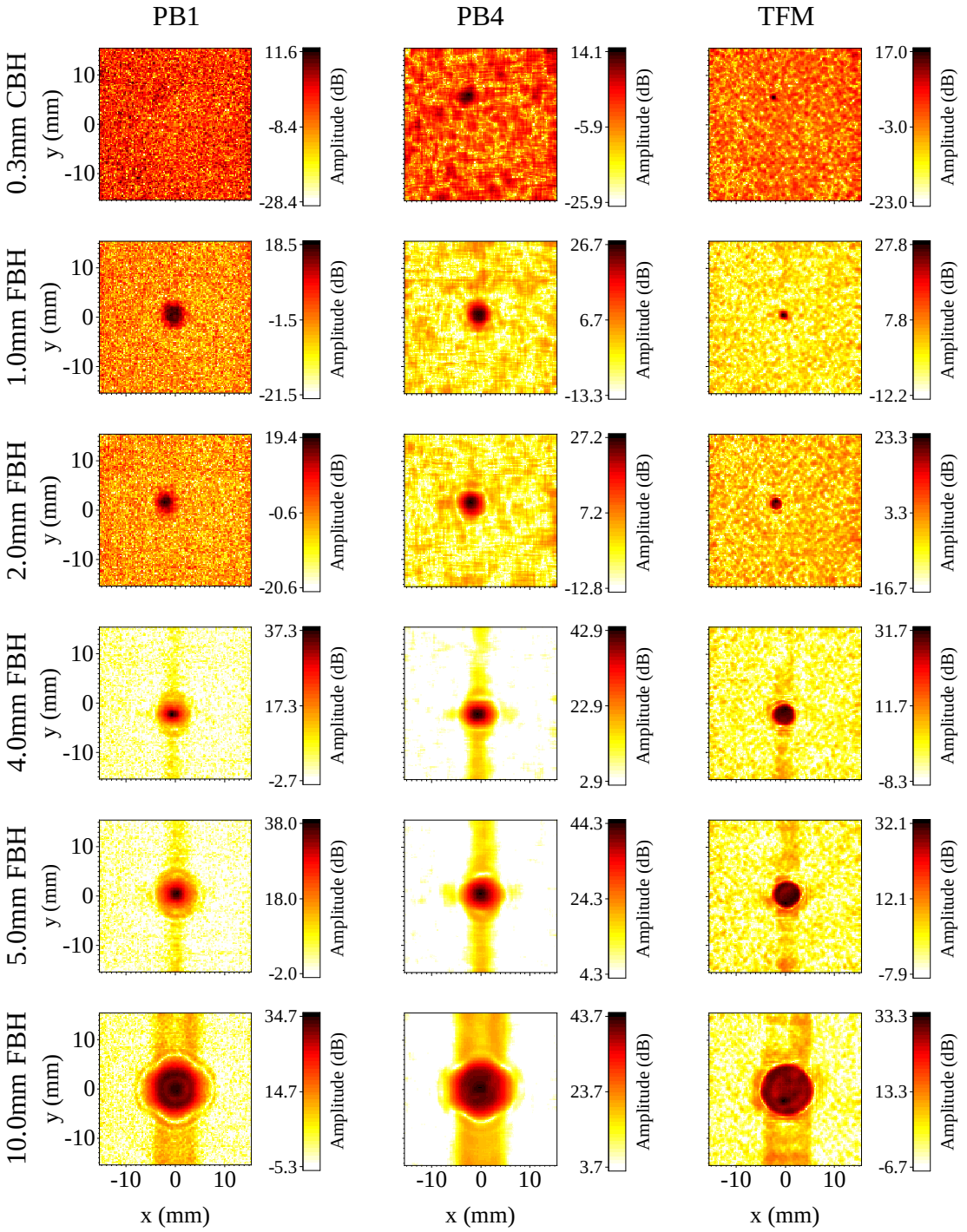

Figure 4.9: C-Scan images of a range of holes in acrylic at a depth of approximately $-5\,\mathrm{mm}$. Increasing defect diameters are shown from top to bottom. PB1, PB4 and TFM imaging algorithms are shown from left to right respectively.

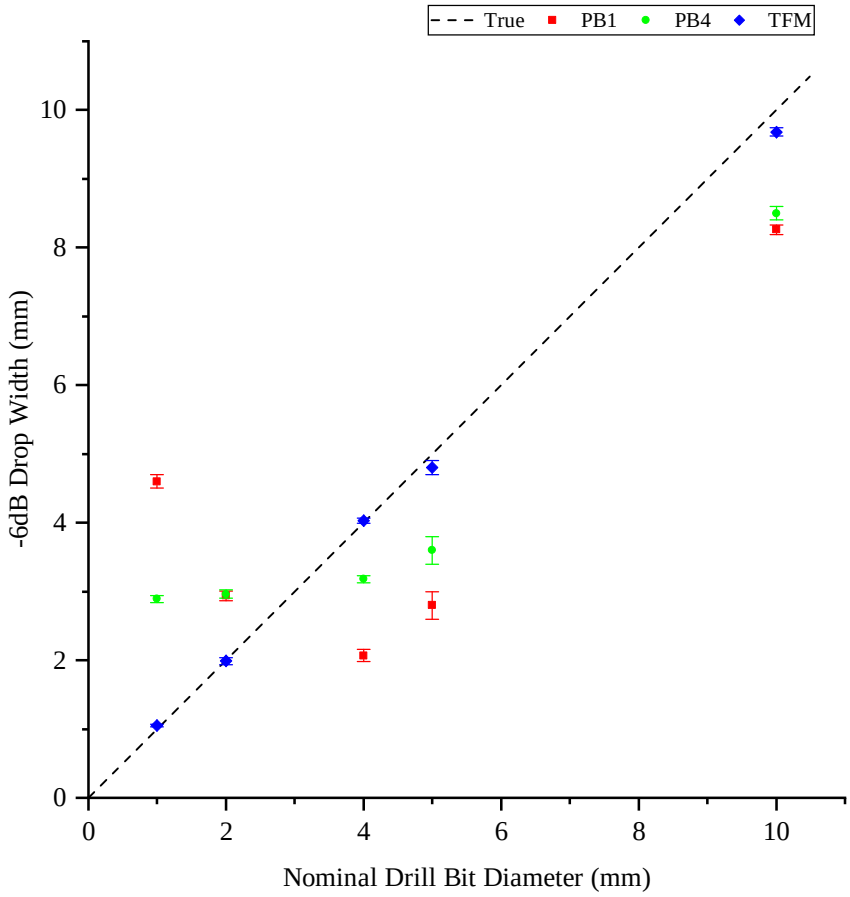

Figure 4.10: The sizing of FBHs in acrylic experimentally using the DolphiCam array.

4.5 Conclusion

The imaging performance of RCA arrays using the Plane B-Scan algorithm and the RCA-adapted TFM algorithm was compared experimentally. The RCA-adapted TFM algorithm was shown experimentally to improve the imaging performance in respect to the detectability of a very small defect. The RCA-adapted TFM algorithm also improved the accuracy and precision of sizing FBHs. These experimental results show a similar improvement to that predicted by the modelling in the advantages of using the RCA-adapted TFM algorithm instead of the Plane B-Scan algorithm when using RCA arrays. These results indicate that the performance of RCA arrays should be comparable to FP2 arrays when using the RCA-adapted TFM algorithm.

Chapter 5

Diffuse Fields and Laser Ultrasonic Arrays

5.1 Ultrasonic Diffuse Fields

A wave field within a specimen that has been scattered many times from geometric features or defects can be described as a diffuse field. This definition is usually satisfied after a considerable time has elapsed. In a theoretical diffuse field the Root Mean Square (RMS) of the particle displacement is the same at all locations, all propagation directions for wave energy equiprobable, and the energy at one point is proportional to the total energy in the system [39, 40]. In dissipative systems the energy in the specimen can be lost and so the total energy in the field tends to zero with increasing time. When measuring diffuse fields experimentally this leads to a trade-off between how diffuse a field is and the signal-to-random-noise ratio of the measured signal. The speed at which the field becomes statistically diffuse can be increased by complex geometries and the presence of many scatterers. Large specimens, however, can degrade the speed of this convergence as the energy needs to be distributed evenly around a larger volume of material.

The study of diffuse fields of elastic waves in solids was first investigated by Egle in 1981 using methods from studies of room acoustics [41]. The study was initially focussed on acoustic emission events and the relative ratios of the energy in different bulk wave modes. This was followed shortly afterwards by Weaver who extended the problem to include surface waves [42], waves in plates [43] and other excitation events [44]. Diffuse fields were finally used in the Non-Destructive Evaluation (NDE) of materials in 1987 when Weaver used the decay of the diffuse field as a function of time for the accurate calculation of ultrasonic attenuation

through internal absorption [45]

Throughout these works the diffuse field was assumed, although not proved, to be a random and incoherent field. The decay in energy of the diffuse field then became the primary means of applying the diffuse field to NDE [46]. Then, in 2001, Lobkis and Weaver demonstrated that cross-correlations of a diffuse field recorded at two receivers reconstructed the Green's function between the two receivers. The authors went on to show that the time derivative of auto-correlations of the diffuse field at a single receiver, recording only thermal noise in the sample, reconstructed the pulse-echo response of the receiver [48, 49, 50]. Details of the accuracy and convergence of the reconstruction are given in [51] and [52]. An understandable explanation as to why this phenomenon occurs is given in [53] and a review paper on these methods, with particular application to seismology, was produced by Goudard et al. in 2008 [54].

Despite the original papers on this reconstruction method covering a metal sample containing geometric reflectors and using transducers at ultrasonic frequencies, very little application to NDE was made. In 2010 Duroux et al. used the reconstructed signals for guided wave tomography in a plate containing simulated structural damage [55] with a similar approach adopted in [56]. In the area of ultrasonic array imaging, Potter et al. used the linear properties of the reconstructed Green's function to remove non-linear near surface saturation effects to image near surface targets [57].

The fact that diffuse field signals can be used to image material structure is not in itself as surprising as it first sounds. The intuitive explanation in [53] and [51] is also given here. Visualisation of the problem requires only two receivers immersed in a diffuse field. At some point a wave will pass through both receivers along some path. The two signals recorded at the receivers from this wave will look similar but will not necessarily arrive at the same time. The cross-correlation of the full time domain signals from the two receivers will produce a peak where the signals from the wave align in time. This will be at the time it took for the wave to travel the path between the two receivers. The signals at the two receivers are not free from noise however, and so the cross-correlation will also produce a large number of other peaks not associated with the wave travelling between the two receivers. This is called reconstruction noise, and can swamp the desired signal. Reconstruction noise can be suppressed by averaging over a large number of wave arrivals, typically done by cross-correlating large amounts of time or cross-correlating signals from a number of excitation locations. It is inter-

esting to note that if the diffuse field signals are repeatable, then so is the reconstruction noise. Obviously the reconstruction noise is coherent and not random.

The derivation of the equations used for reconstructing the early time signals is given in [47], but their simplified form is as follows. The time domain late time array response matrix containing the diffuse field data is denoted by $g_{tr}(\tau)$ where t and r denote the indices of a transmitter and receiver located at $\boldsymbol{e_t}$ and $\boldsymbol{e_r}$ respectively and τ is time. An approximation to the time domain early time full array response matrix element $h_{r_1r_2}(\tau)$ can be calculated by cross-correlating $g_{tr_1}(\tau)$ and $g_{tr_2}(\tau)$. The cross-correlation is only applied over a specific window of time, here referred to as the reconstruction window, between τ_1 and τ_2. This cross-correlation operation is best applied in the frequency domain where cross-correlation is just a multiplication of one term with the complex conjugate of the other.

The Fourier transform of the signal within the reconstruction window is calculated using the equation:

$$\tilde{g}_{tr}(\omega) = \int_{\tau_1}^{\tau_2} g_{tr}(\tau)\, e^{-i\omega\tau}\, \mathrm{d}\tau, \tag{5.1}$$

where ω is the angular frequency and $i = \sqrt{-1}$. The angular frequency is given by $\omega = 2\pi\nu$ where ν is the frequency. The result is then cross-correlated using the full reconstruction equation [47]:

$$\tilde{h}_{r_1r_2}(\omega) \approx \frac{i\omega\tilde{g}_{tr_1}(\omega)\tilde{g}^*_{tr_2}(\omega)}{a(\omega)\tilde{f}(\omega)} \frac{\Psi_{r_2}(\omega)}{\Psi^*_{r_2}(\omega)}, \tag{5.2}$$

where $*$ denotes the complex conjugate, $\Psi_{r_2}(\omega)$ is the transfer function of the receiver r_2, $a(\omega)$ is a correction factor and $\tilde{f}(\omega)$ contains the adjusted auto-correlation of the time domain late time pulse-echo signal of the transmitter. $\tilde{f}(\omega)$ is given by:

$$\tilde{f}(\omega) = \sqrt{\tilde{g}_{tt}(\omega)\tilde{g}^*_{tt}(\omega)}, \tag{5.3}$$

where $\tilde{g}_{tt}(\omega)$ is the frequency domain late time pulse-echo signal of the transmitter.

Conceptually, it can be understood that the $\tilde{f}(\omega)$ term exists because cross-correlating $g_{tr_1}(\tau)$ and $g_{tr_2}(\tau)$ would produce a squared frequency domain response without the normalisation provided by $\tilde{f}(\omega)$. Also, it is logical that the cross-correlation of $g_{tr_1}(\tau)$ and $g_{tr_2}(\tau)$ might naturally reconstruct a mixture of both $h_{tt}(\tau)$ and $h_{r_1r_2}(\tau)$ and that it is therefore desirable to remove the transmission component from the reconstructed signal.

The correction factor, $a(\omega)$, although complicated in composition, varies only slowly with frequency [47] and as such can be approximated to a constant of no real consequence to ignore. Similarly, the phase shift, $\frac{\Psi_{r_2}(\omega)}{\Psi^*_{r_2}(\omega)}$, is difficult to calculate and is ignored by Lobkis and Weaver in their example experimental implementation.

5.2 Laser Ultrasonics

5.2.1 Laser Generation of Ultrasound

In addition to electro-mechanical devices for generating ultrasound, ultrasound can also be generated using opto-mechanical means [58]. Typically a pulsed laser source is used, due to its short pulse length and high coherence, to illuminate the surface of a specimen with a short high intensity burst of light. This causes local heating of the surface. The surface expands rapidly, creating a pressure wave in the material. The pulse length used can be chosen so that the resulting pressure waves are in the ultrasonic frequency regime. The main benefit of laser generation of ultrasound comes from the fact that it is non-contact. This enables the remote excitation of ultrasound inside a material from considerable distances. Laser generation of ultrasound is more favourable still because the light only needs to get to the surface of the specimen, not back again, unlike detection of ultrasound using lasers which is described below. A second benefit of laser generation of ultrasound is that it produces a broadband frequency spectrum input pulse. This is simply because the excitation signal is typically a very short width pulse very similar to a Delta function in the time domain.

In NDE, thermoelastic, rather than ablative, sources are preferred. Ablative sources have a more favourable directivity pattern but, because material is removed during generation, cannot be considered truly non-destructive [59]. When using thermoelastic sources with metallic materials the absorption depth of the laser light at the surface is very shallow. For this reason, these sources are often modelled as force dipoles orientated parallel to the surface. There is assumed to be no force component perpendicular to the surface. These sources produce much more complicated directivity patterns, which also have more complicated relationships to source size [59]. Typically, the directivity patterns comprise of a broad lobe with a maximum at approximately 65° for longitudinal waves and a main sharp lobe with a maximum at approximately 30° for shear waves [60]. Both directivity patterns go to approximately zero perpendicular to the surface. Directivity patterns for both thermoelastic and ablative sources,

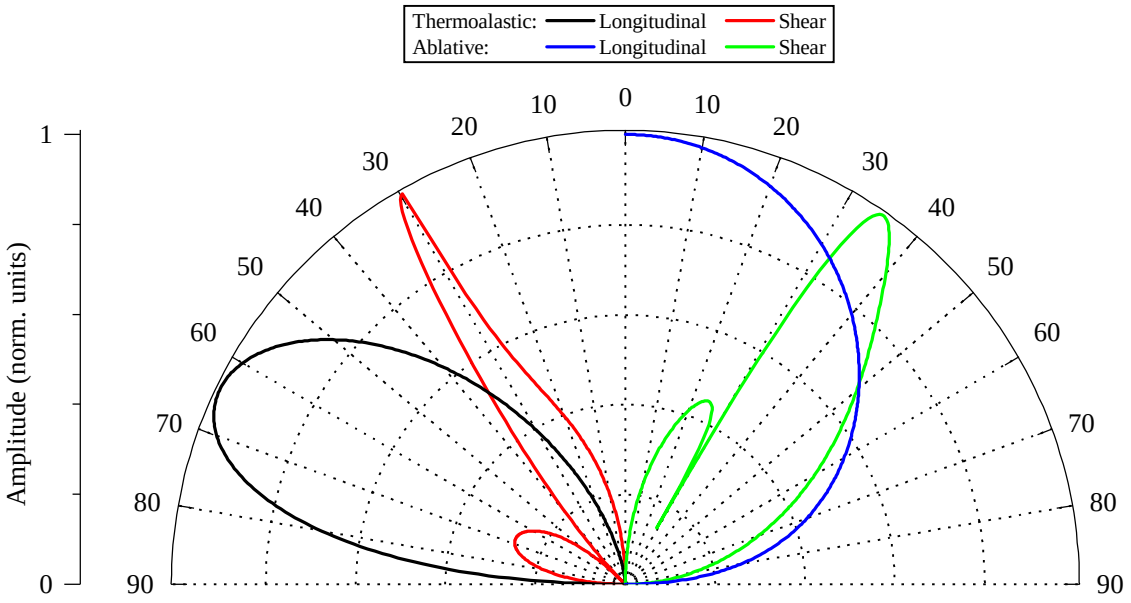

Figure 5.1: Normalised directivity patterns for laser generated ultrasound using thermoelastic and ablative sources. The directivity patterns for both longitudinal and shear waves is shown. Each directivity pattern is symmetric about $0°$. Only half of each directivity pattern is shown for clarity.

calculated using the formulae in [18] and [10] respectively, are shown in Figure 5.1.

5.2.2 Laser Detection of Ultrasound

Ultrasound can be detected locally at a specimen surface using interferometry. This is usually done through the interference of two beams of light.

Between the two extremes of constructive and destructive interference, the amplitude of the interfered beam varies sinusoidally with the phase difference between the two beams. This enables the phase difference between the two beams of light to be measured. If two beams, in phase at some coherence point, each arrive at a surface some distance away, then on reflection back to that coherence point their phases are the same. However, if the two beams travel to surfaces that are different distances away from the coherence point then their phases on return could be different. If the difference in the distance from the coherence point to the two surfaces were equal to a phase shift of $n\pi$, where $n = 1, 3, 5, ...$, then the relative phase shift on return would be an integer multiple of 2π. However, between the zero and the π, half-wavelength, limit, there is a regime where the difference in phase is measurable and the

distance difference can be calculated.

Now imagine the two beams incident on a single surface some distance away from the coherence point. However this time their departure from the coherence point is separated by some time, an integer of the wave period. The beams will therefore arrive at the sample surface separated in time. If the sample has moved away from the coherence point between the arrival of the first and second beams, the second beam will travel further than the first before being reflected. This distance travelled results in the phase of the second beam being different to the phase of the first beam on their subsequent arrival back at the coherence point. We can now measure a phase difference, and therefore the distance moved by the surface can be calculated. In effect, we have the average velocity of the surface between those two points in time. If the time separation of the beams arriving at the surface is such that the surface can perform multiple movements between the arrival of the first beam and the second beam then these movements cannot be known. To correctly characterise these movements, the time separation of the beams must be reduced such that the two beams, repeatedly sent and received, capture the entire movement of the system. Equally, if the surface does not move during the time separation of the beams then the time separation of the beams is unnecessarily short and can be extended. The Nyquist theorem can be used to calculate the time separation of the two beams required to fully resolve a surface moving harmonically between two positions at a given frequency. This principle, given a time separation between the two beams, can be used to calculate the bandwidth of the interferometer.

The description above covers the basic principle of interferometry. Lasers are used for interferometry because they produce very coherent beams of light. Normally the laser detection of ultrasound is done using an interferometer positioned perpendicular to the specimen surface which measures displacements perpendicular to the specimen surface. This is the same as longitudinal wave electro-mechanical devices when recording ultrasonic signals. This means that laser interferometers being used for the reception of ultrasound in this way have favourable directivity patterns.

5.3 Laser Ultrasonic Arrays

Laser ultrasonic arrays have been attempted since the popularisation of ultrasonic arrays. These attempts predominantly consisted of using either multiple lasers [61] or splitting the beam from a single laser into multiple beams [62]. These two methods each have disadvan-

tages. The former is costly and the latter reduces the power available for each element. In the latter case, each beam is delayed using beam paths of different lengths. This would either be in the form of large distances between mirrors [62] or long fibre optic optical delay lines [63]. The use of semi-permanent delay lines meant that systems were very bulky and not readily reconfigurable. Many of these historic attempts at arrays were therefore targetted towards creating laser ultrasonic counterparts for ultrasonic arrays which focussed ultrasound to a particular point using delays in generation [64, 65, 66]. Attempts were also made to shape individual laser beams in generation to focus at a particular point [67].

None of these methods would be suitable for collecting the full array response matrix now often collected for imaging. Currently, the only feasible method for collecting the full array response matrix using laser ultrasonic arrays is to translate the generation and detection beams. Focusing can then be applied in post-processing using the Total Focusing Method (TFM) [20]. This allows a single laser to be used for generation and another to be used for detection which keeps the power high for each array element and also reduces the cost of the system. This method has two disadvantages. Firstly, the translation of the lasers means that the data collection speed is reduced. Secondly, the imperfect repeatability of the translation stages can cause the positions of the elements to shift between each transmit-receive combination.

The laser ultrasonic array and the TFM were first combined by Stratoudaki et al. in 2016 [18]. Subsequent papers using the same technique were also published by the authors [68, 69]. Most recently, the technique was applied to additively manufactured components [70]. These works produced a number of interesting results.

Firstly, it should be noted that the generation of ultrasound in a metal sample using a laser to produce a thermoelastic source produces much lower amplitudes of ultrasonic displacement in the sample than conventional transducers. For this reason, A-Scans in the full array response matrix collected using laser ultrasonic arrays have a relatively low signal-to-random-noise ratio. This is seen in the high number of experimental averages required when collecting the full array response matrix. Stratoudaki et al., for example, used 500 experimental averages for each A-Scan in the full array response matrix [18]. This high number of experimental averages decreases the data collection speed significantly. For example, using the information provided in [18], the time required to collect the full array response matrix for a 128 element array using this method can be calculated to be over 3 hours. With the theoretically optimal setup suggested, data collection would take just under half an hour.

Secondly, Rayleigh waves appear in the TFM images as artefacts at the surface just under the array. This happens with laser ultrasonic arrays using thermoelastic generation because the directivity of the elements in generation is not favourable. Standard ultrasonic array elements have a slowly varying directivity function over a large angular range, with each element seeing a point reflector target with a similar amplitude. When the TFM image is formed, each element contributes a similar amount to pixels at the target location. Surface waves however only contribute where the time from the element pair to the pixel is equal to the time taken for the surface wave to travel between the element pairs. This single contribution is usually averaged out by the zero contribution from other element pairs. Laser ultrasonic arrays using thermoelastic generation on the other hand, due to their strongly directional directivity in generation, have only a few element pairs which contribute to pixels at the target location. The other element pairs reduce the final image amplitude through averaging out the target response with zero contributions. This then becomes of a similar order of magnitude as the single element pair contribution which contributes a higher amplitude surface wave response. Hence the surface wave artefact appears in the final image as it is of a similar amplitude to the target reflector.

Lastly, the strong lobes of the directivity in generation cause a few other peculiarities in the images. These are that imaging directly under the array is difficult and so the back wall of the sample is not seen.

Some of these effects were compensated for by applying apertures to the TFM algorithm and through a division of the TFM image by the sensitivity image. These are described below in more detail.

5.3.1 Sensitivity Images and Weighting Image Contributions

Details of the forward model and the TFM imaging algorithm were given in Section 2.2.1 and Section 2.2.2, but are repeated here for readability.

The frequency domain full array response matrix, $\tilde{h}_{tr}(\omega)$, of an array to a point reflector is given by:

$$\tilde{h}_{tr}(\omega) = \Psi_0(\omega)\, B_t(\mathbf{b_t})\, B_r(\mathbf{b_r})\, \Gamma_t(\omega, \mathbf{b_t})\, \Gamma_r(\omega, \mathbf{b_r}) \exp\left(-i\omega \frac{|\mathbf{b_t}| + |\mathbf{b_r}|}{v}\right), \tag{5.4}$$

where ω is the angular frequency, Ψ_0 is the spectrum of the input pulse, B_j is the beam spread, Γ_j is the array element directivity, $\mathbf{b_j}$ is the vector from the point reflector to the array element and v is the wave velocity. The index j can be either t or r for transmission or reception respectively.

The TFM image, I, at image point, $\mathbf{p}$, is given by the equation:

$$I(\mathbf{p}) = \sum_{t,r} \Lambda_t \Lambda_r h_{tr} \left(\frac{|\mathbf{c_t}| + |\mathbf{c_r}|}{v} \right), \tag{5.5}$$

where Λ_j is a weighting function for either transmission or reception, h_{tr} is the time domain full array response matrix and $\mathbf{c_j}$ is the vector from the image point to the array element. Finally, the sensitivity image of the TFM algorithm to a point reflector is given by:

$$S(\mathbf{p}) = \left| \sum_{t,r} \Lambda_t \, \Lambda_r \, B_t(\mathbf{c_t}) \, B_r(\mathbf{c_r}) \, \Gamma_t(\mathbf{c_t}) \, \Gamma_r(\mathbf{c_r}) \right|. \tag{5.6}$$

The sensitivity image gives an indication of the expected maximum amplitude of an image at the image point if the target were located at the image point, for all image points.

In [18] the strong lobe directivity functions of the generating elements in the laser ultrasonic array caused the amplitudes of the reflectors to vary more than for standard ultrasonic arrays. To counteract this effect, the final image was divided by the sensitivity image, effectively normalising the response of each reflector. In [68, 69, 70] the additional step of weighting the contributions of each transmit-receive combination was added. The combinations were weighted according to the directivity of the elements and the beam spread of a point reflector. This is given by the equation:

$$\Lambda_j = \Gamma_j(\omega, \mathbf{c_j}) \, B_j(\mathbf{c_j}). \tag{5.7}$$

This helps to weight contributions which should produce strong reflections from the targets more strongly.

Chapter 6

Modelling Diffuse Field Hybrid Piezo-Laser Ultrasonic Arrays

6.1 Introduction

The directivity pattern of ultrasound generated using lasers in the thermoelastic regime and the low data collection speed are currently two big problems with laser ultrasonic arrays for the inspection of metals. The directivity pattern, not being broad and smooth in shape, means that very few elements in an array receive a reflection from a point reflector target. This causes the Rayleigh waves to be higher in amplitude after the Total Focusing Method (TFM) algorithm is applied than the signals from the target, leading to large Rayleigh wave artefacts in the images. This chapter uses modelling to demonstrate a data collection method which deals with both of these issues. Diffuse fields can be used to eradicate the unfavourable directivity of laser ultrasonic generation by using them to reconstruct the signal between pairs of laser ultrasonic detector receive elements. This removes any directivity associated with the generation laser and effectively creates an array of elements which have the directivity pattern of a laser ultrasonic detector in both transmission and reception. Laser ultrasonic receive elements have a much more favourable directivity, similar to that of electromechanical transducers. One of the merits of this method is that, in principle, any type of source can be used. The only requirement is that the source excites ultrasound at frequencies of interest in the sample. Diffuse field ultrasonic methods have never been applied to laser ultrasonic arrays before. If the directivity pattern of laser ultrasonic arrays could be made more favourable, and the data collection speeds increased, then the use of laser ultrasonic arrays could become more prevalent. As a test of the principle, and for a greater chance of success before progressing the method, a contact transducer will be used in generation and an array of laser ultrasonic interferometer

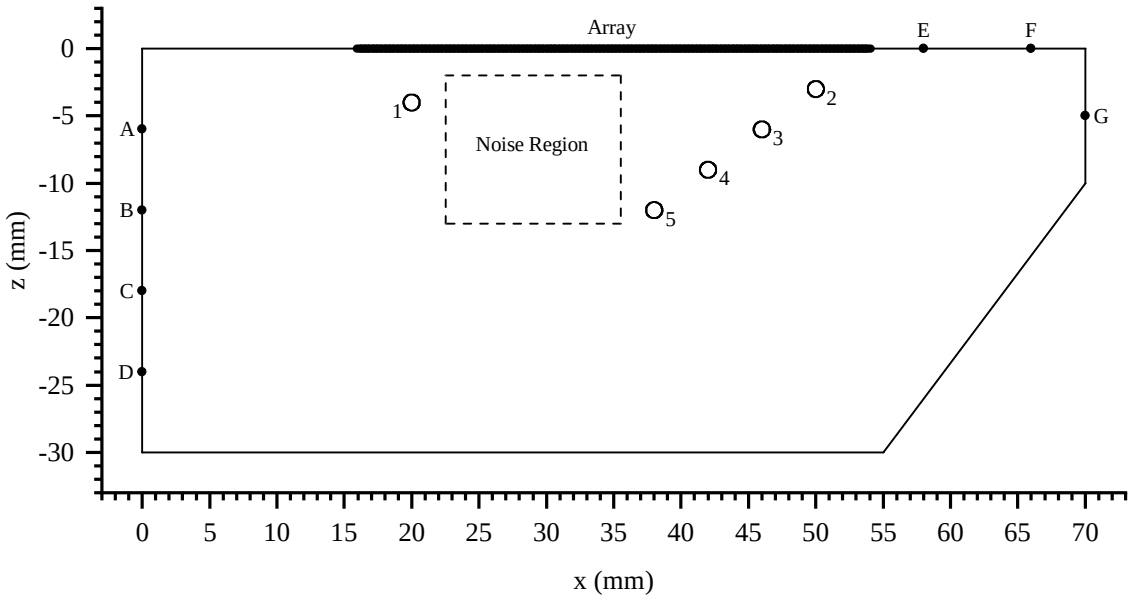

Figure 6.1: Schematic of the sample modelled using FE. The target SDHs are labelled numerically. The different positions used for excitation are labelled alphabetically. These represent different positions of a transmitting transducer. The spatial extent of the linear array is shown as a thick line on the top of the outline of the sample. The region used to evaluate the reconstruction noise in the images is shown as a box with a dashed boundary.

elements in reception.

6.2 Method

6.2.1 Sample

A rectangular sample was designed which was suitable for imaging using a linear array. A wedge shaped cut, not at $45°$, was included in the design in order to promote the rapid formation of a diffuse field within the sample. Five $1.2\,\mathrm{mm}$ diameter Side Drilled Holes (SDHs), located at different depths and positions within the sample were also included as targets. A schematic of the sample is shown in Figure 6.1. Aluminium was chosen for the sample material because it was consistent with the previous literature on laser ultrasonic array experiments [18, 68, 69] and because it has a very low grain noise which makes the defects easier to image in this proof-of-concept study.

6.2.2 Modelling

A suitable model was required so that an understanding of diffuse fields and the reconstruction process could be gained. A time-domain FE model was chosen because the frequency domain linear-time-invariant model used for previous work was not suitable for the necessary large number of reflections over long periods of time required to generate diffuse field data. The FE package used was called Pogo and was chosen because of the speed of its solver [71]. Triangle, a 2-Dimensional (2D) Delaunay mesh generator, was used to generate the triangular mesh of the sample [72]. Triangle was executed using a minimum element angle of 20° and a maximum area constraint. The maximum area constraint was calculated based on the desired number of elements per shear wavelength, E_s.

The material properties used were a Young's modulus of $70\,\mathrm{GPa}$, a density of $2700\,\mathrm{kg\,m^{-3}}$ and a Poisson's ratio of 0.34. This yielded a longitudinal wave velocity of $6317\,\mathrm{m\,s^{-1}}$, a shear wave velocity of $3110\,\mathrm{m\,s^{-1}}$ and a Rayleigh wave velocity of approximately $2900\,\mathrm{m\,s^{-1}}$ [73]. For simplicity, no attenuation was used in the model and there was no medium surrounding the sample. The target SDHs were modelled as material free regions.

6.2.2.1 Transmission

The generation of ultrasound in the model was through a force being applied to nodes within a $6\,\mathrm{mm}$ aperture located on the outer surface of the sample. The nodes were forced using a five-cycle Hann-weighted sine wave, with a centre frequency of $5\,\mathrm{MHz}$. Multiple nodes were within the aperture. For this reason, the total force amplitude of the input force was divided by the number of nodes within the aperture. The force was applied perpendicular to the surface for longitudinal wave generation and transversely for shear wave generation. This generation method represented a single element transducer. A schematic of the force being applied perpendicular to the surface and the input signal used is shown in Figure 6.2.

6.2.2.2 Reception

Detection of ultrasound in the model was through the recording of the displacements of the nodes within a $50\,\mu\mathrm{m}$ aperture located on the outer surface of the sample. The displacements perpendicular to the surface were recorded. Again, when multiple nodes were within the aperture, the displacements recorded were averaged across the aperture. An array of 128 of these detection apertures, separated by a pitch of $300\,\mu\mathrm{m}$, were used in the model. The location of the array is shown in Figure 6.1. A schematic of the displacements recorded perpendicular

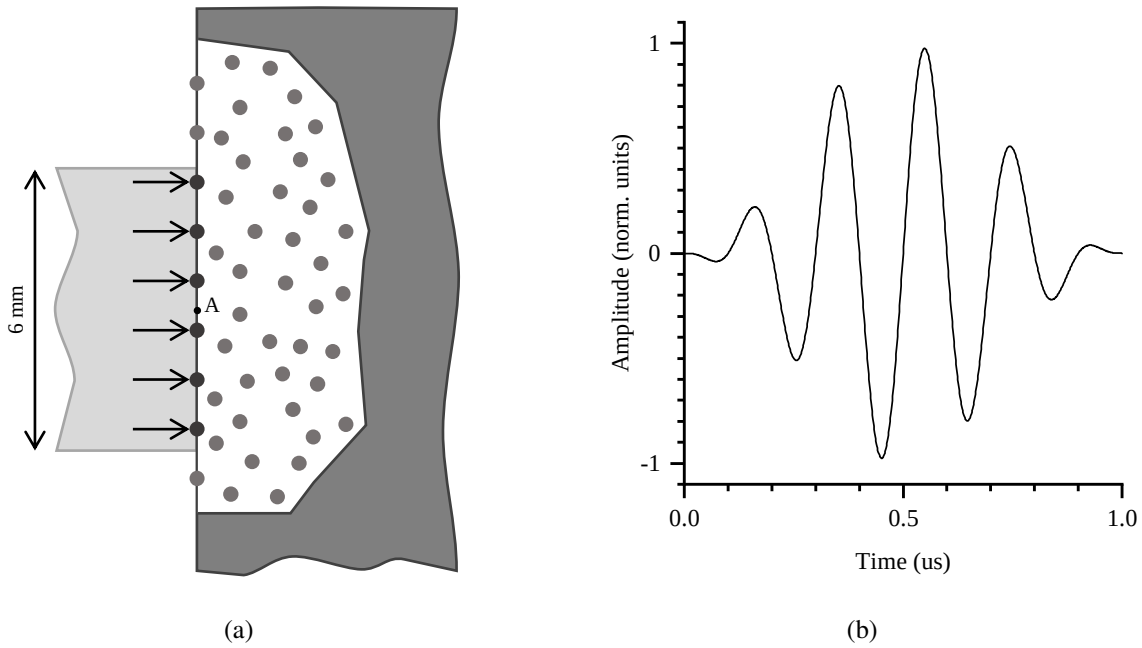

(a) (b)

Figure 6.2: Schematic of the method used for the transmission of ultrasound in the FE model. Ultrasound was generated by the application of a force to the nodes at the surface within an aperture. The aperture used represented a single element transducer. In the example shown in (a), longitudinal waves were generated by applying a force perpendicular to the surface. The nodes were forced using the input signal shown in (b).

to the surface, and the nodes used for each array element, is shown in Figure 6.3. The detection apertures modelled represented an array of laser interferometers. The aperture width was nominally chosen to represent the beam width of a generic interferometer. The pitch between the apertures was chosen so that it was much less than half the wavelength of the longitudinal waves at the generated frequency [17]. The frequency profile of the transfer function of the laser interferometer was not accounted for in the model.

6.2.2.3 Data Collection

Diffuse Field For the collection of diffuse field data, forcing was applied at location A in Figure 6.1. The length of the A-Scans recorded was $1\,\mathrm{ms}$. This was a compromise between field diffusivity and computation time. A sampling frequency of $50\,\mathrm{MHz}$ was used. Forcing was applied at the other locations in Figure 6.1 when investigating the effect of averaging the reconstruction over multiple forcing locations. The displacements of the nodes within the aperture used for excitation were also recorded to simulate the pulse-echo response at the forcing location.

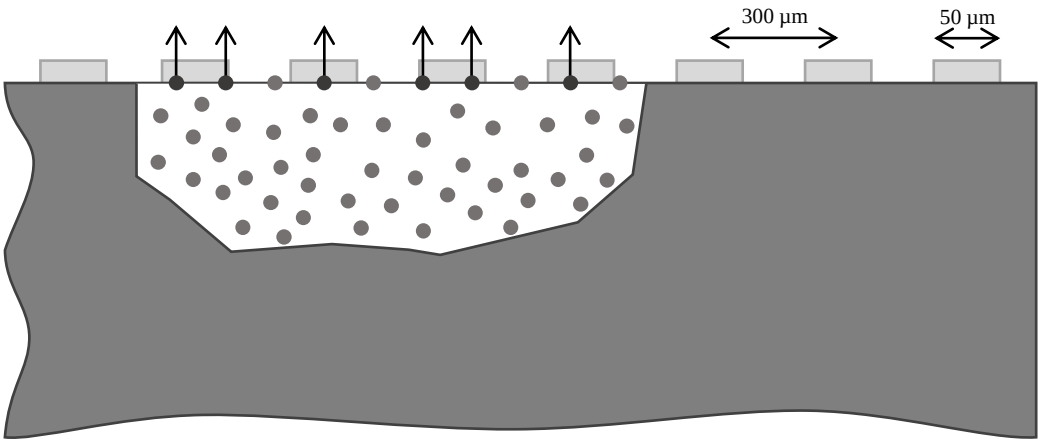

Figure 6.3: Schematic showing the nodes within each array element aperture and the displacement perpendicular to the surface recorded for longitudinal wave detection. Where multiple nodes were within an element aperture, the displacements measured were averaged.

Full Array Response Matrix For the collection of the full array response matrix, the nodes within a detection aperture were excited and the displacements of the nodes within each aperture were recorded. Each aperture was excited sequentially in order to build up the full array response matrix. The same excitation and recording processes as those described above were used.

6.2.2.4 Mesh Convergence

A mesh convergence study was carried out in order to determine the mesh density required. Ultrasound was generated at location A. The arrival time and amplitude of the reflection from the first SDH in the pulse-echo response was recorded as a function of E_s. This was done by finding the maximum of the absolute of the Hilbert envelope between $4\,\mu s$ and $8\,\mu s$. Both the amplitude and arrival time were converted into normalised dimensionless metrics. The arrival time convergence metric, C_t, was defined as:

$$C_t = \frac{t - t_c}{t_c}, \tag{6.1}$$

where t is the arrival time of the reflection and t_c is the arrival time of the reflection for the largest value of E_s tested. A similar metric for the amplitude of the reflection, C_a, was defined as:

$$C_a = \frac{a - a_c}{a_c}, \tag{6.2}$$

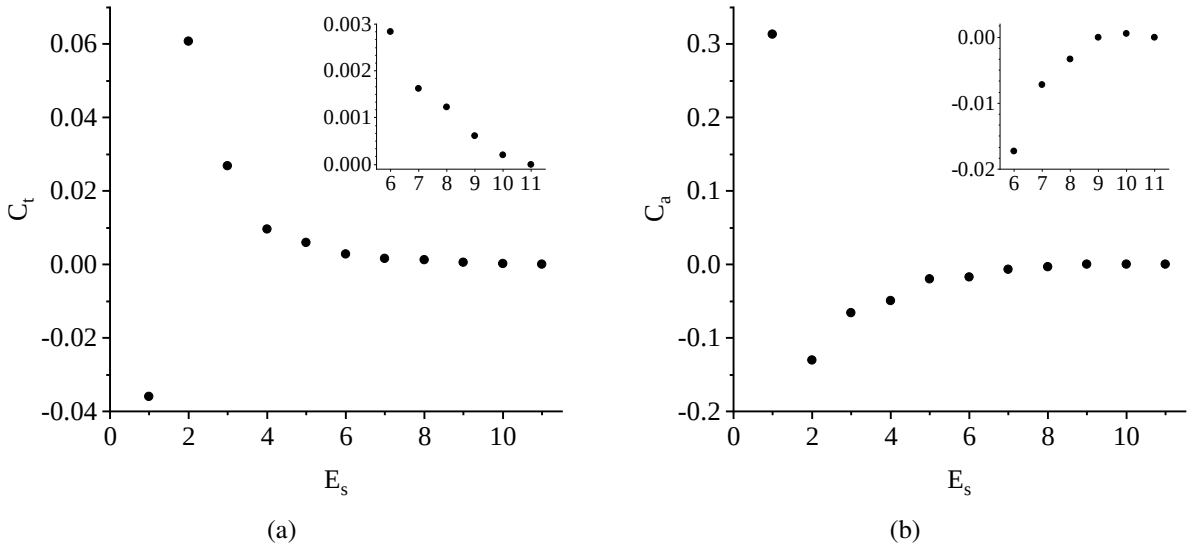

Figure 6.4: Mesh convergence results for (a) the arrival time and (b) the amplitude of the reflection from the first SDH when the excitation was applied at location A. E_s is the number of elements per shear wave length. C_t and C_a are the arrival time and amplitude convergence metrics respectively.

where a is the amplitude of the reflection and a_c is the amplitude of the reflection for the largest value of E_s tested. These metrics as a function of E_s are shown in Figure 6.4. C_t converges much quicker than C_a by approximately an order of magnitude. Both metrics had converged to within $1\,\%$ after 7 elements per shear wavelength. A conservative value of 10 elements per shear wavelength was chosen for the modelling in this chapter.

6.2.3 Reconstruction Process

The process used to reconstruct early time full array response matrix data is given in Section 5.1. The equations used are repeated here for readability.

The time domain diffuse field data collected, $g_{tr}(\tau)$, was windowed and a Fourier transform performed in order to calculate the frequency domain response, $\tilde{g}_{tr}(\omega)$. This was done using the equation:

$$\tilde{g}_{tr}(\omega) = \int_{\tau_1}^{\tau_2} g_{tr}(\tau)\, e^{-i\omega\tau}\, \mathrm{d}\tau, \tag{6.3}$$

where t and r represent the indices of the transmitter and receivers respectively, ω is the angular frequency, τ is time, τ_1 and τ_2 are the start and ends of the reconstruction window respectively and $i = \sqrt{-1}$. An approximation to the frequency domain early time full array

response matrix of the receive elements, $\tilde{h}_{r_1 r_2}(\omega)$ is then given by the equation:

$$\tilde{h}_{r_1 r_2}(\omega) \approx i\omega \; \tilde{g}_{tr_1}(\omega) \; \tilde{g}^*_{tr_2}(\omega), \tag{6.4}$$

where $*$ denotes the complex conjugate. The division by the auto-correlation of the pulse-echo response at the forcing location was omitted because this would not be possible when using a laser ultrasonic source for ultrasonic excitation. The inverse Fourier transform is then applied to convert the full array response matrix from the frequency domain to the time domain for imaging. This process is repeated for every combination of receive elements. Where multiple transmit elements are used, this process was carried out for each transmit element separately and the final result averaged.

6.2.4 Imaging

All A-Scans from full array response matrices used for imaging were first filtered with a Gaussian filter. The Gaussian filter had a centre frequency of $5\,\mathrm{MHz}$ and a standard deviation of $2.5\,\mathrm{MHz}$. The TFM was used to image all the data in this chapter. In keeping with the previous literature on laser ultrasonic arrays, weighting was applied to each transmit-receive combination. The weighting applied was proportional to the theoretical directivity of the array elements and the beam spread of a point reflector in accordance with Equation 5.7.

6.2.5 Performance Evaluation

Although the model results contain no random noise, the imperfection of the reconstruction process causes noise to be seen in the final image. The reconstruction noise level in the images was calculated by taking the Root Mean Square (RMS) of the amplitudes of the pixels inside a region in the middle of the sample. The noise region was defined as $(22.5\,\mathrm{mm} \leq x \leq 35.5\,\mathrm{mm})$ and $(-13\,\mathrm{mm} \leq z \leq -2\,\mathrm{mm})$ and is shown schematically in Figure 6.1. This was chosen so that it covered a similar depth range to the SDHs while not including any of the SDHs within the region itself. The maximum image amplitude in the region of each SDH was used to calculate the Signal-to-Noise Ratio (SNR) relative to the RMS noise level within the noise region.

6.3 Results

Samples of the pulse-echo A-Scan from the forcing aperture being located at location A, at early and late times, are shown in Figure 6.5. The absolute of the displacement field at various

times during the model are shown in Figure 6.6. Example longitudinal wave mode images, reconstructed from the diffuse field data when the excitation aperture was located at location A, are shown in Figure 6.7. The direction of forcing was changed between being perpendicular and parallel to the surface for Figure 6.7a and Figure 6.7b respectively. The longitudinal wave mode was used for imaging in both cases. The image obtained using the directly obtained full array response matrix is also shown in Figure 6.8 for comparison. The mean SNRs of the reconstructed images as a function of the reconstruction window length, window location and the number of forcing locations averaged across, are shown in Figure 6.9, Figure 6.10 and Figure 6.11 respectively. The window length is shown for both the full window being used for the reconstruction, and the window being broken up into sub-windows before the result is averaged. Finally, two A-Scans from the diffuse field data, the pitch-catch A-Scans reconstructed from these two diffuse field A-Scans, and their equivalent directly obtained pitch-catch A-Scan are shown in Figure 6.12. The reconstructed A-Scans are shown when averaged over 1 and 7 forcing locations respectively.

6.4 Discussion

It can be seen from the results in Figure 6.7 that it was possible to reconstruct an approximation to the full array response matrix from a single excitation location using diffuse field reconstruction techniques. The images show no Rayleigh wave artefacts, which are usually common to laser ultrasonic images. This is because the transfer function of each element in the receiving array, when collecting the diffuse field data, becomes the transfer function of the elements in both transmit and receive after reconstruction. This means that the imaging array contains elements with favourable circular directivity patterns so that all the elements see all of the targets.

The similarities between Figure 6.7a and Figure 6.7b demonstrate qualitatively that the method of excitation for this data collection methodology does not significantly influence the results. As the shear wave has a speed of approximately half that of the longitudinal wave, it should have undergone fewer reflections inside the sample within the window used for the reconstruction. The similarities between the two images indicate that the levels of scattering and mode conversion at early times is sufficiently high to mean that this effect does not reduce the reconstruction quality. However this may well be why the reflections from the SDHs decay quicker with depth in the shear wave generated image and why this image has a more broken back wall reflection. It should be noted that there is no attenuation in the FE model,

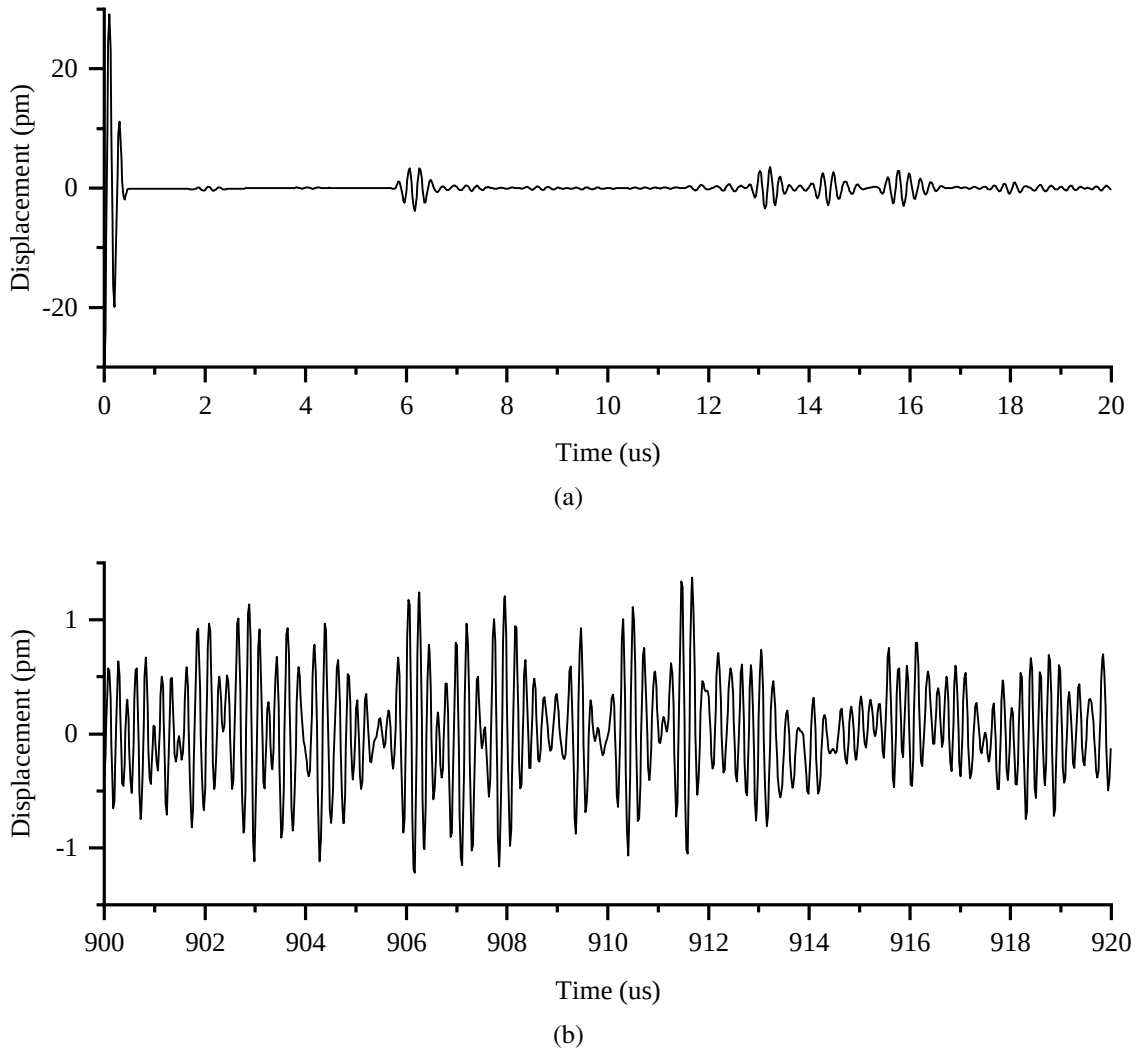

Figure 6.5: Samples of the pulse-echo response when the excitation was applied at location A. The coherent and diffuse nature of the field at early and late times can be seen in (a) and (b) respectively.

which would affect longitudinal and shear waves by different amounts. Therefore, experimentally, this indifference to longitudinal or shear generation over the same reconstruction window would not be expected to be as strong.

It is interesting to compare the reconstructed images in Figure 6.7 with the directly obtained full array response matrix image in Figure 6.8. Obviously there is no noise in the noise region of the direct image. The back wall is smoother. This is to be expected as the reconstruction is only an approximation [47]. It can also be seen that the responses from the SDHs, and especially the back wall, are narrower in the direct image. This indicates a higher bandwidth in the direct case. Any loss in bandwidth must be due to the reconstruction process and may be caused by the need to window the data before applying the reconstruction, the reconstruction

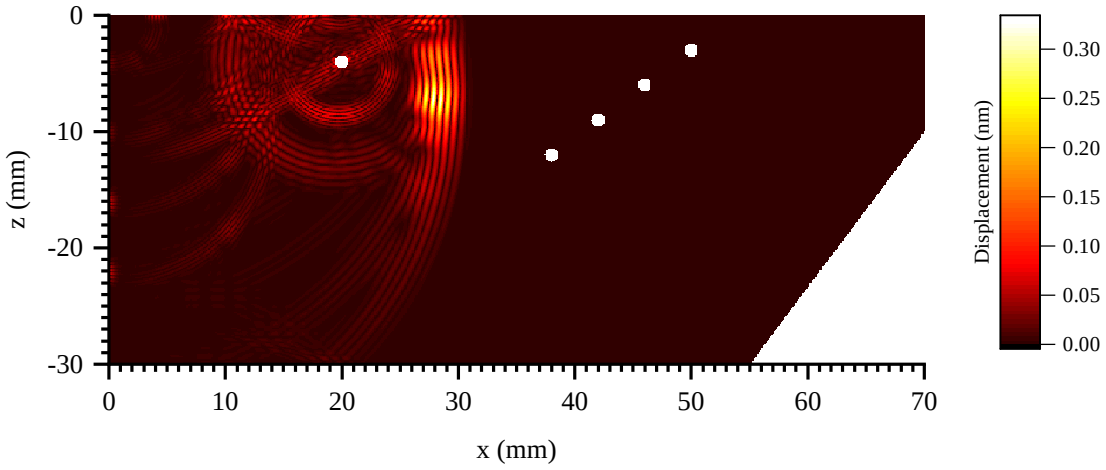

(a) $t = 5.00\,\mu s$ (3 s.f.)

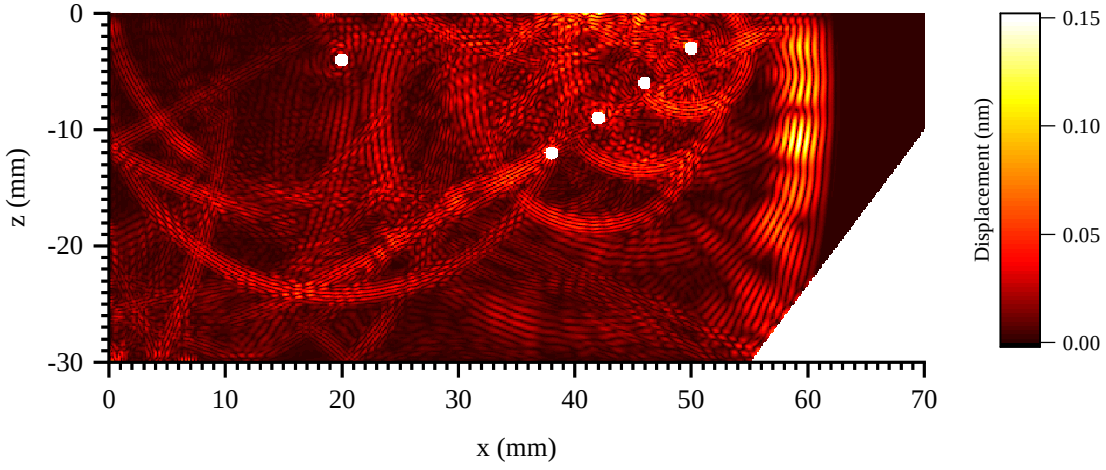

(b) $t = 10.0\,\mu s$ (3 s.f.)

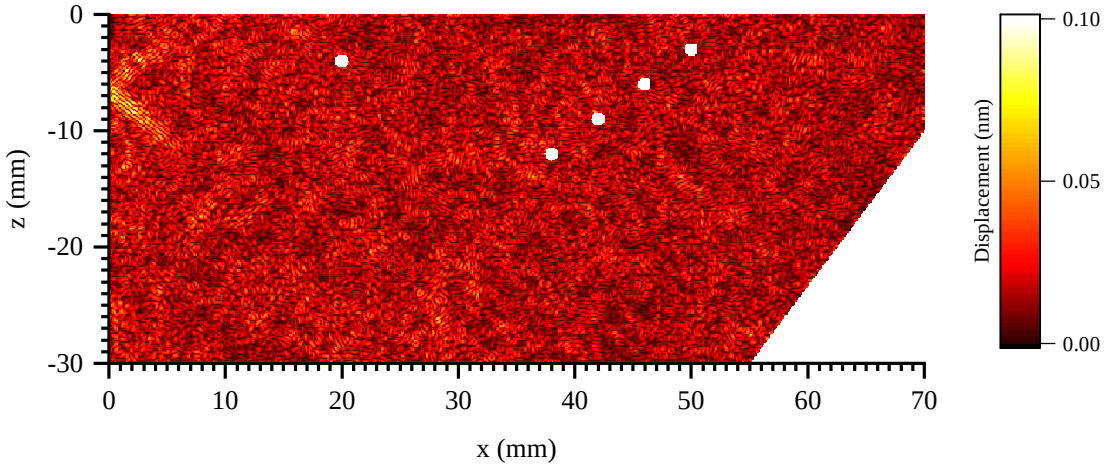

(c) $t = 45.0\,\mu s$ (3 s.f.)

Figure 6.6: Absolute displacement field images from the FE model at different times after initial excitation perpendicular to the surface at location A. The maximum of the colour scale for each image is the maximum absolute displacement in that image.

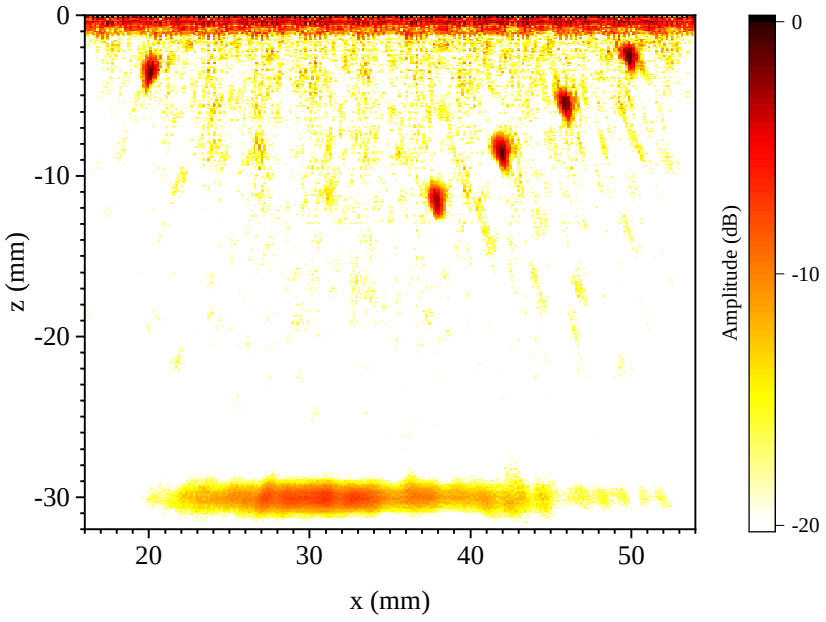

(a)

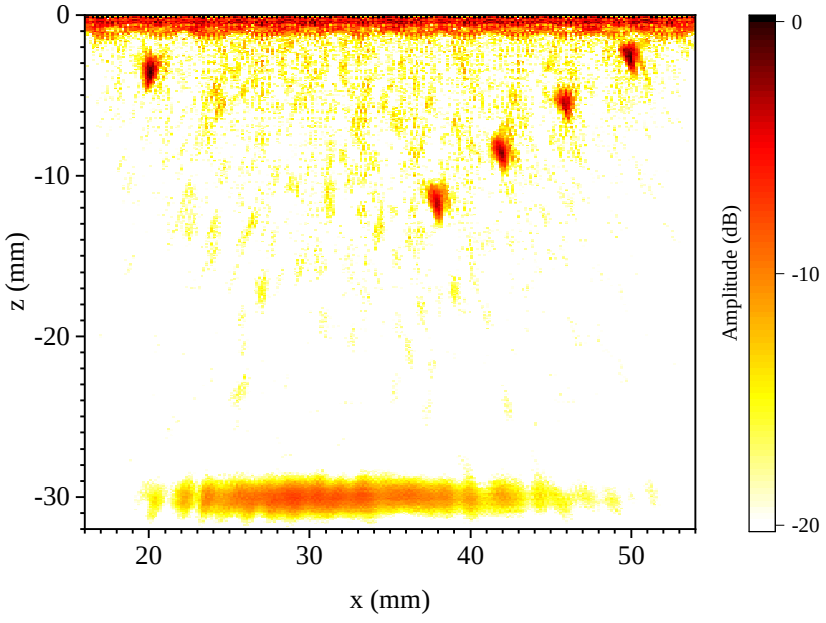

(b)

Figure 6.7: Longitudinal wave mode TFM images from reconstructed data for the array when the nodes at location A were excited (a) perpendicular and (b) parallel to the surface of the specimen. The reconstruction window used was from $0\,\mu s$ to $500\,\mu s$ in $100\,\mu s$ sub-windows. The decibel scale has been normalised to the maximum value in the image. Weighting for both the element directivity and the beam spread of a point reflector was incorporated into the imaging algorithm.

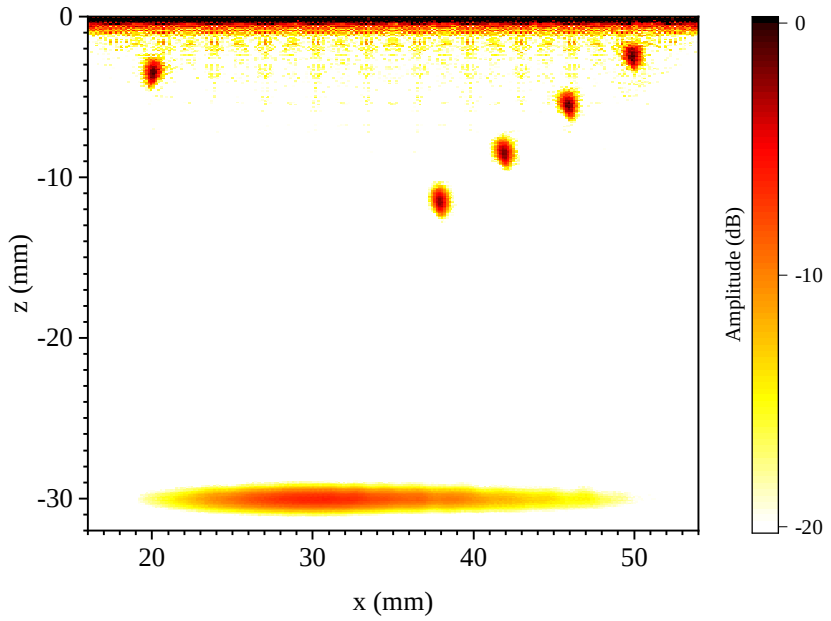

Figure 6.8: A longitudinal wave mode TFM image from the direct full array response matrix for the array. The decibel scale has been normalised to the maximum value in the image. Weighting for both the element directivity and the beam spread of a point reflector was incorporated into the imaging algorithm.

process effectively squaring the spectra, and then applying a filter after reconstruction before imaging.

Figure 6.9 and Figure 6.10 both show that the reconstruction noise decreases with window length. This is in agreement with the theory in the absence of random noise and attenuation. The increase in SNR is greatest when increasing the window length from $100\,\mu s$ to $400\,\mu s$, with the SNR not improving as much as the window length is increased after this. The drop in SNR at $300\,\mu s$ in Figure 6.9 is not unexpected when the same points are identified in Figure 6.10. The corresponding points are the first points in Figure 6.10 for each window length. It can be seen in Figure 6.10 that the location of any window affects the SNR of the reconstruction greatly. However, the general trend is shown clearly in Figure 6.10, that increasing the window length, on average, increases the SNR of the reconstructed image.

Using the full window for the reconstruction always produced a higher SNR than breaking the window up into sub-windows and averaging the reconstruction result for each sub-window. This is expected to be because the use of a longer window produces a frequency spectrum with a higher frequency resolution, allowing finer features to be characterised.

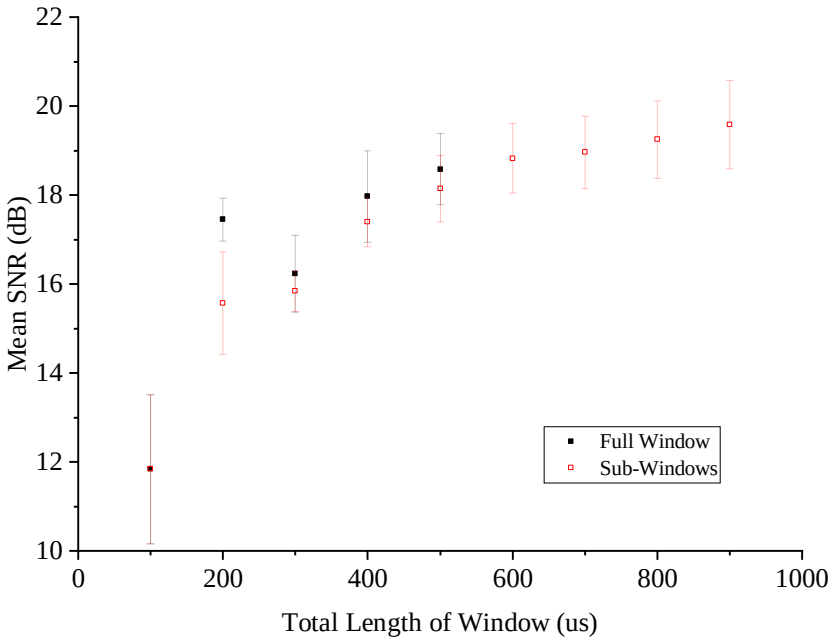

Figure 6.9: The mean SNR of the SDHs in the image for different reconstruction window lengths. The error bar shows the standard deviation of the SNR of the SDHs in the image. Two data sets are potted. The first uses the full window length for the reconstruction. The second splits the window up into sub-windows, calculates the reconstruction, and then averages the results from all of the sub-windows. All windows began at $0\,\mu s$. The full window reconstruction is highly computationally expensive and so is not performed beyond a window length of $500\,\mu s$.

Figure 6.10 shows that the SNR is very dependant on the location of the reconstruction window in time. There is no decay in SNR with later and later time because of the lack of random noise and attenuation. However, the SNR does seem to fluctuate somewhat randomly as the window shifts in time. The cause of these fluctuations is not known. However, given that the reconstruction relies on cross-correlations of multiple internal reflections, it is not altogether surprising. It is clear from Figure 6.10 that increasing the window length not only increases the mean SNR, but also helps to narrow the distribution of SNRs recorded as the reconstruction window moves through the A-Scan. This dependence might not be present in a real system, where random noise and attenuation may limit the positioning of the reconstruction window to early times.

Figure 6.11 shows that averaging the reconstruction result over a number of different excitation locations improves the SNR in agreement with the theory. Again, the greatest increase in SNR is when moving from 1 excitation location to 2 excitation locations, with subsequent

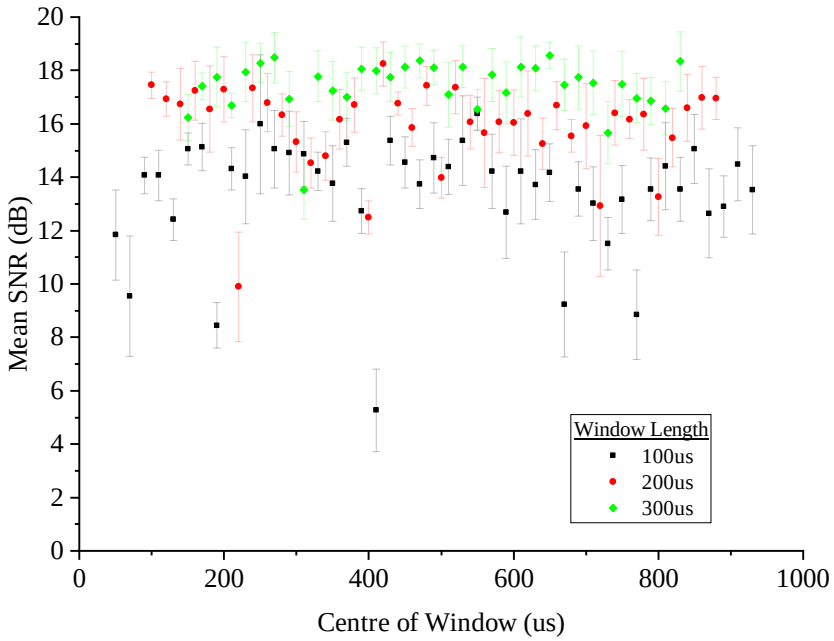

Figure 6.10: The mean SNR of the SDHs in the image for different reconstruction window centres. The error bar shows the standard deviation of the SNR of the SDHs in the image. Three different data sets are plotted corresponding to different window lengths.

increases producing a proportionally lower increase in SNR. It is clear when comparing the reconstructed A-Scans in Figure 6.12c and Figure 6.12d with the direct pitch-catch A-Scan in Figure 6.12e that the reconstruction noise obscures the small amplitude reflections from the SDHs. Only the initial Rayleigh wave is visible above the reconstruction noise in both reconstructed A-scans. The reflection of the Rayleigh wave from a corner of the sample only becomes visible when averaging across all 7 excitation locations.

6.5 Conclusion

A hybrid piezo-laser ultrasonic array which utilised diffuse fields was demonstrated, through modelling, to improve the imaging of laser ultrasonic arrays. The SNR of TFM images formed from data using this method were improved by increasing the length of the window used for the reconstruction and through averaging the reconstruction result over a number of excitation locations. The quality of the reconstruction was shown to be very dependant on the window location, but no clear pattern to this was found. Increasing the window length also helped to reduce this dependence.

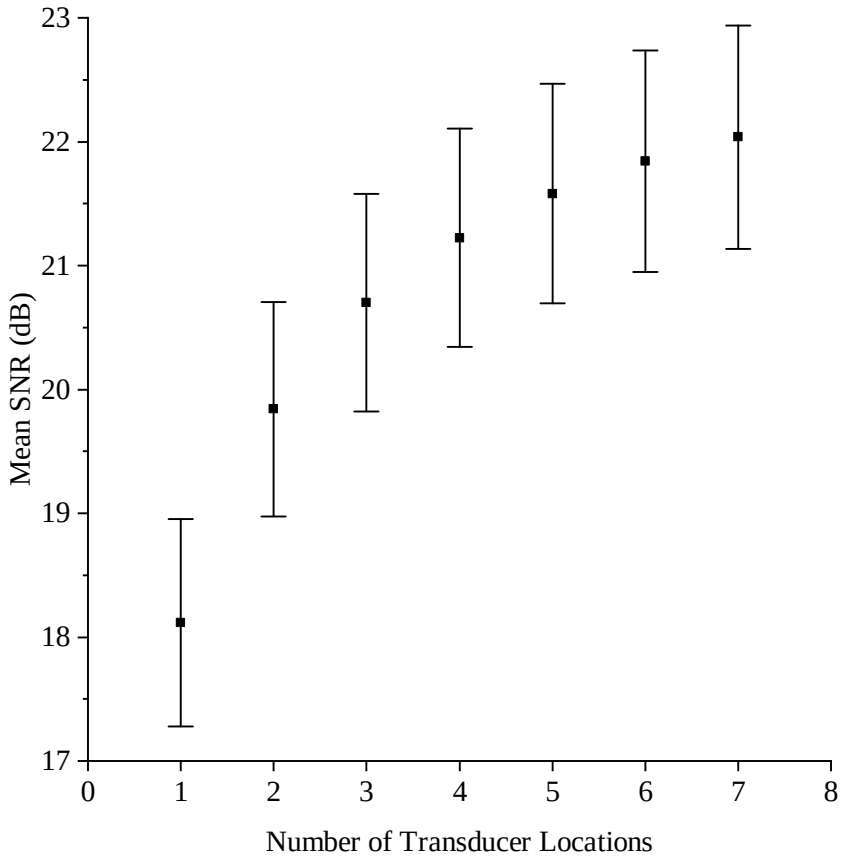

Figure 6.11: The mean SNR of the SDHs in the image when averaging over different numbers of excitation locations. The reconstruction window used was from $0\,\mu s$ to $500\,\mu s$ in $100\,\mu s$ sub-windows. The error bar shows the standard deviation of the SNR of the SDHs in the image.

These results have given sufficient confidence that the data collection method works theoretically. An experiment can be performed to test the imaging of hybrid piezo-laser ultrasonic arrays on metals.

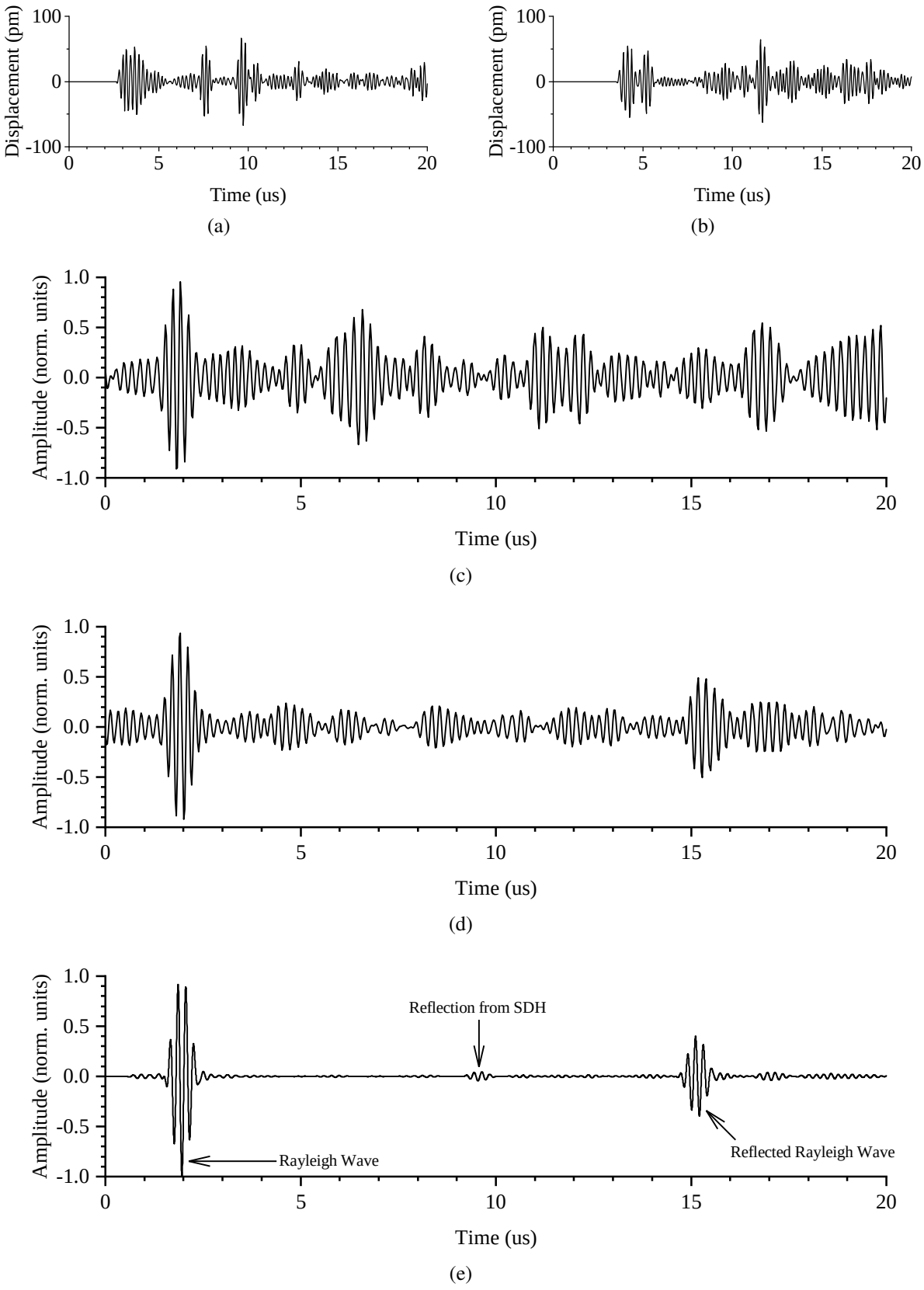

Figure 6.12: A-Scans from elements (a) 12 and (b) 31 of the diffuse field data. The reconstructed pitch-catch A-Scan between these two elements is shown in (c) and (d) when averaging across 1 and 7 forcing locations respectively. The direct pitch-catch A-Scan between the elements is shown in (e). Only the first 20 μs of each A-Scan are shown.

Chapter 7

Experimental Testing of Diffuse Field Hybrid Piezo-Laser Ultrasonic Arrays

7.1 Introduction

The reconstruction of diffuse field data into the full array response matrix using a single transmitter and an array of receivers has been shown through modelling to be successful. If this technique can be applied experimentally to a transducer being used to generate ultrasound and a laser ultrasonic array being used to detect, then the possibility of a fully non-contact laser ultrasonic diffuse field array is increased. This would enable the data collection times for laser ultrasonic arrays to be decreased and would produce images with properties more similar to conventional ultrasonic arrays. This chapter shows the results of an experimental trial using a sample with the same geometric shape as that used in the modelling. Diffuse field ultrasonic methods have never been applied experimentally to laser ultrasonic arrays before. Images are formed, using the Total Focusing Method (TFM), from the reconstructed full array response matrix and the optimal reconstruction window properties are discussed.

7.2 Method

7.2.1 Sample

An aluminium sample was machined which had the same profile as the 2-Dimensional (2D) sample described in Section 6.2.1 with a thickness of $20\,\mathrm{mm}$. The sample surface had a machined finish, but was not optically polished. The sample was clamped to a support structure using clamps with rubber feet. The support structure was used to position the sample surface

at the centre of rotation of the goniometer for better alignment. The wave velocities in the sample were measured to be approximately $6450\,\mathrm{m\,s^{-1}}$ (3 s.f), $3130\,\mathrm{m\,s^{-1}}$ (3 s.f) and $2880\,\mathrm{m\,s^{-1}}$ (3 s.f.) for longitudinal, shear and Rayleigh waves respectively. These values were calculated using imaging features such as the back wall and the target Side Drilled Holes (SDHs).

7.2.2 Transmission

A $6\,\mathrm{mm}$ diameter single element transducer (V310-SM, Olympus) was placed at location A [Figure 6.1] on the sample. The transducer was crudely attached to the sample using elastic bands wrapped around the transducer casing and the sample. Couplant was used between the transducer and the sample to increase the amount of energy transmitted into the sample. A pulser-receiver (5072PR, Panametrics) was used to excite the transducer and provide the trigger signal for the two combined Analog-to-Digital Converters (ADCs) (HS4-50 and HS5-530XM, TiePie). The pulser-receiver was used to control both the input energy to the transducer and the pulse repetition frequency, which were set to $104\,\mu\mathrm{J}$ [74] and $200\,\mathrm{Hz}$ respectively.

7.2.3 Reception

An interferometer (Double Differential Fibre Optic Sagnac, LuxSonics) [75, 76] was used to receive ultrasound at the 128 array element positions on the top face of the sample. The interferometer position on the sample surface was physically changed by translating the interferometer head using an electronic translation stage (X-LSM200B, Zaber). The array element positions had a nominal pitch of $0.3\,\mathrm{mm}$. The beam from the interferometer was aligned perpendicular to the sample surface. The interferometer power was controlled by changing the current going through the superluminescent diode. This was set to $250\,\mathrm{mA}$, which corresponded to an average power of $6\,\mathrm{mW}$. The raw ultrasonic time domain signal from the interferometer was first passed through the reception channel of the ultrasonic pulser-receiver before being recorded using the ADC (HS5-530XM). The pulser-receiver filtered the signal with both high-pass and low-pass filters which had cut-off frequencies of $1\,\mathrm{MHz}$ and $10\,\mathrm{MHz}$ respectively. Logarithmic gain could also be applied in order to use the digitisation range of the ADC efficiently, however this was not required. Each signal was repetition averaged 16 times before being stored. Each A-Scan in the diffuse field data had a length of $1.5\,\mathrm{ms}$. A sampling frequency of $100\,\mathrm{MHz}$ was used.

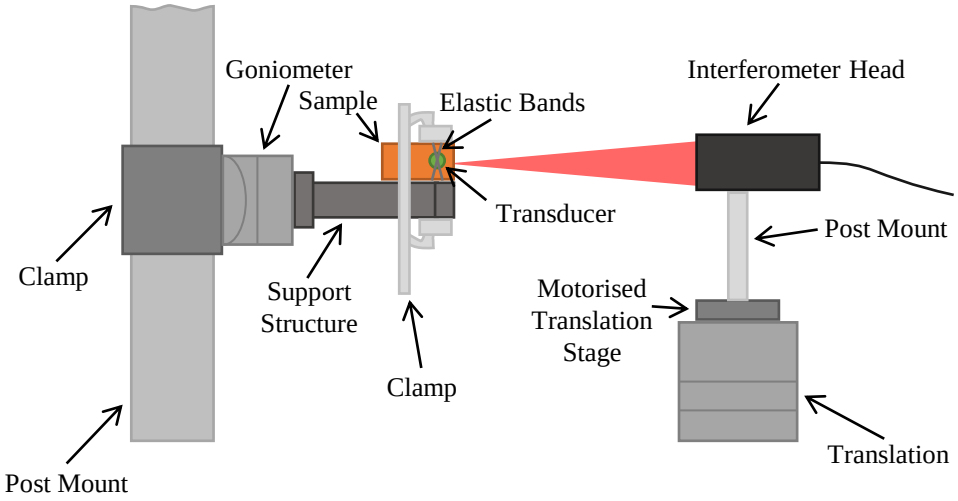

Figure 7.1: Schematic of the experimental setup used.

The transducer used for transmission was also used for reception in order to obtain the pulse-echo response. The same filtering, number of averages and A-Scan length were used when collecting the pulse-echo response. The signal was amplified by $19\,\mathrm{dB}$ before digitisation.

A schematic of the experimental setup is shown in Figure 7.1.

The low frequency output of the positive monitor channel was also recorded using the ADC (HS4-50). The amplitude of the monitor channel signal was proportional to the amount of light which was returned to the interferometer from the sample surface. As the interferometer is not calibrated, the maximum amplitude of the A-Scan signals recorded using the interferometer are similarly proportional to the light returned to the interferometer from the sample surface. The amount of light returned to the detector was not uniform across the sample surface. Figure 7.2 shows how the amplitude of the monitor channel signal varies with position around element number 100 in the array. A simple search algorithm was used to find locations of good reflectance close to each nominal element location. This was done with the aim of reducing the variation in the amplitudes of the signals in the diffuse field data.

The monitor channel voltage was recorded as the interferometer was scanned $75\,\mu\mathrm{m}$ around each nominal element centre in $2\,\mu\mathrm{m}$ (0 d.p.) increments. The peak response location from the first search was used as the centre of a second $9\,\mu\mathrm{m}$ long search using a finer increment of $1\,\mu\mathrm{m}$. If during the second search the response was greater than the first search peak response,

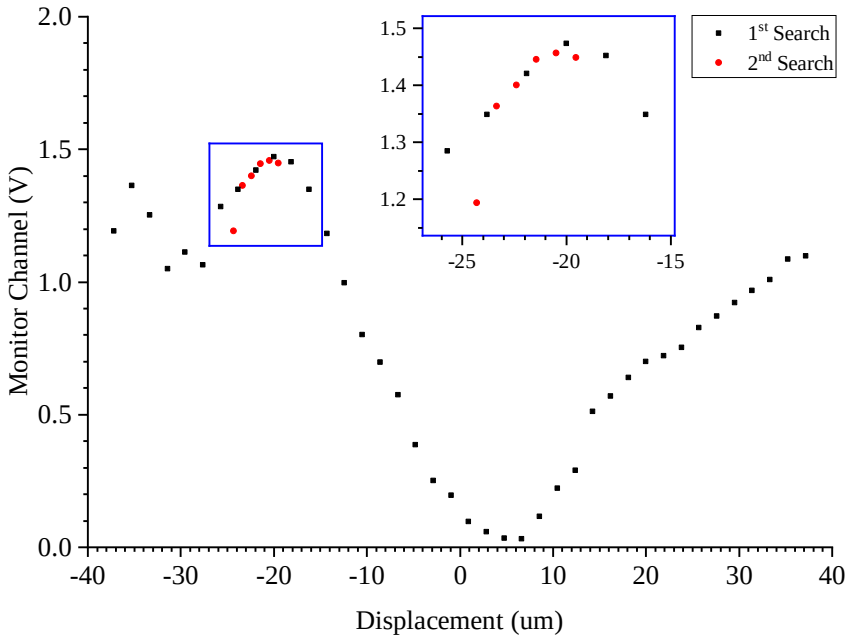

Figure 7.2: The variation of the monitor channel signal across the surface of the specimen around the location of array element 100. The voltage of the monitor signal is recorded at various locations as part of a search process to try and collect data at locations of high reflectivity.

then the data was collected at that location. If during the second search the response at a location was lower than the response at the previous location then the data was collected at that location. If, by the end of the second search, data had not been collected, then the interferometer would return to the location of the peak response from the first search and collect data at that location. The nominal element position was then updated with the location at which the data were collected. A graphical example of this process is shown in Figure 7.2. This process yielded an array with elements which were not uniformly spaced. This search process could be omitted to increase the data collection speed. For example, when not using the search process, the collection of the 128 element diffuse field array data took approximately $100\,\mathrm{s}$. This was increased by a factor of 9 when the search process was used. The backlash of the translation stage, which was of the order of $16\,\mu\mathrm{m}$ according to the data sheet, meant that this process was not perfect. It is noted that the search process outlined above is crude, and could be improved, but this was not the focus of the study.

Example amplitudes of the monitor channel voltage at each array element when the search was not used is shown in Figure 7.3a. The peak response from the first search is shown in Figure 7.3b and the voltage at the location the data were collected at after the search process was complete is shown in Figure 7.3c. The difference between the monitor channel voltage

for each element when the search process is, and is not, used is shown in Figure 7.3d. Elements from 121 onwards were ignored when calculating any improvement as the last few array elements were not on the surface of the sample during this example. The light search methodology, however basic, clearly shows an improvement in the amplitude of the monitor signal voltage in this example. The mean voltage was improved by a factor of approximately 2. More importantly, the minimum voltage in the range was improved by a factor of approximately 9. When the search was not used, some array elements could not be used because the received signals were not efficiently digitised by the range set on the ADC.

7.2.4 Imaging

The diffuse field data were reconstructed into a full array response matrix using Equation 6.3 and Equation 6.4. Before reconstruction, the influence of the amount of light returned to the interferometer from the sample surface on the amplitude of the A-Scan signals was removed. This was done by dividing each A-Scan by the monitor channel voltage for the location at which it was collected. No division was performed for monitor channel voltages of less than $0.1\,\mathrm{V}$ to prevent the large amplification of A-Scans which contained predominantly detector noise. For the data presented here this applied to 3 elements in total.

All A-Scans used for imaging were first filtered with a Gaussian filter. The centre frequency and standard deviation of this filter were $3.5\,\mathrm{MHz}$ and $5\,\mathrm{MHz}$ respectively.

The TFM algorithm was used to image all the data in this chapter. In keeping with the previous literature on laser ultrasonic arrays, weighting was applied to each transmit-receive combination in accordance with Equation 5.7. The weighting applied was proportional to the theoretical directivity of the array elements and the beam spread of a point reflector.

7.2.5 Performance Evaluation

The Signal-to-Noise Ratio (SNR) was evaluated in the same way as in Section 6.2.5.

7.3 Results

Samples of the pulse-echo A-Scan from the transducer at location A, at early and late times, are shown in Figure 7.4. An example longitudinal wave mode image, reconstructed from diffuse field data, is shown in Figure 7.5. The search algorithm was used when collecting the

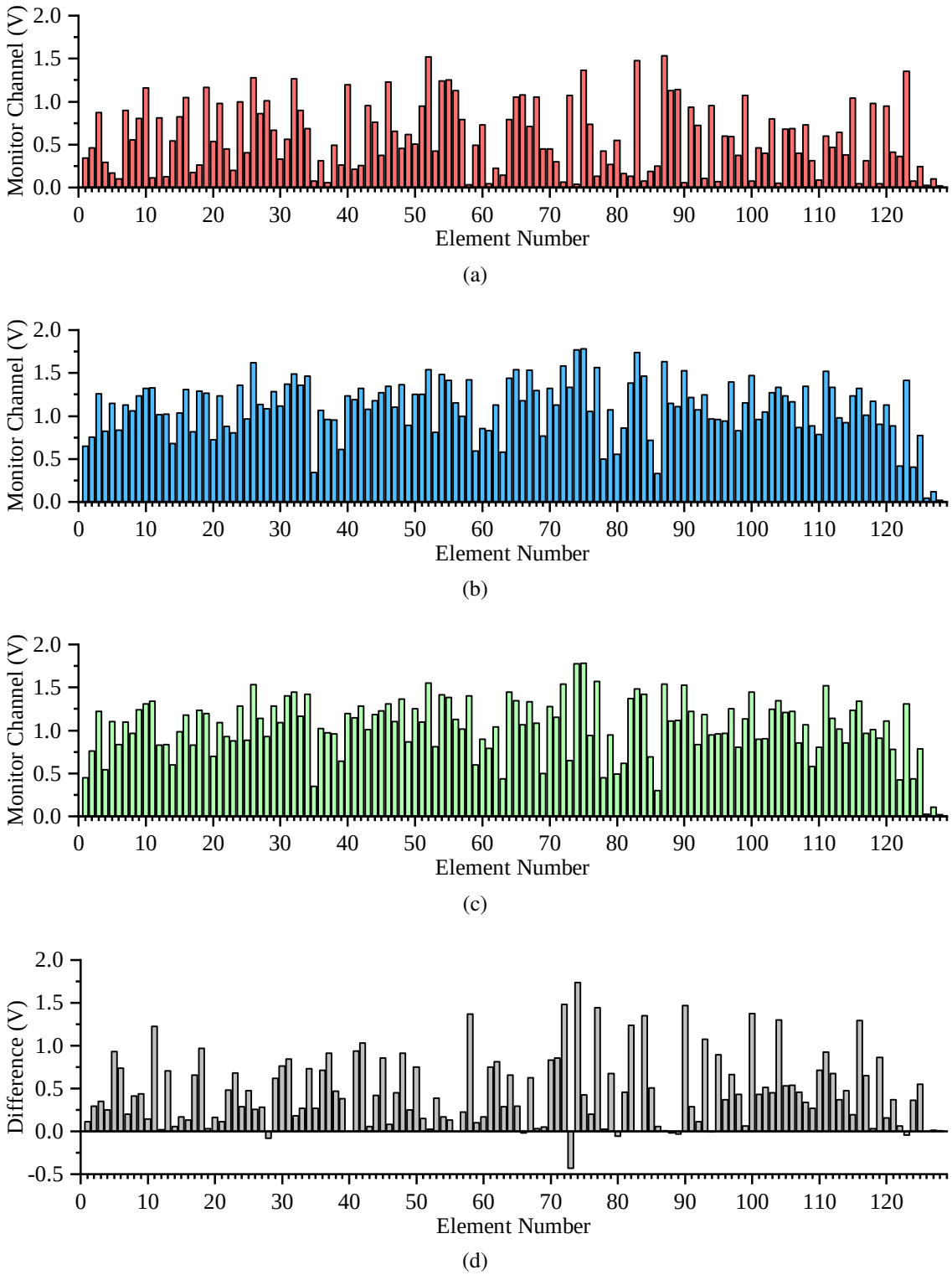

Figure 7.3: Monitor channel voltages for elements in a 128 element array when (a) no search system is used to try and find locations of high reflectance, (b) the initial search process is applied and (c) the second search process is applied and data are collected. (d) shows the difference in the monitor signal at data collection when a search process is and isn't applied. The last few elements of the array were not on the specimen surface and so produce no meaningful reflection.

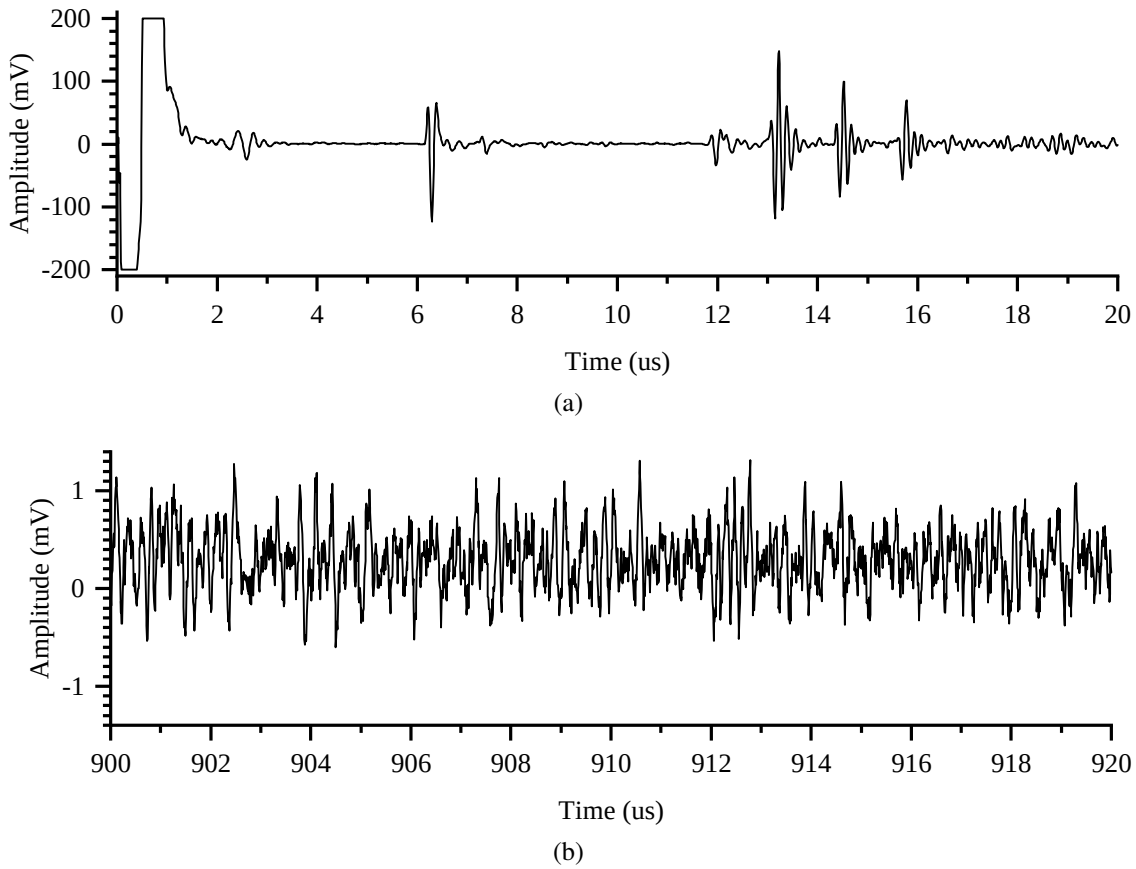

Figure 7.4: Samples of the pulse-echo response from the transducer at location A. The coherent and diffuse nature of the field at early and late times can be seen in (a) and (b) respectively.

data used for this image and data collection took 15 minutes. The first 128 transmit-receive combination A-Scans of the reconstructed full array response matrix are shown in Figure 7.6. Two A-Scans from the diffuse field data and the pitch-catch A-Scan reconstructed from these two A-Scans are shown in Figure 7.7. The effect on the SNR of the final image of the number of repetition averages taken when collecting the diffuse field data is shown in Figure 7.8. Similarly, the effect of changing the centre frequency and bandwidth of the Gaussian filter applied before imaging, is shown in Figure 7.9. Finally, the mean SNRs of the reconstructed image as a function of the reconstruction window length and window location are shown in Figure 7.10 and Figure 7.11 respectively. The window length is shown for both the full window being used for the reconstruction, and the window being broken up into sub-windows before the result is averaged.

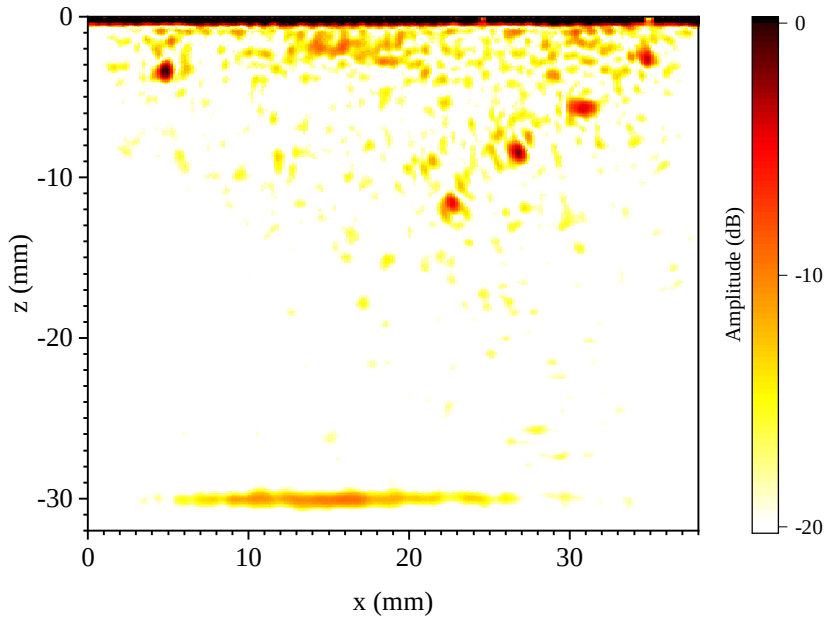

(a)

Figure 7.5: TFM images from reconstructed data for the 128 element array where the transmitting transducer located at position A. 16 repetition averages were used during data collection. The reconstruction window used was from 0 µs to 250 µs. No sub-windows were used for the reconstruction. The decibel scale has been normalised to the maximum value in the image. Weighting for both the element directivity and the beam spread of a point reflector was incorporated into the imaging algorithm.

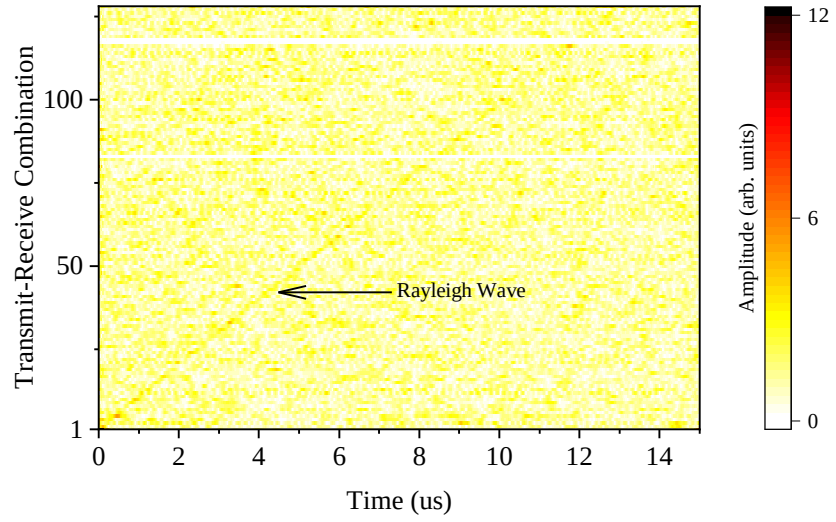

(a)

Figure 7.6: The first 128 A-Scans of the reconstructed full array response matrix. Element 1 is used in transmission and all 128 elements are used in reception. The linear instantaneous amplitude is shown. Only the first 15 µs of each A-Scan are shown.

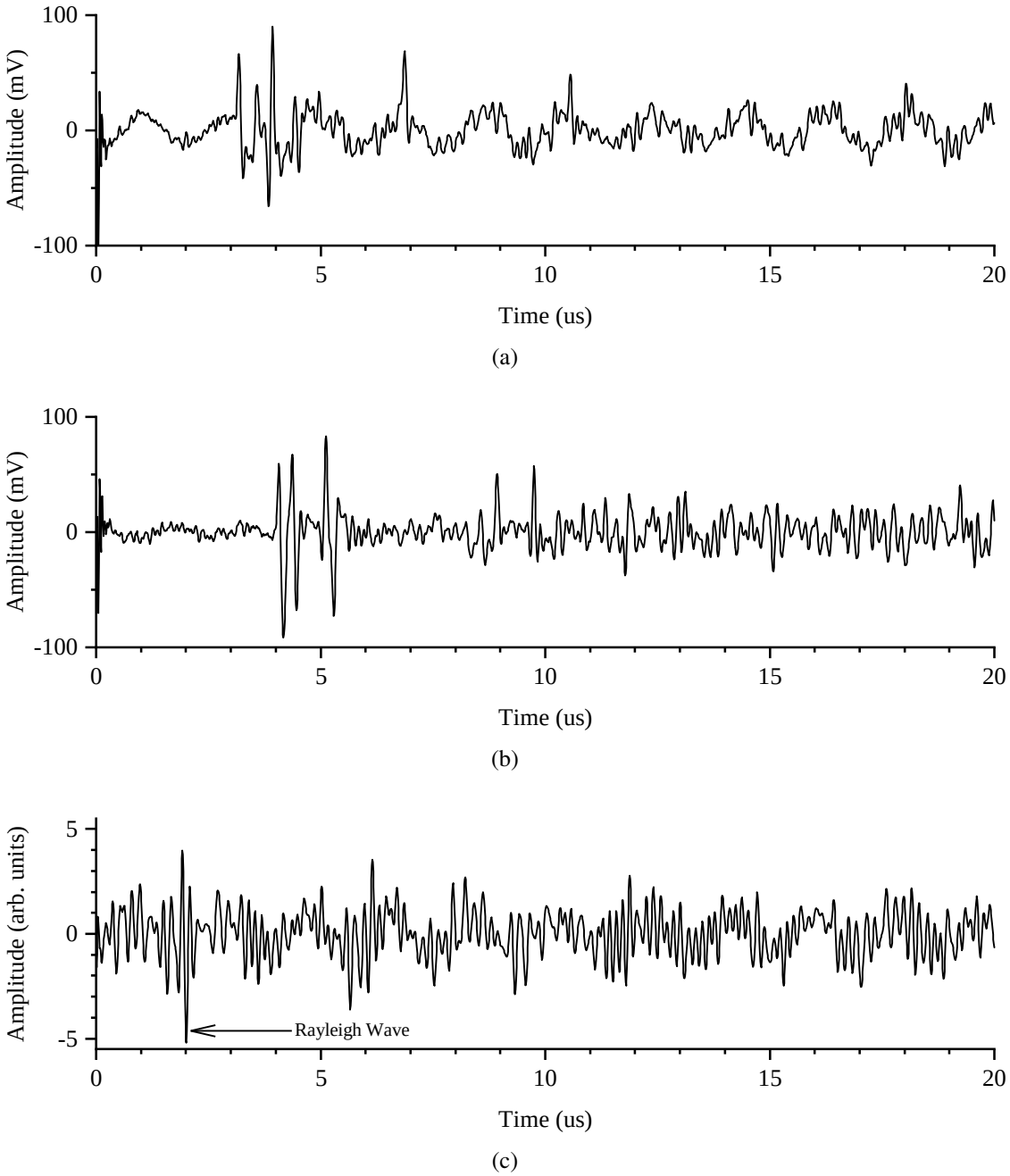

Figure 7.7: A-Scans from elements (a) 12 and (b) 31 of the diffuse field data. The reconstructed pitch-catch A-Scan between these two elements is shown in (c). Only the first 20 μs of each A-Scan are shown.

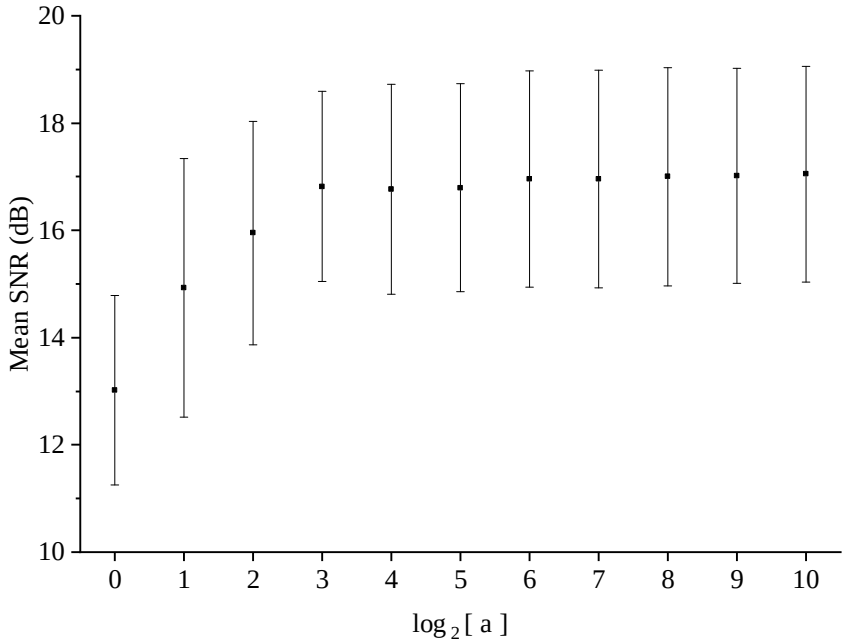

Figure 7.8: The mean SNR of the SDHs in the image for different numbers of repetition averages. A logarithm with base-2 was taken of the number of repetition averages, a, to increase the clarity of the plot. The error bar shows the standard deviation of the SNR of the SDHs in the image. The reconstruction window used was from $0\,\mu s$ to $100\,\mu s$. No sub-windows were used for the reconstruction.

7.4 Discussion

Figure 7.5 shows that diffuse field data can be used to reconstruct the full array response matrix of a laser ultrasonic array in reception. This is in agreement with the Finite Element (FE) modelling carried out in Chapter 6. The SDHs and back wall are clearly visible, although there is some noise. There are no Rayleigh wave artefacts in the image although the Rayleigh waves between elements are clearly shown reconstructed in Figure 7.6 and Figure 7.7c. This suggests that, in accordance with the theory, the transfer function of the receive elements becomes the transfer function in both transmit and receive on reconstruction.

The number of repetition averages was chosen to be 16 from the plot shown in Figure 7.8. It is clear that the affect of adding more averages after this point has little effect on the final result. This indicated that after this point the random noise in the diffuse field data is no longer the main contributing factor to the image SNR. This is the case when the reconstruction window is at early times when the SNR is highest. At later times the number of averages required may increase. Ultimately the number of repetition averages is a compromise between SNR and data collection speed.

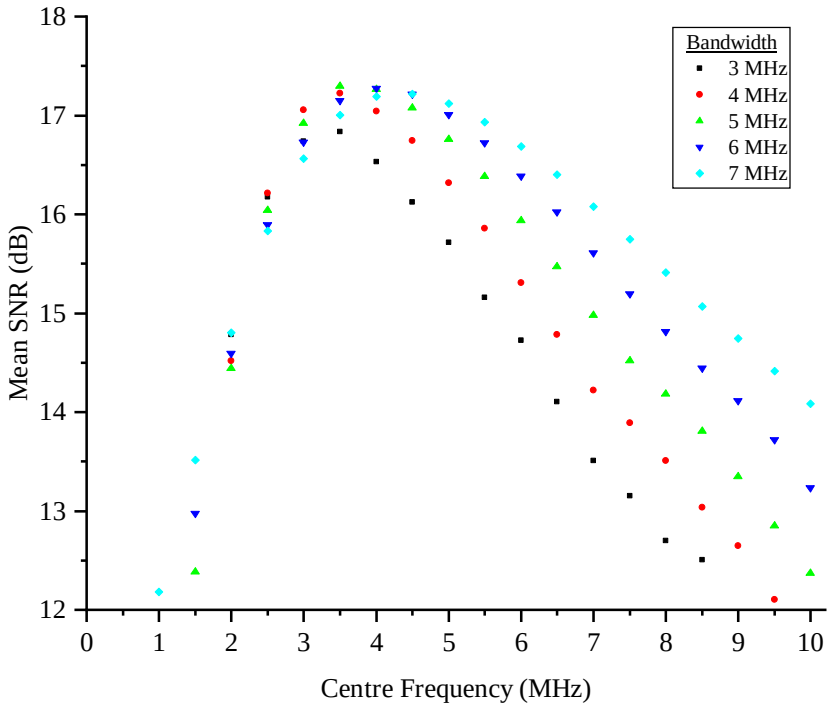

Figure 7.9: The mean SNR of the SDHs in the image for different centre frequencies and bandwidths of Gaussian frequency filter. Error bars have been removed to increase the clarity of the plot. The reconstruction window used was from 0 µs to 150 µs. No sub-windows were used for the reconstruction.

The shift in the best centre frequency to filter the reconstructed data with from the centre frequency of the generating transducer is shown in Figure 7.9. There are two possible causes for this. First that the peak frequency response of the interferometer is not at the centre frequency of the generating transducer. This is known to be the case, however the exact value has not been characterised. The second possibility is that, as attenuation affects higher frequencies to a greater degree than lower frequencies, the useful information in the reconstruction window changes from the centre frequency of the generating transducer towards lower frequencies at later and later times. The former possibility is more likely due to aluminium exhibiting very low attenuation and the transfer function of the receive elements in the array, which includes their frequency response, being demonstrated earlier to be the transfer function in both transmit and receive on reconstruction. The best centre frequency is shown to increase with bandwidth for the two highest bandwidths in Figure 7.9. The cause of this is expected to be that the peak SNR occurs when the Gaussian filter is best fitted to the non-Gaussian frequency response of the interferometer.

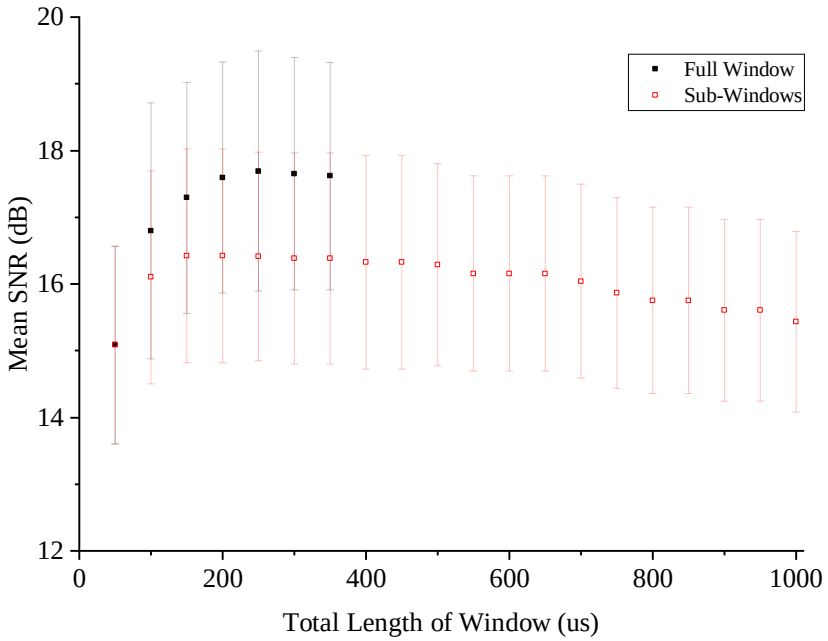

Figure 7.10: The mean SNR of the SDHs in the image for different reconstruction window lengths. The error bar shows the standard deviation of the SNR of the SDHs in the image. Two data sets are potted. The first uses the full window length for the reconstruction. The second splits the window up into sub-windows, calculates the reconstruction, and then averages the results from all of the sub-windows. All windows began at $0\,\mu s$. The full window reconstruction is highly computationally expensive and so is not performed beyond a window length of $350\,\mu s$.

It is clear from Figure 7.10 and Figure 7.11 that the addition of attenuation and noise has an affect on the best length and location of the reconstruction window in time. The SNR is shown to initially increase with an increasing window length as more and more useful information is added to the reconstruction process. However this benefit is soon lost as the signal from the A-Scan added to the reconstruction process contains proportionally more random noise as the contributions come from later and later times. The same trend is seen experimentally as in the FE modelling that using the full window, as opposed to sub-windows, produces images with a higher SNR. It is clear from Figure 7.11 that increasing the window length helps to increase the SNR even as the SNR generally decreases rapidly. Where the SNR appears to level off, at around $8\,dB$, it is likely that fluctuations in the noise are being measured rather than signals from the target SDHs. The lack of initial increase in SNR as the window shifts to cover a more diffuse field is probably due to the sample's ability to scatter the ultrasound quickly throughout the sample and the degrading effect of the noise as the window moves later in time.

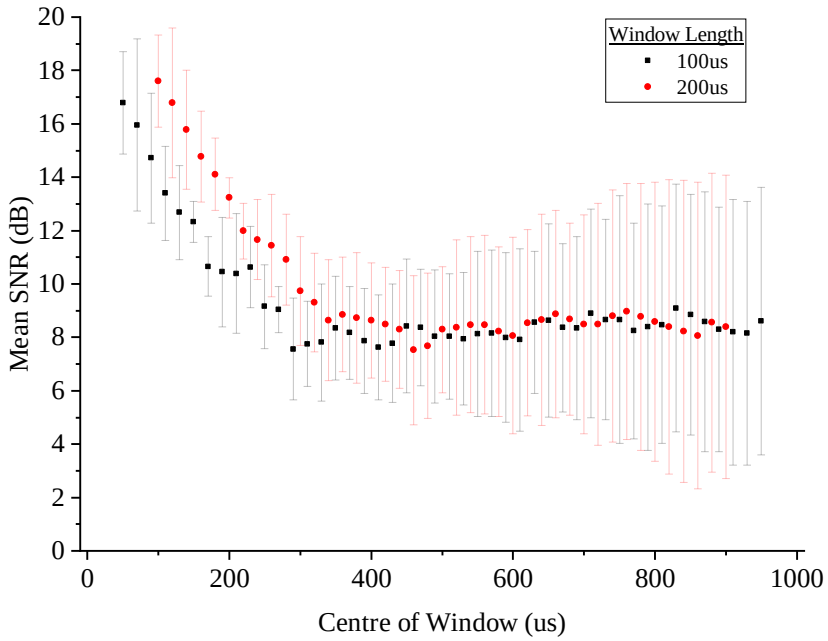

Figure 7.11: The mean SNR of the SDHs in the image for different reconstruction window centres. The error bar shows the standard deviation of the SNR of the SDHs in the image. Two different data sets are plotted corresponding to different window lengths.

7.5 Conclusion

The possibility of using diffuse fields to create a laser ultrasonic array of receive elements operating in both transmit and receive has been shown to work experimentally. The Rayleigh wave artefacts were shown to be absent from the images, despite Rayleigh waves clearly being reconstructed, the back wall was visible in the images and the data collection time was much less than for conventional laser ultrasonic arrays. These experimental results increase the probability that a fully non-contact version of this experiment, using high powered lasers in generation, could work experimentally.

Chapter 8

Conclusion

8.1 Summary

Two examples of improving the imaging performance of novel, that is non-standard, ultrasonic arrays have been presented.

The first example exploited the symmetry of the Row-Column Addressed (RCA) array, adapting the Total Focusing Method (TFM) imaging algorithm for use with RCA arrays. In Chapter 3, Fully Populated 2D (FP2) and RCA arrays with large numbers of elements were shown, through modelling, to be comparable when using the adapted TFM algorithm. The algorithm was tested experimentally in Chapter 4 using a commercial RCA array, the DolphiCam, with good results shown. The sizing of Flat Bottom Holes (FBHs) was shown to be improved in both accuracy and precision when using the adapted TFM algorithm. In addition, a less-than-half-wavelength Conical Bottom Hole (CBH) was successfully detected $17\,\mathrm{dB}$ above the Root Mean Square (RMS) noise level. Even with these improvements, the DolphiCam remains a fairly noisy array when compared to a standard FP2 array. Since the work on the DolphiCam was done, DolphiTech have released a new version of the DolphiCam. This has not yet been tested. In terms of the novelty of this example, the TFM had never before been applied to RCA arrays in the field of Non-Destructive Evaluation (NDE). In terms of the industrial relevance of this example, an improvement to the DolphiCam has been demonstrated and was incorporated by DolphiTech into their latest product.

The second example, covered in Chapter 6 and Chapter 7, used the properties of the diffuse field to reconstruct a laser ultrasonic array of interferometers. The method of data collection used increased the data collection speed, allowing a full array response matrix of data to be

collected in under 2 minutes. This is an improvement of two orders of magnitude over the latest published laser ultrasonic array. Through the reconstruction, the interferometer acted as if it could transmit and receive, improving the directivity of the array when compared to normal laser ultrasonic arrays. The technique used was proved successful in imaging a selection of Side Drilled Holes (SDHs) and the back wall of a sample. The Signal-to-Noise Ratio (SNR) of the technique was, however, still low. In addition, the technique used a contact transducer which removed the non-contact element of standard laser ultrasonic arrays. This is not mandatory for the technique however, and a laser ultrasonic source could be used. The samples inspected are also required to be small and their geometry such that the ultrasound is quickly scattered throughout the sample. In terms of the novelty of this example, laser ultrasonic arrays have never before been used with diffuse fields to reconstruct a laser ultrasonic array of interferometers. The industrial relevance of this example is less clear than the first example, however, the technique has been shown to be viable should a future requirement arise.

Both examples have shown an improvement to the imaging performance of a novel ultrasonic array. However, specific cases have been selected which are most favourable to the technique used. Further work is required to generalise the result.

8.2 Recommendations for Further Work

8.2.1 Row-Column Addressed Arrays and the Total Focusing Method

While the work carried out in this thesis shows compelling reasons to use RCA arrays in the place of FP2 arrays, further work is still required to explore this further. It would be advantageous to consider the Point Spread Function (PSF) for a range of off-centre locations under the array and compare the results to those presented here for directly under the centre of the array. Metrics, other than the volume of the PSF should also be considered, for example metrics which quantify resolution. Finally, validity of the assumption that the array-sample interface is parallel could be investigated. A method of calculating the imaging path for non-parallel interfaces has also not been conceived.

8.2.2 Laser Ultrasonic Arrays through Diffuse Field Reconstruction

The possibilities of further work on using diffuse field reconstruction to improve laser ultrasonic arrays are much larger than for the project involving RCA arrays and the TFM. The

most obvious next step is to test a fully non-contact version of the system demonstrated here, where the transducer used here is replaced with a generation laser. Equally obvious is the use of 2-Dimensional (2D) arrays with the same hybrid technique described here. Both of these were attempted at some point during this project. Although the initial results were positive, the results were in a less developed stage than those presented here and so were not included.

More abstract work would include reconstructing the pulse-echo signal from a single interferometer location using only the thermal noise in the sample. Equally abstract would be creating an array generation lasers with beam shapes engineered to improve directivity with a single interferometer recording the diffuse field signals.

Bibliography

[1] Fredrik Lingvall and Eskil Skoglund. 1.3 Technical Paper, 2015.

[2] S. Deutsch. A preliminary study of the fluid mechanics of liquid penetrant testing. *Journal of research of the National Bureau of Standards*, 84:287, 1979.

[3] J. R. Bowler and N. Bowler. Evaluation of the magnetic field near a crack with application to magnetic particle inspection. *Journal of Physics D: Applied Physics*, 35(18): 2237–2242, Sep 2002.

[4] R. Hughes, Y. Fan, and S. Dixon. Near electrical resonance signal enhancement (NERSE) in eddy-current crack detection. *NDT & E International*, 66:82–89, 2014.

[5] E. Deprins. Computed radiography in NDT applications. *Insight - Non-Destructive Testing and Condition Monitoring*, 46(10):590–593, Oct 2004.

[6] D. P. Almond and S. G. Pickering. Analysis of the defect detection capabilities of pulse stimulated thermographic NDE techniques. *AIP Conference Proceedings*, 1581 (1):1617–1623, 2014.

[7] Y. C. Lee J. D. Achenbach, I. N. Komsky and Y. C. Angel. Self-calibrating ultrasonic technique for crack depth measurement. *Journal of Nondestructive Evaluation*, 11:103–108, 1992.

[8] J. P. Kirkpatrick, P. D. Wilcox, and R. A. Smith. Row-column addressed arrays for non-destructive evaluation applications. *IEEE Transactions on Ultrasonics, Ferroelectrics, and Frequency Control*, 66(6):1119–1128, 2019.

[9] Shi-Chang Wooh and Yijun Shi. Three-dimensional beam directivity of phase-steered ultrasound. *The Journal of the Acoustical Society of America*, 105(6):3275–3282, 1999.

[10] G. F. Miller and H. Pursey. The field and radiation impedance of mechanical radiators on the free surface of a semi-infinite isotropic solid. *Proceedings of the Royal Society*

of London A: Mathematical, Physical and Engineering Sciences, 223(1155):521–541, 1953.

[11] J. D. Achenbach. *Reciprocity in Elastodynamics*. Cambridge Monographs on Mechanics. Cambridge University Press, 2004.

[12] R. B. Thompson and T. A. Gray. A model relating ultrasonic scattering measurements through liquidsolid interfaces to unbounded medium scattering amplitudes. *The Journal of the Acoustical Society of America*, 74(4):1279–1290, 1983.

[13] L. W. Schmerr Jr. *Fundamentals of Ultrasonic Nondestructive Evaluation*. Springer, Switzerland, 2 edition, 2016.

[14] Jie Zhang, Bruce W. Drinkwater, and Paul D. Wilcox. Effects of array transducer inconsistencies on total focusing method imaging performance. *NDT & E International*, 44 (4):361–368, 2011.

[15] N. Budyn, R. L. T. Bevan, J. Zhang, A. J. Croxford, and P. D. Wilcox. A model for multiview ultrasonic array inspection of small two-dimensional defects. *IEEE Transactions on Ultrasonics, Ferroelectrics, and Frequency Control*, 66(6):1129–1139, 2019.

[16] H. A. Bloxham, A. Velichko, and P. D. Wilcox. Combining simulated and experimental data to simulate ultrasonic array data from defects in materials with high structural noise. *IEEE Transactions on Ultrasonics, Ferroelectrics, and Frequency Control*, 63(12):2198–2206, 2016.

[17] P. D. Wilcox and J. Zhang. Quantification of the effect of array element pitch on imaging performance. *IEEE Transactions on Ultrasonics, Ferroelectrics, and Frequency Control*, 65(4):600–616, 2018.

[18] Theodosia Stratoudaki, Matt Clark, and Paul D. Wilcox. Laser induced ultrasonic phased array using full matrix capture data acquisition and total focusing method. *Opt. Express*, 24(19):21921–21938, Sep 2016.

[19] Maria V. Felice, Alexander Velichko, and Paul D. Wilcox. Accurate depth measurement of small surface-breaking cracks using an ultrasonic array post-processing technique. *NDT & E International*, 68:105–112, 2014.

[20] Caroline. Holmes, Bruce W. Drinkwater, and Paul D. Wilcox. Post-processing of the full matrix of ultrasonic transmit-receive array data for guided wave pipe inspection. *NDT & E International*, 38:701–711, 2005.

[21] Shyamal C. Mondal, Paul D. Wilcox, and Bruce W. Drinkwater. Design of Two-Dimensional Ultrasonic Phased Array Transducers. *Journal of Pressure Vessel Technology*, 127(3):336–344, 03 2005.

[22] A. Velichko and P. D. Wilcox. Defect characterization using two-dimensional arrays. *AIP Conference Proceedings*, 1335(1):835–842, 2011.

[23] Lawrence L P Wong, Albert I H Chen, Zhenhao Li, Andrew S. Logan, and John T W Yeow. A row-column addressed micromachined ultrasonic transducer array for surface scanning applications. *Ultrasonics*, 54(8):2072–2080, 2014.

[24] G. Curtis and A. B. Joinson. Polyscan - A rapid, ultrasonic, through-transmission C-scanning system. In *8th World Conference on Non-Destructive Testing*, 1976.

[25] M. Bernard. Crossed-Transducers Array for Transmission Ultrasonic Imaging. In *1983 Ultrasonics Symposium*, pages 732–735, 1983.

[26] Andreas Koch, Stefan Gruber, Thomas Scharrer, Karl Thomas Fendt, Reinhard Lerch, and Helmut Ermert. 2D transmission imaging with a crossed-array configuration for defect detection. In *IEEE International Ultrasonics Symposium*, pages 36–39, 2012.

[27] Han Wang, Yongqiang Qiu, Christine E M Démoré, Sylvia Gebhardt, and Sandy Cochran. 2-D Crossed-electrode Transducer Arrays for Ultrasonic Particle Manipulation. In *IEEE International Ultrasonics Symposium*, 2016.

[28] Roger J. Zemp, Ryan Chee, Alexander Sampaleanu, Deepak Rishi, and Alexander Forbrich. S-sequence bias-encoded photoacoustic imaging with top Orthogonal to Bottom Electrode (TOBE) CMUT arrays. In *IEEE International Ultrasonics Symposium*, pages 1197–1200, 2013.

[29] C.E. Morton and Geoffrey R. Lockwood. Theoretical assessment of a crossed electrode 2-D array for 3-D imaging. In *IEEE Symposium on Ultrasonics*, pages 968–971, 2003.

[30] Morten Fischer Rasmussen, Thomas Lehrmann Christiansen, Erik Vilain Thomsen, and Jorgen Arendt Jensen. 3-D imaging using row-column-addressed arrays with integrated apodization -Part i: Apodization design and line element beamforming. *IEEE Transactions on Ultrasonics, Ferroelectrics, and Frequency Control*, 62(5):947–958, 2015.

[31] Thomas Lehrmann Christiansen, Morten Fischer Rasmussen, Jan Peter Bagge, Lars Nordahl Moesner, Jorgen Arendt Jensen, and Erik Vilain Thomsen. 3-D imaging using row-column-addressed arrays with integrated apodization-part ii: Transducer fabrication and

experimental results. *IEEE Transactions on Ultrasonics, Ferroelectrics, and Frequency Control*, 62(5):959–971, 2015.

[32] Christine E M Démoré, Andrew Joyce, Kieran Wall, and Geoffrey R. Lockwood. Real-time volume imaging using a crossed electrode array. *IEEE Transactions on Ultrasonics, Ferroelectrics, and Frequency Control*, 56(6):1252–1261, 2009.

[33] Bruce W. Drinkwater and Paul D. Wilcox. Ultrasonic arrays for non-destructive evaluation: A review. *NDT & E International*, 39(7):525–541, 2006.

[34] Jie Zhang, Bruce W. Drinkwater, Paul D. Wilcox, and Alan J. Hunter. Defect detection using ultrasonic arrays: The multi-mode total focusing method. *NDT & E International*, 43(2):123–133, 2010.

[35] Terje Melandso, Frank Melandso, and Tore Baarstad. Ultrasonic Transducer Module Comprising a Transmitter Layer and a Receiver Layer, 2008.

[36] P. D. Wilcox. Array imaging of noisy materials. In *AIP Conference Proceedings*, volume 1335, pages 890–897, 2011.

[37] Jessica G. McKee, Rhodri L.T. Bevan, Paul D. Wilcox, and Robert E. Malkin. Volumetric imaging through a doubly-curved surface using a 2D phased array. *NDT & E International*, 113:102260, 2020.

[38] Robert A. Smith. Ultrasonic defect sizing in carbon-fibre composites - an initial study. *Insight*, 36(8):595–605, 1994.

[39] J. N. Potter, A. J. Croxford, and P. D. Wilcox. Nonlinear ultrasonic phased array imaging. *Phys. Rev. Lett.*, 113:144301, Oct 2014.

[40] J. Potter and A. J. Croxford. Characterization of nonlinear ultrasonic diffuse energy imaging. *IEEE Transactions on Ultrasonics, Ferroelectrics, and Frequency Control*, 65 (5):870–880, 2018.

[41] Davis M. Egle. Diffuse wave fields in solid media. *The Journal of the Acoustical Society of America*, 70(2):476–480, 1981.

[42] Richard L. Weaver. On diffuse waves in solid media. *The Journal of the Acoustical Society of America*, 71(6):1608–1609, 1982.

[43] R.L. Weaver. Diffuse waves in finite plates. *Journal of Sound and Vibration*, 94(3):319 – 335, 1984.

[44] Richard L. Weaver. Diffuse elastic waves at a free surface. *The Journal of the Acoustical Society of America*, 78(1):131–136, 1985.

[45] Richard L. Weaver. Diffuse field decay rates for material characterization. In J. D. Achenbach and Y. Rajapakse, editors, *Solid mechanics research for quantitative non-destructive evaluation*, pages 425–434, Dordrecht, 1987. Springer Netherlands.

[46] John Burkhardt. Spectral statistics in damped systems: Diffuse field decay curvature for materials characterization. *The Journal of the Acoustical Society of America*, 102(4): 2113–2116, 1997.

[47] Oleg I. Lobkis and Richard L. Weaver. On the emergence of the greens function in the correlations of a diffuse field. *The Journal of the Acoustical Society of America*, 110(6): 3011–3017, 2001.

[48] Richard L. Weaver and Oleg I. Lobkis. Ultrasonics without a source: Thermal fluctuation correlations at mhz frequencies. *Phys. Rev. Lett.*, 87:134301, Sep 2001.

[49] Richard Weaver and Oleg Lobkis. On the emergence of the green's function in the correlations of a diffuse field: pulse-echo using thermal phonons. *Ultrasonics*, 40(1): 435 – 439, 2002.

[50] Richard L. Weaver and Oleg I. Lobkis. Elastic wave thermal fluctuations, ultrasonic waveforms by correlation of thermal phonons. *The Journal of the Acoustical Society of America*, 113(5):2611–2621, 2003.

[51] Richard L. Weaver and Oleg I. Lobkis. Fluctuations in diffuse fieldfield correlations and the emergence of the greens function in open systems. *The Journal of the Acoustical Society of America*, 117(6):3432–3439, 2005.

[52] Richard L. Weaver and Oleg I. Lobkis. The mean and variance of diffuse field correlations in finite bodies. *The Journal of the Acoustical Society of America*, 118(6): 3447–3456, 2005.

[53] Roel Snieder. Extracting the green's function from the correlation of coda waves: A derivation based on stationary phase. *Phys. Rev. E*, 69:046610, Apr 2004.

[54] P. Goudard, L. Stehly, F. Brenguier, M. Campillo, Y. Colin de Verdire, E. Larose, L. Margerin, P. Roux, F. J. Snchez-Sesma, N. M. Shapiro, and R. L. Weaver. Cross-correlation of random fields: mathematical approach and applications. *Geophysical Prospecting*, 56(3):375–393, 2008.

[55] Adelaide Duroux, Karim G. Sabra, James Ayers, and Massimo Ruzzene. Using cross-correlations of elastic diffuse fields for attenuation tomography of structural damage. *The Journal of the Acoustical Society of America*, 127(6):3311–3314, 2010.

[56] Tom Druet, Bastien Chapuis, and Emmanuel Moulin. Feasibility of passive tomography of extended defects using ambient elastic noise correlation. *Physics Procedia*, 70:640 – 643, 2015. Proceedings of the 2015 ICU International Congress on Ultrasonics, Metz, France.

[57] J.N. Potter, P.D. Wilcox, and A.J. Croxford. Diffuse field full matrix capture for near surface ultrasonic imaging. *Ultrasonics*, 82:44 – 48, 2018.

[58] D. A. Hutchins. 2 - ultrasonic generation by pulsed lasers. volume 18 of *Physical Acoustics*, pages 21 – 123. Academic Press, 1988.

[59] Victor V. Krylov. Directivity patterns of laser-generated sound in solids: Effects of optical and thermal parameters. *Ultrasonics*, 69:279 – 284, 2016.

[60] C. B. Scruby and L. E. Drain. *Laser Ultrasonics, Techniques and Applications*. Adam Hilger, Bristol, UK, 1990.

[61] Marie-Helene Noroy, Daniel Royer, and Mathias Fink. The laser-generated ultrasonic phased array: Analysis and experiments. *The Journal of the Acoustical Society of America*, 94(4):1934–1943, 1993.

[62] J. Scott Steckenrider, Todd W. Murray, James W. Wagner, and John B. Deaton. Sensitivity enhancement in laser ultrasonics using a versatile laser array system. *The Journal of the Acoustical Society of America*, 97(1):273–279, 1995.

[63] Sandra N. Hopko, I. Charles Ume, and Dathan S. Erdahl. Development of a Flexible Laser Ultrasonic Probe . *Journal of Manufacturing Science and Engineering*, 124(2): 351–357, 04 2002.

[64] A. J. A. Bruinsma and J. A. Vogel. Ultrasonic noncontact inspection system with optical fiber methods. *Appl. Opt.*, 27(22):4690–4695, Nov 1988.

[65] Jacek Jarzynski and Yves H. Berthelot. The use of optical fibers to enhance the laser generation of ultrasonic waves. *The Journal of the Acoustical Society of America*, 85(1): 158–162, 1989.

[66] Cuixiang Pei, Kazuyuki Demachi, Tetsuo Fukuchi, Kazuyoshi Koyama, and Mitsuru Uesaka. Cracks measurement using fiber-phased array laser ultrasound generation. *Journal of Applied Physics*, 113(16):163101, 2013.

[67] Xiao Wang, Michael G. Littman, John B. McManus, Mohsen Tadi, Young Sik Kim, Attila Askar, and Herschel Rabitz. Focused bulk ultrasonic waves generated by ringshaped laser illumination and application to flaw detection. *Journal of Applied Physics*, 80(8): 4274–4281, 1996.

[68] Theodosia Stratoudaki, Matt Clark, and Paul D. Wilcox. Full matrix capture and the total focusing imaging algorithm using laser induced ultrasonic phased arrays. *AIP Conference Proceedings*, 1806(1):020022, 2017.

[69] T. Stratoudaki, M. Clark, and P. D. Wilcox. Adapting the full matrix capture and the total focusing method to laser ultrasonics for remote non destructive testing. In *2017 IEEE International Ultrasonics Symposium (IUS)*, pages 1–4, 2017.

[70] Don Pieris, Theodosia Stratoudaki, Yashar Javadi, Peter Lukacs, Sam Catchpole-Smith, Paul D. Wilcox, Adam Clare, and Matt Clark. Laser induced phased arrays (lipa) to detect nested features in additively manufactured components. *Materials & Design*, 187:108412, 2020.

[71] Peter Huthwaite. Accelerated finite element elastodynamic simulations using the GPU. *Journal of Computational Physics*, 257, Part A(0):687 – 707, 2014.

[72] Jonathan Richard Shewchuk. Triangle: Engineering a 2D Quality Mesh Generator and Delaunay Triangulator. In Ming C. Lin and Dinesh Manocha, editors, *Applied Computational Geometry: Towards Geometric Engineering*, volume 1148 of *Lecture Notes in Computer Science*, pages 203–222. Springer-Verlag, May 1996. From the First ACM Workshop on Applied Computational Geometry.

[73] J. D. Achenbach. *Wave Propagation in Elastic Solids*. North-Holland Series in Applied Mathematics and Mechanics. Elsevier, Amsterdam, 1975.

[74] Olympus. 920-108B-EN - Manually Controlled Pulser-Receivers 5072PR, 5073PR, 5077PR.

[75] Ivan Pelivanov, Takashi Buma, Jinjun Xia, Chen-Wei Wei, and Matthew ODonnell. Ndt of fiber-reinforced composites with a new fiber-optic pumpprobe laser-ultrasound system. *Photoacoustics*, 2(2):63 – 74, 2014.

[76] Ivan Pelivanov, Takashi Buma, Jinjun Xia, Chen-Wei Wei, and Matthew O'Donnell. A new fiber-optic non-contact compact laser-ultrasound scanner for fast non-destructive testing and evaluation of aircraft composites. *Journal of Applied Physics*, 115(11): 113105, 2014.